Site Specific X-ray Induced Changes In Organic And Metal Organic Compounds And Their Influence On Global Radiation Damage

Dissertation

zur Erlangung des Doktorgrades des Fachbereichs Physik

der Universität Hamburg

vorgelegt von

Désirée Ellen Heintz

aus Münster

Hamburg, 2012

Gutachter der Dissertation:

1. Prof. Dr. Edgar Weckert
2. Prof. Dr. Dr. Christian Betzel

Gutachter der Disputation:

1. Prof. Dr. Edgar Weckert
2. Dr. Alke Meents

Vorsitzender des Prüfungsausschusses: Prof. Dr. Peter Hauschildt

Vorsitzender des Promotionsausschusses: Dr. Michael Martins

Datum der Disputation: 21.06.2012

Contents

Abstract

State-of-the art 3rd generation synchrotron sources provide high photon flux densities. With advanced X-ray optics it has become possible to focus a large amount of photons into spots of less than a micron in size. This offers the possibility to obtain large amounts of high resolution data in a short amount of time. On the other hand, such high doses cause severe radiation damage, especially in case of biological materials, such as proteins. Radiation damage is known to alter the structure of the sample and can therefore lead to misinterpretations of the underlying biological principles.

X-ray radiation damage is generally categorised into global and specific damage. Global damage leads to an overall degradation of the sample. Specific damage occurs at specific sites of the sample. X-ray induced photoreduction, cleavage of disulfide bridges and decarboxylation are examples for specific radiation damage.

Radiation damage has been investigated extensively. However, no conclusive model covering all different aspects could be found so far. Cryocooling to liquid nitrogen temperatures is routinely applied in order to reduce the effects of radiation damage. Understanding of the underlying mechanisms is essential to develop methods to further reduce X-ray radiation damage.

The aim of this work was to systematically investigate the effects of specific and global X-ray radiation damage to biological samples and obtain a conclusive model to describe the underlying principles.

Based on the systematic studies performed in this work, it was possible to propose two conclusive mechanisms to describe X-ray induced photoreduction and global radiation damage. The findings of this work can therefore be seen as an important step in improving X-ray data collection.

The influence of chemical composition, temperature and solvent on X-ray induced photoreduction was investigated by X-ray Absorption Near Edge Spectroscopy and single crystal X-ray diffraction of two B12 cofactors - cyano- and methylcobalamin - as well as iron(II) and iron(III) complexes. The obtained results revealed that X-ray induced

photoreduction is a ligand dependent process, with a redox reaction taking place within the complex. It could further be shown that selective hydrogen abstraction plays an important role in the process of X-ray induced photoreduction.

Based on the experimental results of this work, a model to describe X-ray induced photoreduction of metal organic complexes could be proposed: As initial step, a low energy electron generated upon X-ray irradiation of the sample, interacts with the metal centre. This leads to a short-lived excited state with a temporary reduced metal centre. In the second step, two possible reactions can take place. If the ligand cannot be oxidised, the metal centre reacts back into its initial, oxidised state and the low energy electron is released. If an oxidation reaction takes place within the ligand, the metal centre is permanently reduced. Hydrogen abstraction from or decarboxylation of the ligand are two possible oxidation reactions. In case of a hydrogen abstraction as oxidation reaction, the photoreduction process is temperature dependent.

The process of X-ray induced hydrogen abstraction was further investigated in a combined X-ray and neutron diffraction study on the amino acids L-serine and L-alanine, which were used as model compounds for proteins, and the nucleoside deoxythymidine (thymidine) as a model for DNA. Hydrogen abstraction preferentially takes place at primary hydroxyl groups, leading to the formation of hydrogen gas. This process is also a main contributor to global radiation damage. A damage mechanism for L-serine could be found. It involves the abstraction of two hydrogen atoms, one from the hydroxyl group and one from the adjacent methylene group. Such a hydrogen abstraction results in the formation of a carbonyl group.

X-ray diffraction measurements on cyano- and methylcobalamin as well as on three metal amino acid complexes, containing nickel(II) and copper(II), respectively, were conducted to investigate the contribution of X-ray induced photoreduction to global radiation damage. Results from these measurements combined with the results from L-serine, L-alanine and thymidine allowed to propose a model to describe global radiation damage.

It is proposed that global radiation damage is mainly caused by hydrogen abstraction. The hydrogen gas formed in the sample exerts stress on the crystal lattice. Since crystals are anisotropic, their response to stress is also anisotropic. This results in a different expansion or contraction behaviour of the cell axes with dose, which also depends on the crystal symmetry. The changes in the unit cell axes generally cause an expansion of the unit cell. With increasing dose the amount of gas formed in the sample and, thus, the stress within the crystal increases. At a certain dose, the stress exceeds the tensile strength of the crystal. This disrupts the crystal lattice, which is reflected in an increase in mosaicity.

Kurzfassung

Synchrotronquellen der dritten Generation zeichnen sich durch ihre hohen Photonenflüsse aus. Mithilfe hochentwickelter Röntgenoptiken können diese hohen Flüsse auf sehr kleine Foki ($<\mu$m) konzentriert werden. Dadurch können in kürzester Zeit große Datenmengen gesammelt werden. Unglücklicherweise werden durch diese hohen Photonendichten die untersuchten Proben stark geschädigt. Diese röntgeninduzierten Schäden machen sich besonders im Falle biologischer Materialien bemerkbar. Ofmals führen sie zu grundlegenden Änderungen innerhalb der Molekülstruktur, was zu Fehlinterpretationen von biologischen Vorgängen führen kann.

Generell wird zwischen zwei Sorten von Strahlenschäden unterschieden: Zum einen globale Schäden, die nicht-lokalisierte Veränderungen der Probeneingeschaften zur Folge haben und bis hin zum vollständigen Zerfall der Probe führen können. Zum anderen werden auch spezifische Strahlenschäden beobachtet. Diese führen zu lokalisierten Veränderungen innerhalb der Probe. Beispiele sind hier röntgeninduzierte Photoreduktion von metallorganischen Komplexen, Spaltung von Disulfidbrücken sowie Decarboxylierung.

Die zugrundeliegenden Mechanismen röntgeninduzierter Strahlenschäden sind bis heute ein wichtiger Bestandteil der Forschung mit Photonen. Trotzdem konnte bis dato kein schlüssiges Modell zur Beschreibung aller auftretenden Effekte aufgestellt werden. Zur Verringerung von rönteninduzierten Schäden werden die meisten Proben heutzutage standardmässig bei einer Temperatur von 100 K gemessen. Um röntgeninduzierte Effekte noch weiter zu verringern, ist allerdings ein tieferes Verständnis aller involvierten Prozesse dringend erforderlich.

Es war das Ziel dieser Doktorarbeit, die Effekte spezifischer und globaler röntgeninduzierter Strahlenschäden an biologischen Materialien systematisch zu untersuchen und auf Basis dieser Untersuchungen ein schlüssiges Modell zur Beschreibung der zugrundeliegenden Mechanismen vorzustellen.

Im Laufe dieser Arbeit konnten zwei Modelle vorgeschlagen werden, mit denen zum ainen die Mechanismen der röntgeninduzierten Photoreduktion und zum anderen die globaler

Strahlenschäden beschrieben werden können. Die Ergebnisse dieser Arbeit können somit als wichtiger Schritt in diesem Bereich angesehen werden.

Mithilfe von Röntgenabsorptionsspektroskopie und Einkristall-Röntgendiffraktion konnte der Einfluss der Faktoren chemische Zusammensetzung, Temperatur und Lösungsmittel auf röntgeninduzierte Photoreduktion bestimmt werden. Hierfür wurden sechs Modellsysteme untersucht: zwei B12 Cofaktoren, Cyano- und Methylcobalamin, sowie zwei Eisen(III)- und zwei Eisen(II)-Komplexe.

Die Messungen zeigten, dass röntgeninduzierte Photoreduktion ein ligandenabhängiger Prozess ist und über eine Redoxreaktion innerhalb des Moleküls abläuft. Selektive Wasserstoffabstraktion scheint hierbei eine wichtige Rolle zu spielen.

Auf Basis dieser Ergebnisse wurde ein Modell zur Beschreibung der Reaktionsmechanismen aufgestellt. In diesem Modell wird ein niedrigenergetisches Elektron vom Metallzentrum eingefangen, was zu einem kurzlebigen, angeregten Zustand und einem reduzierten Metallzentrum führt. Im Anschluss an den Einfangprozess kann ein zweiter Reaktionsprozess stattfinden. In diesem verlässt das Elektron entweder das Metallzentrum und hinterlässt die Probe im Grundzustand, wenn keine Oxidation im Liganden stattfindet, oder aber es verbleibt im Metallzentrum, falls eine Oxidation im Liganden abläuft. Nur im zweiten Fall kann eine permanente Photoreduktion beobachtet werden. Abstraktion von Wasserstoff vom Liganden oder Decarboxylierung eines Liganden sind hierbei mögliche Oxidationen. Unsere Messungen zeigten, dass im Falle einer Wasserstoffabstraktion als Oxidationsprozess die Photoreduktion temperaturabhängig ist.

Wie bereits erwähnt, scheint selektive Wasserstoffabstraktion eine wichtige Rolle im Prozess röntgeninduzierter Strahlenschäden zu spielen. Mithilfe eines kombinierten Röntgen- und Neutronendiffraktionsexperiment an Einkristallen sollte diese These genauer untersucht werden. Hierbei wurden die Aminosäuren L-Serin und L-Alanin, als Bausteine von Proteinen, sowie das Nukleosid Deoxythymidin, als Baustein der DNA, ausgewählt. Unsere Experimente konnten zeigen, dass selektive Wasserstoffabstraktion bevorzugt an primären Hydroxylgruppen stattfindet und zur Bildung von Wasserstoffgas führt. Dieses Gas spielt im globalen Schadensprozess eine wichtige Rolle.

Im Rahmen dieser Untersuchungen konnte zudem der Schadensmechanismus von L-Serin aufgedeckt werden: Hier werden ein Wasserstoffatom der primären Hydroxylgruppe und ein Wasserstoffatom der benachbarten Methylengruppe durch die Röntgenstrahlung selektiv abgespalten, was zur Bildung einer Carbonylgruppe führt.

Röntgendiffraktionsmessungen von Cyano- und Methylcobalamin, sowie drei Metallaminosäurekomplexen mit Ni(II) bzw. Cu(II) als Metallzentren konnten den Beitrag röntgeninduzierter Photoreduktion zum globalen Schadensprozess aufzeigen. Auf Basis sämtlicher Diffraktionsmessungen wurde ein Modell zur Beschreibung globaler Strahlenschäden in Kristallen vorgestellt.

In diesem Modell werden globale Schäden hauptsächlich durch selektive und nicht-selektive Wasserstoffabstraktion verursacht. Im Zuge dieser Abstraktion entsteht Wasserstoffgas innerhalb der Probe, welches zu einer Spannung des Kristallgitters führt. Kristalle sind anisotrope Gebilde und besitzen entsprechend einen Elastiztätstensor. Abhängig von der Kristallsymmetrie führt dieser zu unterschiedlichem Ausdehnungs- und Kontraktionsverhalten der Zellachsen als Funktion der Dosis. Diese Veränderung der Zellachsen führt im Allgemeinen zu einer Vergrößerung des Zellvolumens. Mit steigender Dosis wird immer mehr Wasserstoffgas innerhalb der Probe generiert und entsprechend mehr Spannung wird auf das Kristallgitters ausgeübt. Ab einem bestimmten Punkt übersteigt diese Spannung die Zugfestigkeit des Kristalls. Dies führt zu Störungen im Kristallgitter, die sich durch ein Anwachsen der Kristallmosaizität bemerkbar machen.

I Introduction

Introduction

In this work different aspects of X-ray radiation damage were systematically investigated. X-ray induced photoreduction, selective hydrogen abstraction and global radiation damage, as well as their possible relation to each other, were explored by the application of different methods. It was the main goal of this work to obtain a conclusive model for X-ray induced photoreduction of metal organic compounds and for global radiation damage to organic samples in general.

X-ray radiation damage to biological samples is a major limitation in X-ray data collection. With the development of highly brilliant synchrotron sources and the possibility to focus a high amount of monochromatic photons into spots of less than a micrometre in size it has become possible to obtain high resolution structural information from large complexes, such as the ribosomes. The ultimately achievable resolution, however, is still limited by radiation damage,[1–7] as it alters the structure of the sample under investigation and ultimately destroys it.

X-ray radiation damage is generally divided into three categories. Primary radiation damage is a consequence of the direct inelastic interaction between the X-ray photons and the sample. The energy deposited in the sample by inelastic scattering processes and photoelectric absorption is released into a cascade of hundreds to thousands of low energy electrons.[8] These low energy electrons cause radiolytic reactions within the sample, which lead to secondary damage. Both, primary as well as secondary radiation damage, cause localised changes in the molecule and are therefore referred to as specific damage. Another effect caused by X-rays are long-range rearrangements within the sample. This process is called tertiary or global radiation damage. To date, no conclusive model to cover all of these processes involved has been found.

In order to mitigate X-ray radiation damage, the samples are conventionally cooled to 100 K.[9] However, radiation damage is still a major problem, especially in case of biological samples. In order to obtain further mitigation or even fully prevent radiation damage, it is essential to understand the underlying mechanisms of these processes.

Although it was widely believed that radiation damage is mostly non-specific, damage at specific sites of several proteins has been observed.[10–13] This specific radiation damage can be observed, e.g. in the form of the cleavage of disulfide bridges,[14] deamination of amino acids[15] or decarboxylation reactions of acidic residues.[16,17]

Many biological samples, such as metalloproteins or flavoproteins, show X-ray induced photoreduction of their metal centre as the predominant (specific) damage process.[18–21] Such a change in oxidation state alters the structural arrangement in the direct coordination of the metal center. Thus, incorrect structural data from X-ray crystallography makes it difficult to understand the underlying enzymatic reactions in many proteins as the electron densities observed no longer reflect the native state of the protein.[22]

X-ray induced photoreduction of biological molecules has been reported for several elements such as Co(III)[23] (in B12 cofactors), Ni(III)[24,25] (superoxide dismutase) or manganese in higher oxidation states[19,26] (e.g. photosystem II). Complexes containing Cu(II)[27,28] and Fe(III)[21,29] are also known to be reduced upon X-ray irradiation. The consequences and possible mechanisms of X-ray induced photoreduction are widely discussed in the literature.[30–35] Although Compton scattering also occurs upon irradiation with X-rays, the predominant inelastic process is photoelectric absorption. This results in the ejection of a photoelectron. The general consensus in the literature is that this photoelectron directly interacts with the metal center.[36]

Observations show that X-ray induced photoreduction occurs at much lower doses than those typically applied in X-ray crystallography. Therefore, photoreduction cannot occur as a primary event. A possible explanation might be the aforementioned generation of tens to thousands of low energy (low eV) electrons per incident X-ray photon during the inelastic interaction of the photons with the sample.[8] The chemical interaction of these electrons with the sample then causes the photoreduction of the metal centres.

Another factor assumed to play a significant role in the photoreduction process is the presence or absence of water. The free electrons generated by photoelectric absorption and subsequent water photolysis are believed to enhance the photoreduction as well as the general damage process by formation of radicals within the solvent.[16,31] No consensus on the role of water has yet been found.

It is well-known for both, X-ray crystallography and electron microscopy, that the experiment temperature also has a strong influence on radiation damage.[37,38] It has been shown that cryocooling slows down the damage process of biological samples.[39–41] This is believed to be a consequence of the mitigation of diffusion processes of free radicals generated by X-rays. A significantly higher amount of statistically significant X-ray data can be obtained at 100 K compared to measurements at room temperature. However, recent studies at temperatures between 5 K to 100 K have shown that the standard temperature of 100 K might not always be ideal.[37,42–44] Only a few studies have addressed the temperature dependent behavior of the X-ray induced photoreduction process.[21,45,46] Until now, no conclusive results could be obtained.

Another topic widely discussed in the literature is the influence of hydrogen radicals on X-ray induced photoreduction of metal centres and X-ray radiation damage in general.[21,31,35] Recent results show that the interaction of X-rays with organic materials leads to hydrogen formation by cleavage of mainly aliphatic CH-bonds.[37,47] X-ray induced abstraction of hydrogen atoms by photoexcitation of the sample is proposed as an explanation for this process.[48] Due to the X-ray scattering cross section of hydrogen, hydrogen abstraction could not be directly observed, and changes of bond lengths between heavier atoms had to be used as an indicator.

It was the goal of this work to systematically investigate the influence of these different parameters on X-ray induced photoreduction and global radiation damage. The influence of temperature, solvent and chemical composition on X-ray induced photoreduction was investigated using X-ray Absorption Near Edge Spectroscopy (XANES) and high resolution X-ray diffraction. Measurements were performed on the B12 cofactors cyano- and methylcobalamin and four iron compounds, ammonium ferric citrate and potassium hexacyanoferrate (both containing Fe(III)) as well as pyrite and an organic iron sulphur cluster (both containing Fe(II)).

B12 cofactors are of significant importance in the functioning of the human blood production process, the brain and the nervous system. They were first discovered in 1948 as Merc, Sharp and Dohme were able to extract a crystalline red compound from liver tissue.[49] This extract, namely vitamin B12, was later on used to treat several health impairments, such as vitamin B12 deficiency, cyanide poisoning or pernicious anemia.[50]

B12 cofactors possess a Co(III) metal centre surrounded by a corrin ring. Each cofactor is defined by the upper axial ligand of the cobalt, which can be enzymatically exchanged or removed upon protein binding. While methylcobalamin is a biologically active form, that binds to methionine synthase,[51] cyanocobalamin is an artificial cofactor often found in food supplements.[52] Cyanocobalamin is known to be very stable in air but can easily be converted to aquocobalamin through aquation by the human body, making it biologically active. The remaining cyanide only appears in such low doses that it does not have any toxicological effect.[50,53,54]

B12 cofactors offer the possibility to obtain high-quality crystals and thus to collect high resolution X-ray data. Therefore, these B12 cofactors have been selected as ideal models to investigate X-ray induced photoreduction of metal organic compounds or metalloproteins.

Complexes containing iron,[55,56] such as heme proteins,[58–61] are of equal biological relevance, especially in the human metabolism. Ferric citrate plays an important role in the iron uptake of the human body.[62–64] The mechanism of this uptake is still not fully understood, but it is assumed that it goes along with a reduction of the metal centre from Fe(III) to Fe(II). Since X-ray irradiation might also lead to photoreduction from iron(III) to iron(II), care has to be taken when investigating a ferric citrate complex using X-ray methods. In this work, ammonium ferric citrate was investigated in order to obtain information about the X-ray photoreduction process of this complex. Ammonium ferric citrate is well-known to undergo photoreduction already upon irradiation with UV or blue light.[65] The proposed mechanism for this involves a decarboxylation reaction of the citrate ligand.[66,67]

Potassium hexacyanoferrate, also containing the photosensitive Fe(III), is known to not undergo X-ray induced photoreduction.[69] Furthermore, it does not contain hydrogen atoms and was therefore an ideal model to investigate the influence of the chemical composition of the ligand and the presence of hydrogen atoms on X-ray induced photoreduction.

In addition to this, the influence of the chemical composition and the presence of hydrogen atoms within a compound on radiation damage in general were investigated by XANES measurements on pyrite and an organic iron sulphur cluster. Since they both contain Fe(II) no photoreduction was expected. Both compounds contain a Fe_2S_2 cluster, so any different damage behaviour should originate from the difference in their chemical composition. The organic iron sulphur cluster contains hydrogen atoms, whereas pyrite does not. Due to this, these compounds are ideally suited to investigate the influence of hydrogen abstraction on the global damage process.

Single crystal X-ray and neutron diffraction were applied to further investigate the role of X-ray induced hydrogen abstraction from organic molecules and its role in X-ray induced photoreduction and X-ray radiation damage in general. Selective hydrogen abstraction has been proposed as an important factor in global radiation damage and is in agreement with the observation of the temperature dependence occurring in many cases.[37] The formation of hydrogen gas as a result of irradiation with ionising radiation is a well-known phenomenon in electron microscopy.[38] A formation of bubbles formed by radiolytic products upon irradiation with electrons has recently been reported for DNA.[70] Furthermore, it could be observed, that long-term irradiation of crystals of organic compounds with X-rays leads to the formation of gaseous radiolytic products as well. It is assumed that these bubbles consist of hydrogen gas.[37,70,71]

The goal of the combined X-ray and neutron diffraction measurements conducted in this work was to further explore the hypothesis that selective hydrogen abstraction plays an important role in global and specific radiation damage to metal organic and organic samples.

The amino acids L-serine and L-alanine, as well as the nucleoside deoxythymidine (thymidine), which pairs with deoxyadenosine in double stranded DNA,[72] were chosen as model systems for more complex molecules, such as proteins or DNA. All three compounds offered the possibility to grow large crystals, which are required for neutron diffraction experiments. They furthermore allowed the collection of high resolution X-ray data due to their excellent crystal quality.

The single crystal X-ray data, collected in order to investigate X-ray induced photoreduction and selective hydrogen abstraction, were also used to investigate global radiation damage in general and the contribution of these two factors to the global damage process. In single crystal X-ray diffraction, radiation damage is known to lead to a loss in contrast as well as a decrease in diffraction intensity and, thus, a loss in resolution. Expansion of the cell volume, an increase in mosaicity, loss in isomorphism of the sample and an increase of the atomic displacement parameters are also known to occur as consequences of high doses of X-ray radiation.[11,14,16,47,73,74] As a consequence of these structural changes an increase of the reliability index R1, that describes the agreement between the model and the measured structure, is observed.

In addition to the aforementioned measurements, the influence of the standard electrode potential of a metal centre on the susceptibility of a metal organic compound to global radiation damage was investigated in single crystal X-ray diffraction experiments on Ni(II) and Cu(II) complexes of L-serine.

The transition metals Ni(II) and Cu(II) are located right next to each other in the periodic table of elements (atomic numbers 28 (Ni) and 29 (Cu)) and thus differ in their coordination chemistry (square pyramidal for Cu(II), octahedral for Ni(II)).[75,76] Despite this, they display several chemical similarities[76] while differing strongly in their standard electrode potential for a M^{2+}/M^{+} reduction (+0.159 V for Cu(II) to Cu(I), whereas Ni(II) is not reduced to Ni(I),[76] both values at standard conditions and measured in water). Therefore, these compounds allow for investigation of the influence of the standard electrode potential on radiation-induced changes of metal organic compounds.

In the following chapters the basic principles of X-ray diffraction, X-ray absorption, neutron diffraction and X-ray radiation damage are presented. Experimental procedures and sample preparation are explained in all detail in the experimental section of this work. In the results section, the results from this work are presented. A detailed discussion of the findings and a proposed mechanism to describe X-ray induced photoreduction of metal organic compounds and global radiation damage to organic samples is given in the following discussion. In the last chapter, conclusions from the experiments are drawn and an outlook to experiments to further investigate the proposed findings from this work is made.

II Principles

1 X-ray diffraction

This chapter deals with the principles of (single crystal) X-ray diffraction. A more detailed description can be found e.g. in the books by Woolfson[77] and Nielsen.[78]

1.1 Lattice and reciprocal lattice

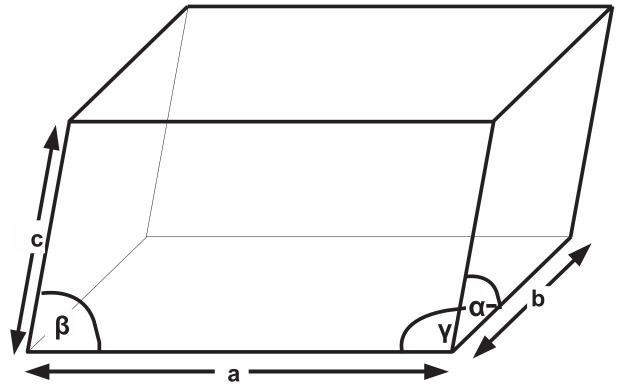

Figure 1.1: Labeling scheme of a unit cell

A three-dimensional crystal is defined as an object that "*consists of atoms arranged in a pattern that repeats itself periodically in three dimensions*".[79]

If the lattice points of a crystal are connected to each other, small parallelepipeds are built. Their repetition by translation from one lattice point to another generates the crystal lattice. A single parallelepiped is called the *unit cell.* In three-dimensional space, it consists of three basic vectors **a**, **b** and **c** (fig. 1.1).

The volume of the unit cell is given by

$$V = abc\left[1 - cos^2\alpha - cos^2\beta - cos^2\gamma + 2 \cdot cos\alpha \cdot cos\beta \cdot cos\gamma\right]^{\frac{1}{2}} \tag{1.1}$$

The geometry within one unit cell defines the crystal system and space group. In three-dimensional space, seven crystal systems (cubic, tetragonal, orthorhombic, hexagonal, rhombohedral, monoclinic and triclinic) and 230 space groups are distinguished.

Crystallographic experiments are carried out using the reciprocal lattice. The reciprocal lattice is the analogue of a crystal lattice in reciprocal space and is defined by the vectors **a***, **b*** and **c*** and the *Miller indices* h, k and l.

$$\mathbf{h} = h\mathbf{a*} + k\mathbf{b*} + l\mathbf{c*} \tag{1.2}$$

where h, k and $l \in N$ and the vectors **a***, **b*** and **c*** are correlated to **a**, **b** and **c** through

$$\begin{array}{lll} \mathbf{a*} \cdot \mathbf{a} = 1 & \mathbf{a*} \cdot \mathbf{b} = 0 & \mathbf{a*} \cdot \mathbf{c} = 0 \\ \mathbf{b*} \cdot \mathbf{a} = 0 & \mathbf{b*} \cdot \mathbf{b} = 1 & \mathbf{b*} \cdot \mathbf{c} = 0 \\ \mathbf{c*} \cdot \mathbf{a} = 0 & \mathbf{c*} \cdot \mathbf{b} = 0 & \mathbf{c*} \cdot \mathbf{c} = 1 \end{array} \tag{1.3}$$

1.2 Scattering

X-rays were first discovered by Wilhelm Conrad Röntgen in 1895[80] and are electromagnetic radiation in the wavelength range of Å (10^{-10} m). For an ideally collimated, monochromatic beam, X-rays can be described by assuming a plane wave $\mathbf{E}(\mathbf{r} \cdot t)$:

$$\mathbf{E}(\mathbf{r} \cdot t) = \hat{\epsilon} \cdot \mathbf{E}_0 \cdot exp\left[i(\mathbf{k} \cdot \mathbf{r} - \omega \cdot t)\right] \tag{1.4}$$

where $\hat{\epsilon}$ is the polarisation perpendicular to the propagation direction of the plane wave. Each photon has an energy $\hbar\omega$ and a momentum $\hbar\mathbf{k}$.

X-ray diffraction experiments utilise the interaction between electromagnetic waves and

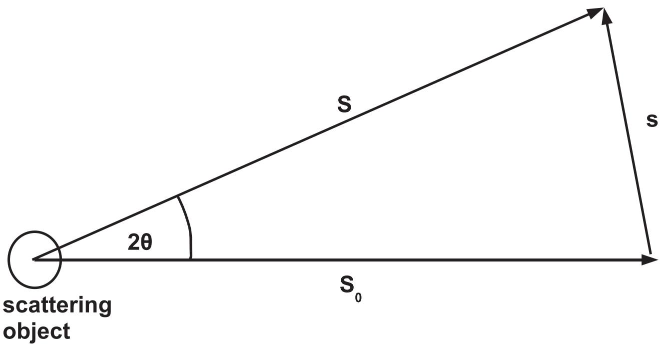

Figure 1.2: Definition of the scattering vector **s** in a diffraction experiment.

matter. They are used for determination of the lattice, intensity and symmetry of a crystal.

Coherent Thomson scattering is the most important component of the elastic scattering process exploited in X-ray diffraction measurements. It leads to a fixed phase relation between the diffracted waves from each atom. During a measurement, the electrons within the sample are excited to oscillations in the electric field of the incident beam. Since the mass of a nucleus of an atom is large as compared to that of an electron, the movement of the nuclei cannot follow the electron oscillations. Thus, electrons are the primary scattering unit of X-ray radiation.

1.2.1 Scattering vector and constructive interference

A more graphical approach to the scattering process of X-rays in crystals is the *scattering vector* **s**. It is defined as the difference vector of the incident beam $\mathbf{S}_0$ and the diffracted beam $\mathbf{S}$ where $|\mathbf{S}| = |\mathbf{S}_0| = 1/\lambda$. The angle between $\mathbf{S}_0$ and $\mathbf{S}$ is denoted 2θ (see fig. 1.2).

$$\mathrm{s} = \mathbf{S} - \mathbf{S}_0 \tag{1.5}$$

Crystals are three-dimensional, periodic structures. Therefore, the allowed diffraction angles in a crystal are determined by the wavelength of the X-ray radiation and by the repeat distances of the periodicity of a crystal. Constructive interference of the diffracted waves at single crystals can be observed, if the *Laue equations*

$$\mathbf{a} \cdot \mathbf{s} = h \quad \mathbf{b} \cdot \mathbf{s} = k \quad \mathbf{c} \cdot \mathbf{s} = l \tag{1.6}$$

are fulfilled concurrently. Hereby h, k and l have to be integer numbers. As can be derived easily from eq. 1.3, the Laue equations are fulfilled for all points of the reciprocal lattice. Therefore, constructive interference of the scattered waves can be observed for $\mathbf{h} = \mathbf{s}$.
A scalar approach of the Laue equations is the *Bragg equation*

$$\lambda = 2d_{\mathbf{h}} sin\theta \tag{1.7}$$

which describes the relation between the diffraction angle 2θ, the distance $d_{\mathbf{h}}$ between two lattice planes and the wavelength λ. Hence, constructive interference only occurs if wavefronts that have been scattered at different lattice planes propagate in the same phase. Otherwise the interference will be destructive. This superimposition of interference maxima and minima leads to clearly defined Bragg spots. Their intensity, shape and distribution is influenced by different factors. These factors will be explained in the following sections.

1.2.2 Structure factor and atomic form factor

An X-ray diffraction experiment does not provide a real space image, but the modulus of the Fourier transform of the electron density distribution $\rho(\mathbf{r})$ of the sample:

$$F_{cryst}(\mathbf{s}) = \int_V \rho(\mathbf{r}) exp[2\pi i \cdot \mathbf{r} \cdot \mathbf{s}] dV \tag{1.8}$$

As mentioned before, constructive interference will only occur in case of $\mathbf{h} = \mathbf{s}$. Therefore, the integral in eq. 1.8 can be quantised to a sum over all unit cells

$$F_{cryst}(\mathbf{h}) = F(\mathbf{h}) \sum_{\mathbf{g}} exp[2\pi i \cdot \mathbf{h} \cdot \mathbf{g}] \tag{1.9}$$

where $F(\mathbf{h})$ is the so called structure factor:

$$F(\mathbf{h}) = \sum_{j=1}^{N} f_j(\mathbf{h}) exp[2\pi i \cdot \mathbf{h} \cdot \mathbf{r}_j]. \tag{1.10}$$

f_j is named the atomic form factor and describes the scattering ability of a single, free atom j within a unit cell. $\mathbf{r}_j$ describes its position within the unit cell. The atomic form factor is defined as the Fourier transform of the electron density $\rho(\mathbf{r})$ of the respective atom

$$f_j(\mathbf{s}) = \int \rho(\mathbf{r}) exp[2\pi i \cdot \mathbf{r} \cdot \mathbf{s}] dr^3 \tag{1.11}$$

1.2.3 Friedel's law

Friedel's law states that in the absence of anomalous scattering

$$I(\mathbf{h}) = I(\bar{\mathbf{h}}) \tag{1.12}$$

holds for one scattering process. Accordingly, it can be said that even if the crystal structure lacks a centre of symmetry, the diffraction pattern will be centrosymmetric. The crystal then appears to be in one of the 11 Laue groups.

Friedel's law fails when anomalous scattering becomes significant. A pair of reflection sets (h, k, l) and $(\bar{h}, \bar{k}, \bar{l})$, known as a Friedel pair, will then show a small difference in their respective intensities. This can be used to determine the absolute configuration of a molecule.[81,82] It is important to note that even for a high contribution of anomalous scattering Friedel's law stays valid for centrosymmetric structures.

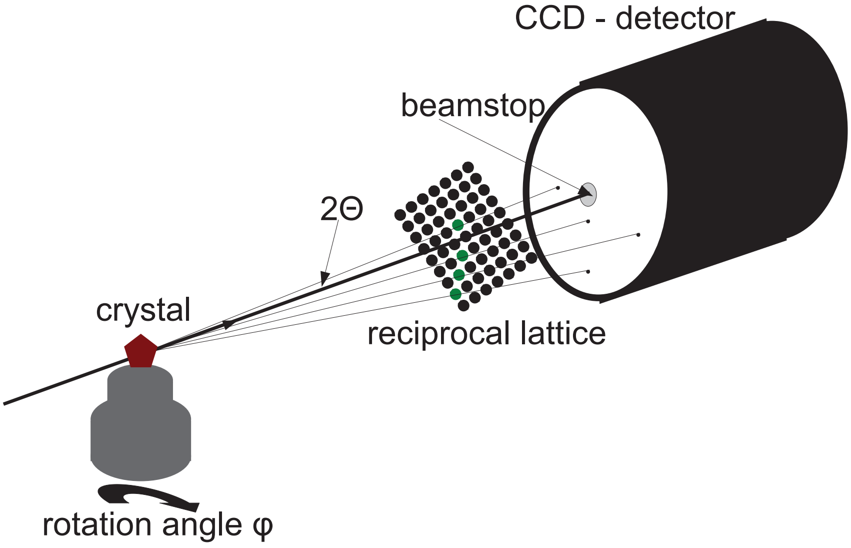

Figure 1.3: Basic setup for X-ray data collection of single crystals by rotation photographs.

1.3 Data collection

X-ray data collection is performed on single crystals by taking rotation photographs using a 2-D detector: During the collection of a rotation photograph the shutter is opened and the crystal is rotated at a constant angular velocity for a defined angle increment while being exposed to the X-ray beam. After that, the shutter is closed and the rotation is stopped. The detector is then read out. All lattice points that fulfill eq. 1.7 during that rotation can be observed in the respective image. Fig. 1.3 shows the basic alignment of such an experiment. The crystal is rotated around φ. For each φ different points of the reciprocal lattice fulfill eq. 1.7 (marked green in fig. 1.3). Thus, the image of Bragg peaks appearing as result of the constructive and destructive interference of the scattered radiation varies depending on the orientation.

A complete dataset will include all Bragg peaks and is completed after a full 360° rotation, although, depending on the crystal symmetry, a full rotation is not always necessary to collect all Bragg peak positions. Evaluation programs can be used to assign an index (hkl) to each Bragg reflection and determine the reflection intensity.

2 X-ray absorption

The following section provides a short overview over X-ray absorption spectroscopy, which is based on the effect of photoelectric absorption. A more detailed description can be found in the literature.[77, 78, 83, 84]

2.1 Absorption

Absorption of X-rays is the second important photon-matter interaction. The resulting intensity through a sample is given by

$$I(d) = I_0 exp(-\mu d) \tag{2.1}$$

where I_0 is the incident intensity, μ is the linear absorption coefficient and d the sample thickness.

Upon ***photoelectric absorption*** of an X-ray photon the energy is transferred to an electron and this electron is ejected from the atom if the photon energy is higher than the electron binding energy. During this process, a hole is created in the inner shells of an atom. The following processes can then take place when this hole is filled by an electron from an outer shell:[78]

- The energy difference between the binding energies of the electron from the outer and inner shell is simultaneously emitted in form of a photon of the respective energy. This process is called ***fluorescence***.

  Due to the very specific energy transitions for each atom in a molecule, the resulting

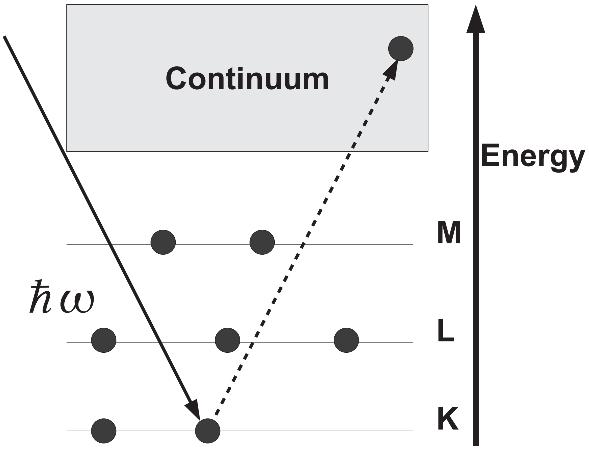

Figure 2.1: Photoelectric absorption process.

monochromatic fluorescence is a specific fingerprint of each atomic species.

- The energy difference between the binding energies is transferred to another electron in the atom. This leads to an ejection of the respective electron. This process is called ***Auger emission*** and the secondary emitted electron is called Auger electron.

The absorption coefficient μ(E) of a material, which describes how strongly X-rays are absorbed, has a distinct dependence on the incident photon energy. Generally, it decreases with increasing energy (roughly following 1/E^3). At energies characteristic for each atom within a material the absorption cross section σ_a, which is proportional to μ(E) shows jumps. These jumps are called absorption edges and originate from photoelectric absorption.

If the binding energy of an electron is higher than the energy of the incident photon photoelectric absorption is no longer possible and the absorption cross section decreases again. Photoelectric absorption is the main contributor to the absorption cross section whenever the photon energy is much smaller than the mass of an electron. The photoelectric absorption cross section varies with Z^4, where Z is the atomic number of the absorber. The resulting material specific behaviour of the absorption cross section is exploited in XANES and EXAFS^{86} measurements.

2.2 EXAFS and XANES

X-ray Absorption Spectroscopy (XAS) exploits details during the absorption of high energy photons by matter. In contrast to UV or visible light spectra, X-ray photons excite and liberate inner shell electrons. The photoelectron wave scatters from the atoms in the direct vicinity of the absorbing atom and leads to interferences between the outgoing and scattered parts of the photoelectron wavefunction. This interference leads to an energy-dependent variation in the probability of X-ray absorption. This probability is proportional to the X-ray absorption coefficient. Therefore the X-ray absorption coefficient is the quantity measured in X-ray absorption spectroscopy.

X-ray absorption spectra are usually divided into two regions, the XANES (X-ray Absorption Near Edge Spectroscopy) region and the EXAFS (Extended X-ray Absorption Fine Structure) region, which can be seen in fig. 2.2 for a spectrum of Molybdenum metal.[85]

The features of an X-ray absorption spectrum are listed below.

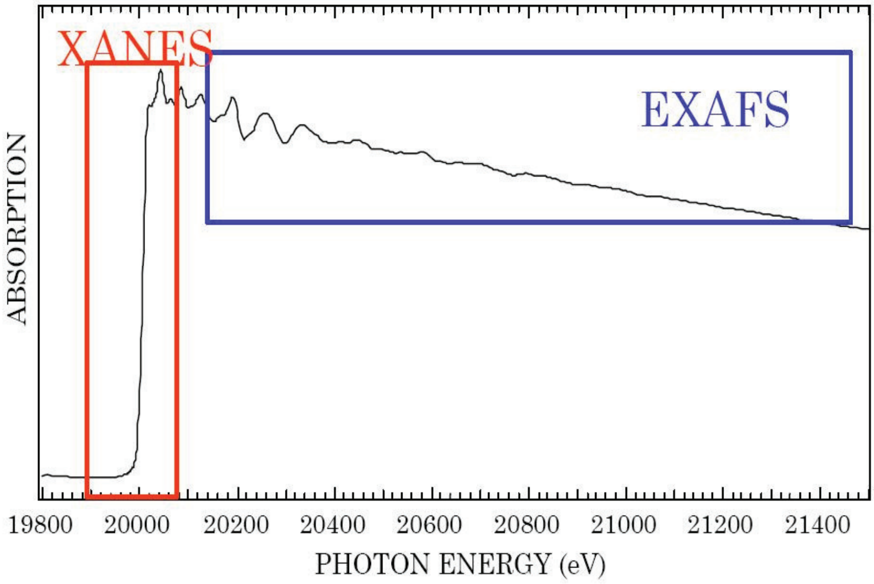

Figure 2.2: X-ray absorption spectrum of Molybdenum metal showing the distinction between the XANES and the EXAFS region.[85]

- Especially in case of transition metal XANES, pre-edge peaks can be found in the region below the absorption edge. They are correlated to the valence of the absorbing atom and provide information about the electron transitions between different shells, following dipole-selection rules. Furthermore weaker pre-peaks appear, due to quadrupole-allowed electron transitions.

- An important part of the XANES component of a spectrum is the region around the absorption edge. The energy-position of the absorption edge is a measure for the chemical valency of the absorbing atom. In case of transition metals, the oxidation state of the metal under investigation can be determined by the position of the absorption edge.

- The edge peak(s) - also called the white line(s) - are part of the XANES-region. They correspond to transitions of core electrons to unfilled bound states close to the continuum of the absorbing atom and therefore offer information about these electronic states.

- The EXAFS region above the white line consists mainly of the gentle oscillations which result from the interference of the outgoing photoelectron wave with the backscattered wave from the atoms in the immediate vicinity of the absorbing atom. These oscillations carry information about number, species and distance of the atoms close to the absorbing atom.

Usually the pre-edge as well as the edge region are investigated in XANES experiments while the oscillations are investigated in EXAFS experiments. Due to the high sensitivity of the edge region to the atomic valency of the target atom, XANES is a well-suited tool to probe the oxidation state of a sample. The position of the absorption edge is independent of the aggregation state of the sample, so a wide range of samples can be investigated with this method.

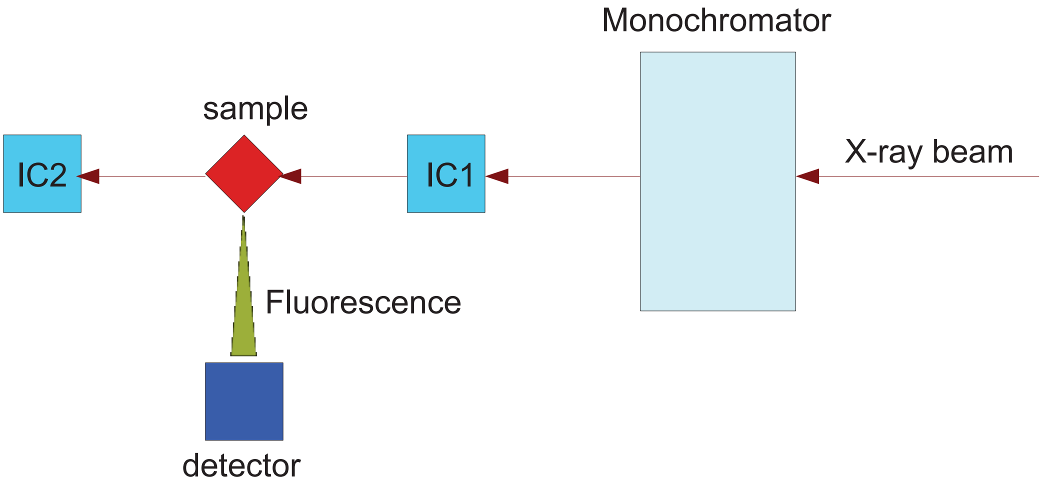

Figure 2.3: Experimental setup of a XAS experiment for either transmission (IC1 and IC2) or fluorescence (IC1 and fluorescence detector) measurements.

2.3 Data collection

XAS experiments can be performed in transmission or fluorescence mode. Figure 2.3 shows the basic experimental setup at a synchrotron source. A double crystal monochromator is used to produce monochromatic X-rays. During data collection the X-ray energy is changed in defined steps for a defined energy spectrum. The incident beam intensity is determined by a first ion chamber. Behind this chamber, the beam hits the sample. In transmission mode, a second ion chamber is used to determine the intensity transmitted through the sample.

In fluorescence mode, an energy sensitive detector is used to collect the fluorescence photons emitted from the sample. To minimise the contribution from scattering processes in this case, the detector should be aligned in an 90° angle to the beam axis. In this case the polarisation factor for Thomson scattering of linearly polarized synchrotron light equals 0. Analysis of XAS spectra is usually performed by using a normalised absorption coefficient (μ_{norm}).

3 Neutron diffraction

This section deals with the most important principles of neutron scattering. More detailed information about neutron scattering on single crystals can be found in the literature.[87,88] The diffraction experiments conducted in the frame of this thesis were usually performed with neutrons of a wavelength of 1.8 Å (energy of 0.025 eV).[89] Their de-Broglie wavelength is in the range of interatomic distances in solids and liquids, which makes these **thermal neutrons** an excellent tool for the investigation of matter.[90]

3.1 Elastic neutron scattering

The principles of single crystal neutron diffraction are similar to those of X-ray diffraction. Single crystal neutron diffraction can be seen as a complementary method to X-ray diffraction because the scattering lengths of neutrons for certain elements do not directly depend on the atomic number Z. Neutrons are uncharged, hence, they do not face the Coulomb barrier. This means they are not diffracted by the electron distribution in the sample, but scattered by nuclear forces. Therefore, it is possible to determine the position of the nucleus independent of the electron distribution in the sample.

The scattering length of each nucleus is isotope-specific. Hydrogen - which is poorly visible in X-ray diffraction experiments - has a very high scattering cross section for neutrons and can thus directly be observed in a neutron diffraction experiment.

However, hydrogen scattering contains a large inelastic component, which might complicate data evaluation. Since deuterium does not show this strong inelastic scattering component, it is more viable to deuterate a sample containing large amounts of hydrogen prior to a neutron experiment. The cross sections of hydrogen and deuterium are different in sign. This allows for contrast variation within experiments.

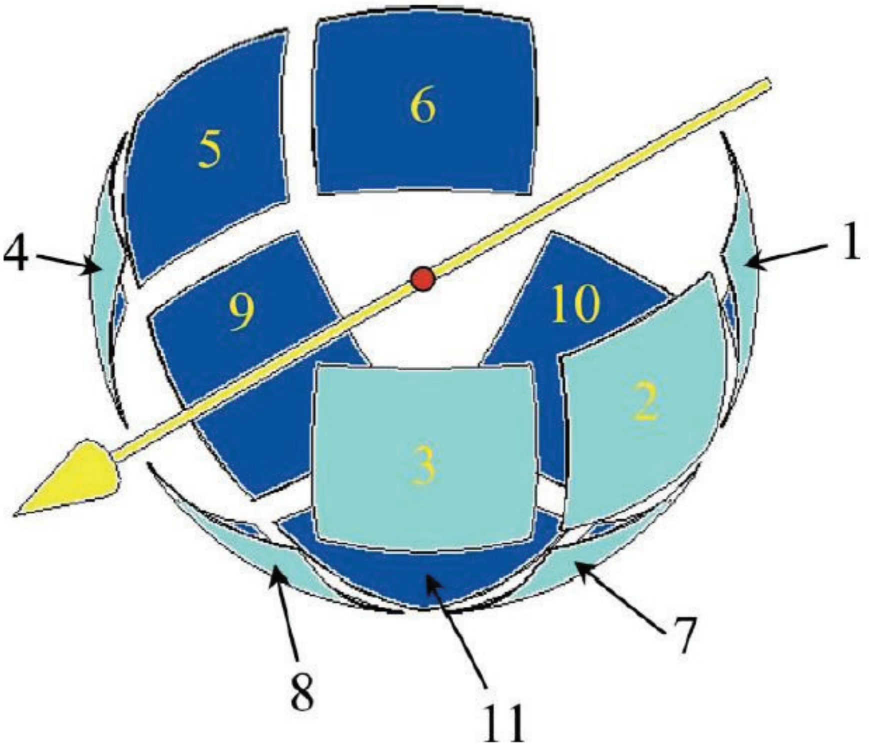

Figure 3.1: Detector arrangement of the ISIS SXD-beamline.[91] Each detector is assigned a number that is used for indexing all reflections.

3.2 Neutron sources

Neutrons can be produced either by nuclear fission in reactors or by spallation sources.[92] Nuclear reactors produce large amounts of neutrons, which can then be moderated to thermal neutrons and used for neutron scattering experiments.

Spallation sources utilise a high-power accelerator, such as a synchrotron, that focuses an intense proton beam onto a spallation target. When the proton hits the target, spallation particles, such as neutrons and muons, are produced. Due to the high energy of the neutrons, moderators are used to slow down the neutrons to a thermal level.

Wavelength selection of the neutron beams can be achieved by various methods, such as utilisation of a neutron chopper, in which velocity and tilting angle are used for selection of the wavelength or of a single crystal monochromator, by which Bragg reflected neutrons are used in selective angular ranges corresponding to the respective energy and wavelength.[93] The flux of neutron beams is small compared to that of an X-ray beam. In order to minimise the time needed for a structure solution larger crystals are required.

3.3 Data collection

In many cases, time-of-flight measurements with polychromatic beams are applied for neutron diffraction. This way the energies of the incident neutrons can be sorted easily and no monochromator has to be used. For this, a number of time-resolving detectors is arranged around the sample for data collection to cover a large solid angle.

Such an alignment can be seen in fig. 3.1[91] where the detector arrangement of the ISIS SXD-beamline is shown.

4 X-ray radiation damage

X-ray radiation damage to biological samples is a major limitation for obtaining structural information from radiation sensitive samples by X-ray methods.[94] Cryocooling to liquid nitrogen temperatures is known to slow down this damage process and, thus, is commonly applied in many experiments. It is assumed that the diffusion processes of radicals created during X-ray irradiation are slowed down at lower temperatures.[7,37,95,96] Although the origin and consequences of X-ray radiation damage have been investigated extensively, the underlying processes are still not fully understood.

X-ray radiation damage is known to result from inelastic scattering processes and photoelectric absorption. In contrast to early assumptions, it is not a purely stochastic process.[95] Radiation damage can be classified into three categories: *Primary* radiation damage, *secondary* damage and *tertiary* radiation damage. Primary radiation damage originates from the direct interaction between X-ray photons and the sample. Compton scattering and photoelectric absorption cause the formation of tens to thousands of low energy (low eV) electrons in an electron cascade.[8] Secondary radiation damage is a result of the radiolytic reactions caused by these electrons. Possible results of primary and secondary damage are bond cleavage of specific bonds, generation of free radicals in the sample and the surrounding solvent and decarboxylation as well as redox reactions. Such localised damage processes are also referred to as *specific* radiation damage.

Long-range rearrangements between different molecules within a sample are referred to as tertiary damage and also as *global* damage.[95]

In crystallography, global radiation damage manifests itself in a loss of crystalline order and, thus, a decrease in diffraction power. The global damage process can be followed by the analysis of different parameters.

Due to the nature of the global damage process, the indicators used for global radiation damage are not suited to follow the damage progression within a crystal on an atomic scale from its very first onset. As mentioned before, specific damage occurs before global damage can be observed.[14] The effects of specific radiation damage can therefore already be significant before global damage indicators show measurable changes.

Nowadays, an experimental temperature of 100 K is commonly applied in X-ray crystallography on biological samples. Cooling to temperatures of 50 K has been demonstrated to further mitigate radiation damage.[37] This can be explained by the fact that upon irradiation, mainly hydroxyl as well as hydrogen radicals are produced. At temperatures below 100 K the hydroxyl radicals cannot diffuse anymore and, thus, cause less damage. Hydrogen radicals, however, can still diffuse and prevent pronounced damage to the crystal structure. It has been shown that cooling down to 30 K, which is the temperature at which hydrogen radicals become immobile, is therefore not effective due to the resulting trapping of hydrogen gas within the crystal. This trapping leads to a deterioration of the crystalline structure.[37, 42]

It has been proposed that the presence of solvent has a strong influence on the susceptibility of a compound to radiation damage. Solvent molecules are suspected to favour the formation of radiolytic products that can diffuse within the sample. This is assumed to accelerate the damage progression via radical diffusion.[14, 16]

This work investigates the origin and nature of several specific as well as global damage processes. In the following sections the main indicators of radiation damage to crystalline as well as non-crystalline samples are presented.

4.1 Global radiation damage

This work investigates global radiation damage by application of single crystal X-ray diffraction. Global radiation damage affects several parameters describing a crystalline sample.[11,14,16,47,73,96] The most important indicators of global X-ray radiation damage are summarised in this section.

4.1.1 Wilson-Plot, B-factor and mean intensity

In general, the positions of atoms within a unit cell are considered to oscillate around their mean equilibrium positions. For a first approximation, these positions are considered to follow a Gaussian distribution around their mean value. Deviation from these mean positions can be either dynamic due to thermal vibrations, which is the predominant contribution in case of small molecules, or static, e.g. in forms of disorders between different unit cells, which is the predominant contribution in case of macromolecular crystals. In order to take this effect into account, the so-called temperature factor or *B-factor* B has been introduced.

Assuming the thermal vibrations are isotropic and the values of B are equal for all atoms, the scattered intensity for a certain temperature is defined as

$$I(\mathbf{h})_T = I(\mathbf{h}) exp\left[-2 \cdot B \cdot sin^2\Theta/\lambda^2\right] \tag{4.1}$$

The exponential term is the well-known *Debye-Waller factor.* It is assumed in eq.4.1 that the B-factor has the same value for all atoms ("global B-factor").

A straight-forward method to determine the global B-factor of a structure was first suggested by Wilson[97] and is thus called a *Wilson-plot.* The (polarisation and Lorentz corrected) intensity of each reflection is given by

$$I(\mathbf{h}) = K \left|F_{\mathbf{h}_r}\right|^2 exp\left[-2 \cdot B \cdot sin^2\Theta/\lambda^2\right] \tag{4.2}$$

where K is a scaling factor, $F_{\mathbf{h}_r}$ the structure factor of the atoms in their equilibrium position, Θ can be deduced from the diffraction angle 2Θ and λ is the wavelength. Assuming a statistical distribution of the atoms within the unit cell the mean value of the structure factor for N atoms can easily be determined.

The loss of crystalline order upon exposure to high doses of X-ray radiation leads to a decrease in Bragg reflection intensity. This loss in intensity first becomes visible for reflections in the high resolution range. In data evaluation processes of single crystal X-ray diffraction, the loss in Bragg intensity is investigated using the so-called *mean intensity*. It is calculated by integration over all Bragg reflection intensities. For a number of observed intensities within a narrow range of $sin\Theta$ the mean intensity is described as

$$\langle I_\Theta \rangle = K \left\langle \left| F_{\mathbf{h}_r} \right|^2 \right\rangle exp\left[-2 \cdot B \cdot sin^2\Theta/\lambda^2 \right] \tag{4.3}$$

The mean intensity decreases as function of dose.

With $\left\langle |F_r|^2 \right\rangle = \Sigma_\Theta$ eq.4.3 can be written as

$$ln\left\{ \frac{\langle I_\Theta \rangle}{\Sigma_\Theta} \right\} = lnK - 2 \cdot B \cdot sin^2\Theta/\lambda^2 \tag{4.4}$$

If $ln\left\{ \frac{I(\Theta)}{\Sigma_\Theta} \right\}$ is plotted as function of $sin^2\Theta/\lambda^2$ a straight line with axis intercept lnK and slope $-2 \cdot B$ is obtained.

In order to compare two or more datasets to each other, the *relative Wilson B-factor* can be used. It is a factor obtained from scaling of two or more datasets with XSCALE according to the formula

$$I_{\Theta sc} = K I_{\Theta meas} exp\left[-2 B_{rel} sin^2\Theta/\lambda^2 \right] \tag{4.5}$$

where B_{rel} is the relative B-factor and $I_{\Theta sc}$ and $I_{\Theta meas}$ are the scaled and measured intensities.

If X-ray radiation induces changes to the crystalline order, this is reflected in the Wilson B-factor. Significant structural rearrangements result in an increase of the relative Wilson B-factor with dose.

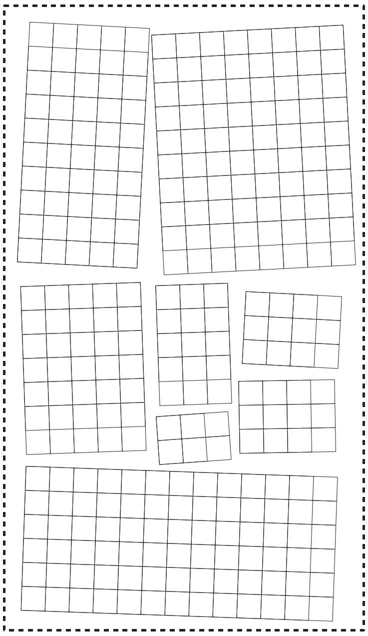

Figure 4.1: Graphical illustration of crystal mosaicity.

4.1.2 Correlation coefficient

The correlation coefficient describes the correlation between two datasets. It is defined as

$$cc_F = \frac{\sum_h F_h^1 F_h^2 - \sum_h F_h^1 \sum_h F_h^2/N}{\left\{\left[\sum_h (F_h^1)^2 - (\sum_h F_h^1)^2/N\right]\left[\sum_h (F_h^2)^2 - (\sum_h F_h^2)^2/N\right]\right\}^{1/2}} \tag{4.6}$$

with N being the number of reflections and F_h^1 and F_h^2 the respective reflection sets. With increasing dose the correlation between the measured datasets and the reference dataset decreases. In this work the reference dataset is usually the first dataset that is collected.

4.1.3 Crystal mosaicity

Real crystals are not perfectly periodical objects. A real single crystal consists of small mosaic perfect blocks in the order of microns, which are slightly misaligned with respect to each other.

In fig. 4.1 a graphical explanation of the principle of *crystal mosaicity* is shown. The gaps between every perfect block are non-parallel and, thus, each block has its own orientation within the single crystal. This orientation is commonly distributed over an angular range from close to 0.0 to several tenth of a degree. Consequently, no systematic phase relation is given for the radiation that is scattered from different parts of a crystal. Therefore, the total intensity is obtained by adding up all intensities from different regions of the crystal. Two aspects of mosaicity influence the shape of the reflections observed on the detector: the size of each block and the angular distribution of the blocks.

The mosaicity of a crystal is also affected by X-ray irradiation. Radical and gas formation within a crystal are known to be consequences of X-ray radiation damage. This exerts a disruptive force on the crystal lattice, which leads to an increase in mosaicity.

4.1.4 Unit cell volume

It has been observed that in most cases the *unit cell volume* of a crystal increases upon irradiation.[5, 11, 14, 16, 73]

4.1.5 R1 value from structure refinement

The agreement between the model amplitudes and the amplitudes determined from an experiment is expressed by the so-called *reliability index* or R1-value:

$$R1 = \frac{\sum ||F_o| - |F_c||}{\sum |F_o|} \tag{4.7}$$

where the sum over all structure factors is taken into account. The lower the R1 value the higher the agreement.

With increasing X-ray dose the alterations within the molecules become more prominent. Hence the agreement between the model and experimentally determined structure decreases. Thus, radiation damage leads to an increase in R1 value from structure refinement.

4.2 Specific radiation damage

Damage located at a specific site of the sample is referred to as specific radiation damage. In this section the special cases of specific X-ray radiation damage relevant for this work are presented.

Important examples for pecific radiation damage are cleavage of disulfide bridges,[14] deamination of amino acids,[15] decarboxylation reactions of acidic residues[16,17] or X-ray induced redox reactions, which occur at specific sites such as metal centres.[18–21] In this work, X-ray induced oxdidation state changes are directly followed by X-ray Absorption Near Edge Spectroscopy (XANES).

Furthermore, single crystal X-ray diffraction and single crystal neutron diffraction were applied to follow specific changes upon X-ray irradiation on the atomic level.

4.2.1 X-ray induced photoreduction

Redox state changes of metal organic compounds and metalloproteins play an important role in many chemical and biological processes, e.g. as homogeneous catalysts used in chemical synthesis or in photosynthesis. Therefore, X-ray induced photoreduction to metal centres of such compounds is a severe problem which has been addressed in the literature for samples like Photosystem II[19] (PSII) and B12 cofactors.[23] X-ray induced photoreduction occurs at doses of a magnitude lower than for global radiation damage[19,23,35,45,46] and is not as significantly mitigated upon cooling as the global events.[35]

Photoionisation is an event leading to X-ray induced photoreduction. The core electrons within lighter atoms such as oxygen, carbon or nitrogen are liberated by the incident X-ray photons. A cascade of secondary ionisation events then leads to the formation of radicals and to the population of excited states.[98,99] This in turn leads to reactions within the compound resulting in the photoreduction of the metal centre.

A slightly higher susceptibility to X-ray induced radiation damage and X-ray induced photoreduction was observed for compounds in solution.[19] This might be a consequence of the mediation of hydroxyl radicals upon irradiation with X-rays.

Spectroscopic measurements on PSII have shown that X-ray induced photoreduction seems to be directly proportional to the aborbed X-ray dose.[35] It could also be demonstrated that the oxidising potential of a metal site has an influence on the photoreduction rate.[46] Due to the temperature dependent behaviour of the X-ray induced photoreduction process of PSII, it was assumed that protein dynamics are rate-limiting the radical chemistry by influencing the electron transfer steps leading to the reduction of the metal centre.[35]

This work mainly investigates the X-ray induced photoreduction of B12 cofactors using XANES and X-ray diffraction. The photoreduction process in B12 cofactors most probably corresponds to the reaction Y-Co(III)-X + $e^{\ominus} \rightarrow$ Y-Co(II)-X, where Y is the lower and X the upper axial ligand.[23]

Previous investigations have shown that not all B12 cofactors with a Co(III) centre are photoreduced upon irradiation with X-rays[23] and a commonly applicable model for X-ray induced photoreduction of B12 cofactors has not been found so far.

X-ray induced photoreduction is known to cause rearrangements in the neighbourhood of the metal centre. It is not possible to determine the oxidation state directly from X-ray diffraction experiments. However, bond length changes around the metal centre caused by photoreduction can be observed using this method.

The oxidation state of a sample can be probed directly in XANES measurements by investigation of the position of the absorption edge.[23, 83, 85] A shift in the edge position towards lower energies implies a reduction; a shift to higher energies implies an oxidation of the sample. The value E_0, which is the energy at which $x\mu_{norm}$ see eq. 2.3 in the “Principles” section) reaches 0.5, was chosen as a measure of the absorption edge position in the XANES investigations presented in this work.

4.2.2 Hydrogen abstraction

Recent studies have shown that the abstraction of hydrogen atoms from specific sites of a molecule is a main contributor to global radiation damage in crystalline samples.[37,47] The abstracted hydrogen atoms form hydrogen gas that can diffuse through the crystal. This exerts a disruptive force on the crystal and increases the crystal mosaicity.

Hydrogen atoms are only poorly visible in X-ray diffraction experiments. However, it is possible to investigate bond length changes caused by the abstraction of hydrogens. In contrast to their poor visibility in X-ray diffraction, hydrogen atoms can be observed well in neutron diffraction. Therefore, hydrogen abstraction can directly be investigated in neutron diffraction experiments. Here, the position of the hydrogen atoms can be directly derived from the nuclei density maps.

III Experimental

1 X-ray diffraction measurements

In this chapter the experimental procedure for radiation damage studies by single crystal X-ray diffraction is explained. It was the goal of these studies to obtain a model to describe the global damage process. Furthermore, localised structural changes occuring upon X-ray irradiation were investigated.

The B12 cofactors cyanocobalamin and methylcobalamin as well as the metal amino acid complexes were investigated in order to gain a deeper understanding of the contribution of X-ray induced photoreduction to the global damage process.

The amino acids L-serine and L-alanine, as well as the nucleoside thymidine were investigated to obtain further information about the influence of selective hydrogen abstraction on the global damage process.

1.1 X-ray diffraction experiment strategy

This section presents the beamline parameters and experimental strategy for X-ray diffraction measurements. Information about the data evaluation procedure and data analysis to investigate X-ray radiation damage in single crystals are given.

1.1.1 Beamlines

PXI (X06SA) - Swiss Light Source

PXI is an undulator beamline for macromolecular crystallography. The beamline is equipped with a fixed-exit Si(111) double crystal monochromator. The second crystal is bendable and used for sagittal focusing. A dynamically bendable mirror is used for meridional focusing. The assigned photon flux of PXI at an energy of 12.4 keV and a ring current of 400 mA is above 2×10^{12} ph/s.

The beamline is equipped with a Pilatus 6M detector, an open-flow nitrogen cryojet and a high precision air-bearing rotation axis. The focused beam size is $85 \times 10\ \mu m^2$ (h × v). The energy range of the beamline is 5.7 to 17.5 keV. The closest sample-to-detector distance is 150 mm.

PXIII (X06DA) - Swiss Light Source

PXIII is a super-bending magnet macromolecular crystallography beamline with a 2.9 T magnet and a critical energy of 11.46 keV. The beamline optics consist of a vertically collimating mirror followed by a four bounce Si(111) monochromator and a toroidal mirror for vertical and horizontal focusing of the beam. At an energy of 12.4 keV and a ring current of 400 mA, the photon flux of PXIII is 5×10^{11} ph/s.

The beamline is equipped with a mar225 mosaic CCD detector, an open-flow nitrogen cryojet and a high precision air-bearing rotation axis. The focused beam size is $80 \times 45\ \mu m^2$ (h × v). The energy of the beamline ranges from 6.0 to 17.5 keV. The closest sample-to-detector distance is 60 mm.

X13 - DORIS III

The EMBL-beamline X13 is a bending magnet macromolecular crystallography beamline at DORIS III. The beamline optics consist of a Si(111) single crystal monochromator and a bending mirror for horizontal and vertical focusing of the beam. The maximum photon flux at an energy of 14.76 keV, a ring current of 190 mA and for a beam size of 0.3 × 0.3 mm^2 is 2×10^{10} ph/s.

X13 is equipped with a marCCD 165mm detector and an open-flow nitrogen cryojet. During experiments, the beam size was slit down to 0.3 × 0.3 mm^2 (h × v). X13 is a fixed energy beamline operated at 15.3 keV. The closest sample-to-detector distance is 35 mm.

1.1.2 X-ray data collection

Data collection was performed using rotation photographs of single crystals (see section 1.3 of the ***"Principles"*** section). For this method the crystal is accelerated to a defined angular velocity and then rotated for a fixed angle increment $\Delta\varphi$ at a constant velocity during exposure to the beam.

In case of the marCCD detectors, which use a shutter, this shutter is opened and the crystal irradiated while rotated. The crystal rotation is stopped after measurement of each angle increment and the shutter is closed. The detector is then read out.

The Pilatus 6M enables shutterless operation. In this case the shutter is open all the time and the crystal is constantly rotated with a fixed velocity. The detector is read out at defined frequencies.

In order to follow radiation induced changes, the following strategy was applied: Series of adjacent complete datasets from the same sample were collected using rotation photographs. A complete dataset is defined as a full 360° rotation.

Depending on the photon flux and crystal size, up to 65 complete datasets were collected until a decrease in diffraction spot quality and loss in (high) resolution became visible. In the following text this procedure is referred to as *dose series*.

1.1.3 Data evaluation and structure refinement

Data integration, analysis of diffraction spots and lattice parameters as well as structure refinement of each dose series was automated with Perl scripts. In the automated process each dataset was evaluated with the XDS package[100] using the same input file. Afterward, reprocessing of the data at a fixed sample-to-detector distance was performed with XDS in order to obtain more precise unit cell parameters. All datasets of a dose series were scaled and merged using XSCALE. Structure solution and refinement was performed by direct methods using SHELX.[101] An initial model for refinement was determined from the first dataset. All subsequent datasets of a dose series were then refined automatically against this model.

1.1.4 Diffraction parameters to follow radiation damage

Each dataset out of a dose series was evaluated in the same way. Several Perl scripts were written to extract parameters from data processing with XDS and XSCALE as well as structure parameters from refinement with SHELX. These parameters were further used to analyse radiation damage as function of dose.

Due to the differences in photon flux, crystal size, unit cell volume and R1 values from structure refinement, normalised values were used when necessary. For normalisation the absolute values were divided by the starting value of each series of parameters. The parameters were then zero-dose corrected.

Parameters from data evaluation with XDS and XSCALE

The effects of global radiation damage were followed by investigation of the

- *Mean intensity*: The mean intensity is defined in eq. 4.3 in chapter 4 of the ***"Principles"*** section and is well known to decrease with dose. It was extracted from the merged datasets from XSCALE.

- *Mosaicity*: The mosaicity can be used as a rough estimate of the crystalline order. The mosaicity is known to increase with dose, since the crystalline order usually decreases as a consequence of global radiation damage. It was extracted from XDS for each dataset of a dose series. Since the mosaicity is influenced by the properties of each crystal, care has to be taken when comparing mosaicities of different crystals to each other.

- *Correlation coefficient*: The correlation coefficient is defined in eq. 4.6 in chapter 4 of the ***"Principles"*** section. Radiation induced changes lead to a decrease in correlation between the current and the reference dataset. The correlation coefficient was extracted from the merged datasets from XSCALE.

- *Relative Wilson B-factor*: Hereafter called "relative B-factor", this factor increases upon exposure to high doses of radiation. Since the temperature during an experiment is kept constant, the increase must originate from radiation induced structural disorders. The relative B-factor was obtained by scaling with XSCALE.

- *Unit cell volume*: Upon exposure to high doses of radiation the unit cell volume of a crystal is known to increase. It was extracted from XDS for each dataset of a dose series.

Parameters from structure refinement with SHELX

- *R1 value from structure refinement*: Radiation damage alters the structure of a molecule and deteriorates the crystalline order. Therefore, the agreement between the model amplitudes and the measured amplitudes decreases and, thus, the R1 value increases with dose. The R1 value was extracted from the structure refinement of each dataset.

- *Bond length changes*: High resolution datasets allow precise determination of bond lengths. A bond length determined from X-ray diffraction is an average of the respective bond lengths of all molecules in the sample. Significant changes in this average bond length imply a change in the statistical distribution between two or more discrete states (e.g. single bond, double bond, bond cleavage, etc.) between the specific atoms. Bond length changes as function of dose could, in some cases, be observed as a consequence of radiation induced changes.

- *Thermal displacement parameters*: Hereafter called "TDP", the isotropic (ITDP) or anisotropic (ATDP) thermal displacement parameter is a measure of the extent to which the electron density of an atom is distributed. This usually describes the thermal movement of each atom around its centre of gravity.

  In case of radiation damage, an increase in TDPs can be observed as a result of radiation induced perturbations of the molecule. This increase can reflect displacements, disorders, or a change in occupancy, if a more pronounced increase of one specific TDP compared to the others is observed.

1.1.5 Dose calculation

In order to make a comparison of all measurements possible, the dose was taken as a common measure for radiation damage. The dose is defined as the absorbed energy [J] per mass [kg].

Dose calculation required knowledge of the beam size, beam shape, photon energy and the photon flux at the sample position as well as the crystal size and shape, the absorption coefficient of the sample and the exposure time.

Calculation of the dose D [J/kg] = D [Gy] was performed using

$$D = \frac{f_{inc} \cdot E \cdot 1.602 \cdot 10^{-19} \cdot [1 - exp(-\mu \cdot d)]}{\rho \cdot V} \cdot t \tag{1.1}$$

where f_{inc} [1/s] is the incident photon flux, which depends on the fraction of beam seen by the crystal, E [eV] is the photon energy in eV, μ [cm^{-1}] is the linear absorption coefficient, d [cm] is the average thickness of the crystal along beam direction, ρ [kg/m^3] is the density of the sample, V [m^3] is the volume of the sample and t [s] is the exposure time.

The linear absorption coefficients for all compounds at the respective energy were calculated using XOP.[102] The respective strategy for dose calculation depended on the beamline.

At PXI and PXIII, flux determination at the position of the sample was performed during measurements. The photon flux was permanently displayed on the graphical user interface at the beamlines. The Swiss Light Source is operated in top-up mode at a constant ring current of 400 mA, so no intensity decay of the beam had to be considered.

Dose calculation at beamline X13 was performed slightly different. Measurements were conducted in so-called “dose mode”. In dose mode a fixed dose setting is chosen for a measurement. Due to the intensity decay of DORIS III the crystal rotation speed is adjusted to the incident photon flux, so that each image is exposed to the same dose. With decaying photon flux the rotation is slowed down.

1.2 X-ray diffraction measurements

1.2.1 B12 cofactors

Sample preparation

B12 cofactors contain a cobalt(III) centre and are well known for their high susceptibility to photoreduction to cobalt(II).[23,106] The biological significance and characteristics of B12 cofactors have been discussed widely in the literature, although - interestingly - their biological function is still not fully understood.[50,53,54]

The X-ray radiation damage of two cofactors of B12, cyano- and methylcobalamin (see fig. 1.1), was investigated by single crystal X-ray diffraction experiments. Both cofactors were purchased in the highest available purity from Sigma Aldrich[*] and were used without further purification.

Single crystals were grown from an aqueous solution of the B12 cofactor, diluted in an iso-

---

[*] http://www.sigmaaldrich.com/germany.html

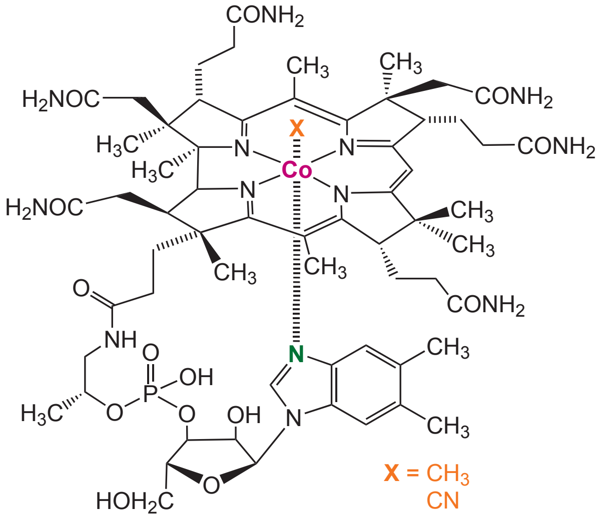

Figure 1.1: Structure of cyano- (X=CN) and methylcobalamin (X=CH_3)

propyl alcohol/water mixture. Crystals were obtained by vapour diffusion of this mixture against isopropyl alcohol. A more detailed description of the crystal growth procedure can be found in section A.4. Small rectangular crystals grew within a few days (see fig. 1.2).

Isopropyl alcohol was expected to be part of the crystal structure for both cofactors. In order to prevent any evaporation of the solvent from the crystals, all mounting procedures were performed at cryogenic temperatures. Therefore, the mother liquor containing the crystals was cooled by an open flow cold nitrogen gas stream. Crystals were then mounted in 0.1 - 0.2 μm and 0.2 - 0.3 μm nylon loops at this temperature. The mounted crystals were plunged in liquid nitrogen immediately after mounting and stored at cryogenic temperatures until the X-ray diffraction measurements were carried out.

Measurements were performed in two different beamtimes at the macromolecular crystallography beamline PXIII (X06DA) at the Swiss Light Source with a mar225 mosaic detector. Experiments were conducted at 100 K for both, cyano- and methylcobalamin. Additionally, cyanocobalamin was measured at 200 K.

Dose series of subsequent datasets consisting of 180 images measured with a rotation angle of $\Delta\varphi = 2^\circ$ were collected at an energy of 0.7537 Å (16.45 keV) until spot quality and resolution decreased significantly. The subsequent datasets showed a loss in data quality

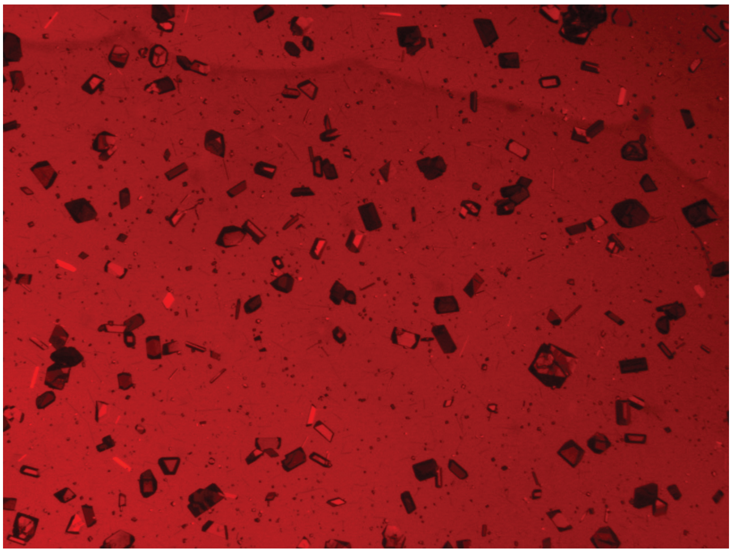

Figure 1.2: Photograph of cyanocobalamin crystals in an isopropyl/water-solution of cyanocobalamin powder.

upon long exposure to X-rays.

Cyanocobalamin

Dose series[37,47] of two cyanocobalamin crystals at 100 K and one cyanocobalamin crystal at 200 K were collected during the first beamtime.

Crystal CNCbl 1 was measured at 100 K and was 400 × 200 × 200 μm^3 in size. The exposure time during measurements was set to 1 s. Data acquisition was performed at a sample-to-detector distance of 70 mm. Filters were set to 15.6 % transmission of the beam, leading to a photon flux of 1.5×10^{10} ph/s, resulting in a dose of 0.98 kGy per image. 4860 images, yielding 27 complete datasets, were recorded. The obtained images showed small well-defined spots and no ice rings were visible, thus proving a good cryo handling of the samples. The data quality had visibly suffered after the full dose series. However, further processing showed that the crystal was not as severely damaged as expected.

As a consequence of this, crystal CNCbl 2 (400 × 400 × 300 μm^3) was measured without filters and exposed to the full intensity of the beam using the same parameters used for the first crystal. The photon flux was determined to be 9.8 × 10^{10} ph/s which lead to a dose of 2.62 kGy per image. The data was of excellent quality. After a few full rotations a significant loss in diffraction quality and resolution could be observed. Data collection was continued until a dose series of 4860 images had been obtained, resulting in 27 complete datasets.

Dose series at 200 K were performed on a crystal of 380 × 150 × 150 μm^3 in size (CNCbl 3). The determined photon flux was 10.8 × 10^{10} ph/s, resulting in a dose of 6.84 kGy per image. The exposure time of 1 s was kept, but the sample-to-detector distance was changed to 65 mm. After 3600 images, corresponding to 20 complete datasets, the data collection was stopped.

Methylcobalamin

Dose series of two methylcobalamin crystals were collected at 100 K in a second beam time. Both crystals absorbed a significantly higher dose than the crystals of cyanocobalamin. This higher dose on the samples was a result of the much higher incident photon flux during this beamtime and the smaller crystal size.

The first crystal (MeCbl 1, 150 × 60 × 80 μm^3) was measured at a sample-to-detector distance of 65 mm with an exposure time of 1 s. First, a complete dataset was collected with a filter transmission of 20 % to gather better low-resolution information. This collection was followed by a dose series of 4320 high resolution images, yielding 24 complete datasets, collected without filter. After the dose series was completed, a second data collection of 180 low-resolution images with a filter transmission of 20 % was conducted. The first low-resolution dataset was merged with the first (high-resolution) dataset of the dose series to obtain a well-fitting model for structure solution of the high resolution data. The incident photon flux without filter was 19.2 × 10^{10} ph/s, yielding in a dose of 33.61 kGy per image.

Crystal MeCbl 2 measured 250 × 50 × 40 μm^3 in size. All experimental parameters were kept the same as for MeCbl 1. The measured photon flux was 19.3×10^{10} ph/s, resulting in a dose of 38.0 kGy per image. 4500 images, resulting in 25 complete datasets, were collected.

Data evaluation

Owing to differences in photon flux and crystal size during the beamtimes as well as chemical composition of the samples, normalised mean intensity, bond length parameters and relative cell volumina had to be used for comparison. The dose delivered to the cyanocobalamin samples was significantly lower than that on the methylcobalamin crystals.

1.2.2 Amino acids and thymidine

Sample preparation

Crystals of L-serine, L-alanine and thymidine were all grown from a saturated aqueous solution. To obtain anhydrous crystalline samples, crystal growth was performed at temperatures above 40° C. Since the crystals were also needed for neutron diffraction, the main goal of the crystal growth was to obtain large crystals. Further information on the crystal growth is given in the appendix (section A.5).
In order to cause significant damage to the crystals, a high photon flux is required for X-ray diffraction measurements. At the same time overload of the detector has to be prevented. Hence, small crystals have to be used. Therefore, larger crystals of all three compounds were cut into small pieces for these measurements. The samples were then glued on graphite fibres which were attached to glas tips using two-component adhesive (see fig. 1.3). Afterward, the crystals were stored at room temperature. Since the crystals did not contain any solvent, no loss of crystal quality due to solvent evaporation during

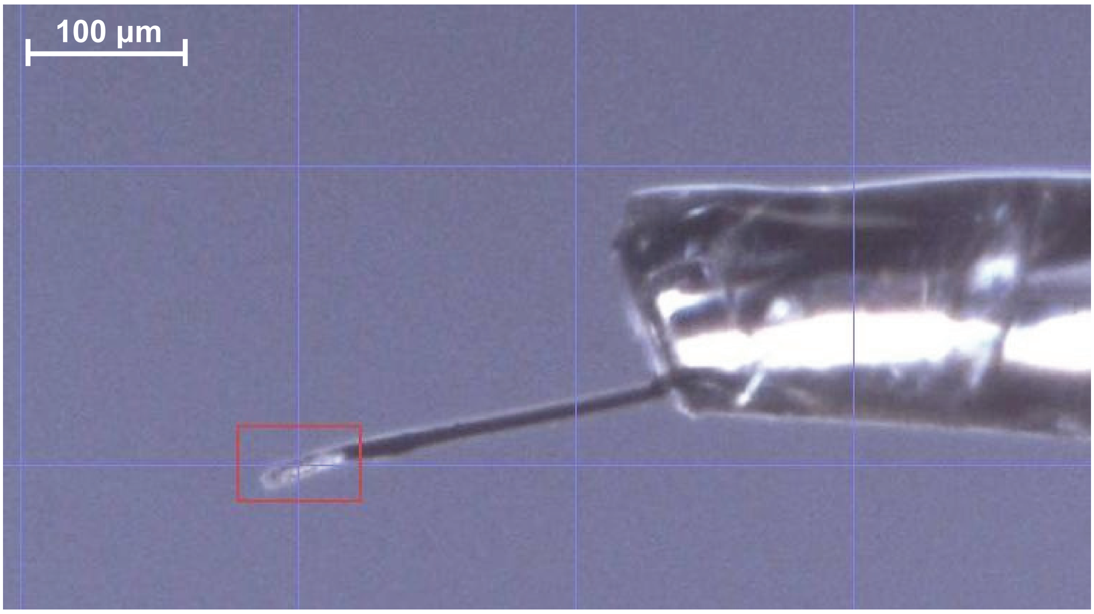

Figure 1.3: L-alanine crystal (within the red frame) attached to a graphite fibre. The picture was taken at beamline PXIII at the SLS.

storage and transfer was expected.

Measurements

Measurements on L-serine and thymidine were performed at the macromolecular crystallography beamline PXI at a wavelength of 0.7085 Å (17.5 keV). Measurements on L-alanine were conducted at beamline PXIII at 0.7560 Å (16.4 keV).

L-serine

X-ray diffraction images of L-serine (see fig. 1.4) were collected at beamline PXI at 90 K from a small single crystal ($120 \times 60 \times 20\ \mu\text{m}^3$) with a Pilatus 6M detector. The sample-to-detector distance was 185 mm. An oscillation range of $\Delta\varphi = 1°$ and an exposure time of 1 s per image were chosen. The beam size at the sample position was defocused to 80 $\times$ 150 μm^2 (h $\times$ v). The incident photon flux was 4.2×10^{10} ph/s which resulted in a

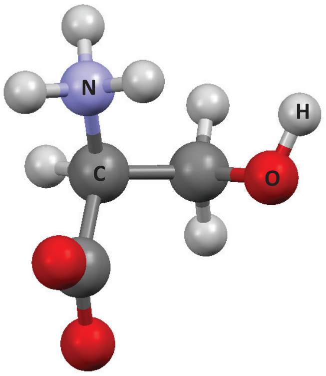

Figure 1.4: Molecular structure of anhydrous L-serine solved from X-ray data.

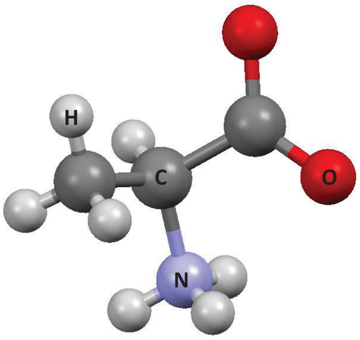

Figure 1.5: Molecular structure of L-alanine solved from X-ray data.

dose of 9.52 kGy per image. In total, 22680 images, yielding 63 complete datasets, were collected.

L-alanine

X-ray diffraction images of single crystals of L-alanine (fig. 1.5) were collected at beamline PXIII at 100 K with a mar225 mosaic detector from a small single crystal (60 × 20 × 10 μm^3) which was cut from a larger crystal. The oscillation range for each image was set to $\Delta\varphi = 2°$ with an exposure time of 1 s. During this experiment the sample-to-detector distance was set to 80 mm. The beamsize was 80 × 45 μm^2 (h × v) and therefore the

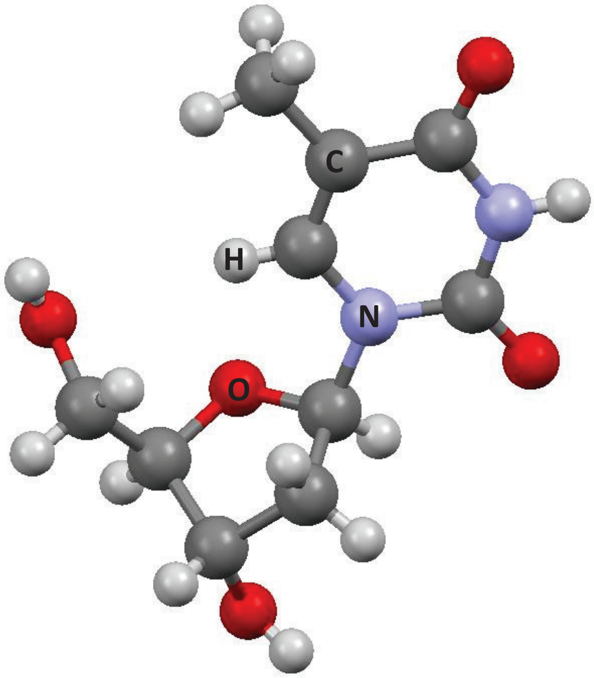

Figure 1.6: Molecular structure of thymidine solved from X-ray data.

crystal was fully irradiated. Measurements were conducted at an incident photon flux of 13×10^{10} ph/s, yielding a dose of 12.33 kGy per image. 4140 images, corresponding to 24 complete datasets, were collected.

Thymidine

For X-ray diffraction measurements a small single crystal ($70 \times 30 \times 20\ \mu\text{m}^3$) of thymidine was chosen. The mounting procedure was performed similarly to L-serine. The incident flux during measurements was 9×10^{10} ph/s with the filter set to 20 % transmission. The oscillation range was $\Delta\varphi = 1°$. The sample-to-detector distance was set to 165 mm and the exposure time was 0.5 s. The calculated dose per image was 5.10 kGy. The beam size in this case was similar to the L-serine measurements. In total 19080 images, resulting in 54 complete datasets, were collected.

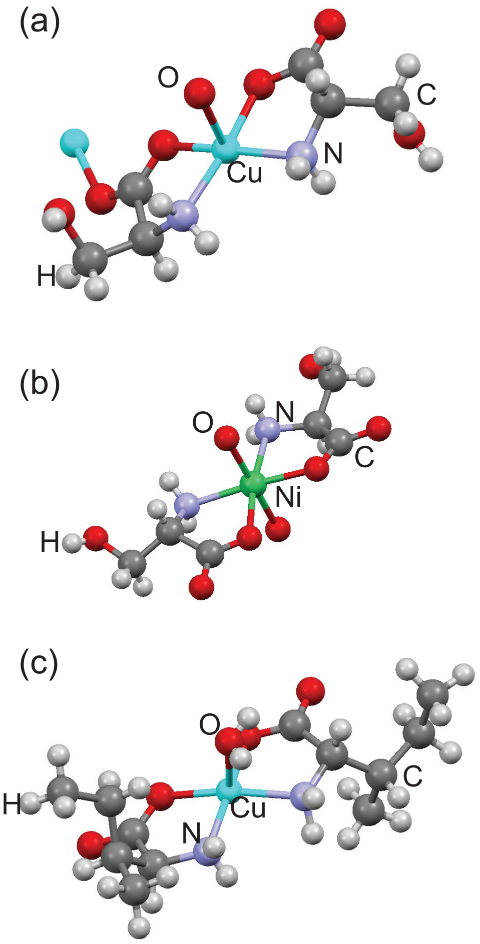

Figure 1.7: Molecular structures of CuSer (a), NiSer (b) and CuIso (c) as obtained from SHELX.

1.2.3 Metal amino acid complexes

Sample preparation

Single crystals of bis(L-serinato)copper(II) (CuSer)[103] (fig. 1.7 (a)), diaquobis(L-serinato)nickel(II)[104] (NiSer) (fig. 1.7 (b)) and bis(L-isoleucinato)copper(II)[105] (CuIso) (fig. 1.7 (c)) were directly mounted at the beamline in 0.1 - 0.2 μm nylon loops. The loops were supported with small amounts of glue at the end of the metal holder to prevent vibrations in the cryostream. The crystals were flash-cooled to 100 K directly after mounting.

Measurements

Measurements were conducted at the EMBL beamline X13 during two subsequent beamtimes. All crystals were measured at 100 K. Seven dose series of subsequent X-ray diffraction datasets of 180 images with rotation increments of 2° per image were collected.

In all cases the sample-to-detector distance was set to 40 mm. The beam size in all cases was slit down to 0.3×0.3 mm^2 (h × v). The NiSer crystals were of poor diffraction quality. CuSer and CuIso diffracted to 0.9 Å resolution. Each full dataset consisted of 180 images. Two to three dose series were collected per compound at different dose settings. Spot quality and resolution decreased significantly with increasing dose.

Data evaluation of all three compounds was performed as described in section 1.1.3 of this chapter. Due to the large beam divergence at X13, the crystal mosaicity could not be determined from the measurements. The mosaicity values obtained from XDS represent a convolution of the beam divergence and the crystal mosaicity. At X13 the refined mosaicity value is determined by the beam divergence, rendering any mosaicity measurements pointless.

CuSer

Three small blue single crystals of CuSer were selected for the measurements. Data collection was performed using different dose settings.

The first crystal (CuSer1) had a size of $250 \times 100 \times 20$ μm^3. The dose mode was set to 200 kHz, resulting in a dose of 6.6 kGy per image. 4860 images, yielding 27 complete datasets, were collected.

The second crystal (CuSer2) was similar in size to CuSer1. For CuSer2 the data collection was conducted in dose mode at 400 kHz per image. The resulting dose per image was 13.2 kGy. 1440 images, corresponding to 8 complete datasets, were collected.

The dimensions of the third crystal (CuSer3) were $250 \times 150 \times 30$ μm^3. The dose mode setting was 400 kHz, resulting in a dose per image of 12.8 kGy. 4140 images, resulting in 23 complete datasets, were collected.

NiSer

Measurements of NiSer were performed on two small light green crystals. Both crystals showed poor diffraction quality.

The first crystal (NiSer1) was 100 × 60 × 20 μm^3 in size. The dose mode setting for this crystal was 200 kHz, resulting in a dose of 4.5 kGy per image. A total of 4680 images, corresponding to 26 complete datasets, was collected from this crystal.

The dimensions of the second crystal (NiSer2) were similar to the first one. For NiSer2 the dose mode setting was 400 kHz, resulting in a dose of 9.0 kGy per image. 4860 images, yielding 27 complete datasets, were collected.

In case of NiSer1 data processing as well as structure refinement were performed. The data of the second crystal could be processed, but no structure refinement could be performed due to the poor data quality. The mean intensity values as well as the correlation coefficient for both NiSer complexes showed strong deviation between each other. Only the normalised unit cell volume and relative B-factor were taken to follow the X-ray damage process for all metal amino acid complexes.

CuIso

Two small blue single crystals of CuIso were selected for the measurements. Two different dose mode settings were chosen for the data collection.

The first crystal (CuIso1) was 120 × 150 × 10 μm^3 in size. This crystal was measured at a dose mode setting of 100 kHz, which resulted in a dose of 6.2 kGy per image. 4860 images, corresponding to 27 complete datasets, were collected.

The second crystal (CuIso2) was 150 × 150 × 10 μm^3 in size. The dose mode was set to 400 kHz, resulting in a dose of 24.9 kGy per image. A total of 1800 images, resulting in 10 complete datasets, were collected.

2 X-ray absorption measurements

In the following chapter the experimental procedure for X-ray Absorption Near Edge Spectroscopy (XANES) measurements is described. The main goal of these measurements was to investigate X-ray induced photoreduction, which can be directly probed by a shift in the absorption edge in a XANES spectrum. The influence of the factors temperature, solvent and chemical composition was investigated.

2.1 X-ray absorption experiment strategy

2.1.1 Beamline: SuperXAS (X10DA) - Swiss Light Source

The SuperXAS beamline is a super-bending magnet beamline for X-ray Absorption Spectroscopy. It is equipped with a Si(111) double crystal monochromator followed by a toroidal mirror for higher harmonic suppression and focusing. The beam size at the sample was determined to be 0.08×0.11 mm^2 (h × v). The photon flux on the sample is approximately 1×10^{12} ph/s for a ring current of 400 mA.

The beamline is equipped with two 30 cm long ion chambers in front of and behind the sample filled with a He/N$_2$ mixture for transmission measurements. For fluorescence measurements, a 13 element LN$_2$ cooled solid state Germanium detector is available.

2.1.2 XANES data collection

In transmission geometry, XANES spectra were collected by changing the incident energy over a defined range and measuring the incident intensity as well as transmitted intensity behind the sample as function of energy. In fluorescence geometry, the fluorescence from the sample is measured as a second variable. These measurements are conducted at defined energy steps.

Spectra collected for cyanocobalamin and the four iron compounds were measured in three regimes. For each regime, different energy steps were chosen.

In the pre-edge region energy steps of 2 eV were used. Since the most important feature of the XANES measurements is the horizontal shift of the absorption edge and a change in the white line, measurements were conducted at smaller energy steps in this part of the spectrum. Acquisition of data points was performed in 0.5 eV steps around the edge region. Above the absorption edge, energy steps of 1 eV were used.

The acquisition of a spectrum deposits a defined dose of radiation in the sample. With each spectrum that is collected, the dose to the sample increases. Therefore, subsequent spectra can be used to monitor radiation induced changes in the sample. This series of adjacent spectra will be called *dose series* in agreement with the nomenclature applied in the X-ray diffraction measurements. In case of the iron compounds, additional exposure times at an energy of 7280 eV were added after the collection of each spectrum.

2.1.3 Data evaluation

Normalisation of all spectra was performed using the IFFEFFIT package.[107] The pre-edge region was fitted by a linear background function and the post-edge region was fitted by a spline function. Normalisation was performed so that the inflection point of the first oscillation above the absorption edge was assigned to a $x\mu_{norm}$ of 1 for all spectra of all compounds[*].

---

[*] This method was proposed in the Athena User's Guide which can be found at http://cars9.uchicago.edu/ ravel/software/doc/Athena/mobile/index.html.

For comparison of the different compounds it was necessary that all spectra were normalised in the same way. In all cases, where a change in the spectra could be observed, these changes mainly manifested themselves in the absorption edge position and the intensity of the white line.

The energy value of the edge position where $x\mu_{norm}$, the normalised absorption coefficient, reached 0.5 was named E_0. This value was used for investigation of the edge shift and, thus, as an indicator of photoreduction. This method was first proposed by Champloy *et al.*[23] A Perl script was used to extract the values of E_0 for the subsequent spectra. E_0 was then plotted as function of dose. The position of E_0 represents the distribution between the two discrete states of the cobalt centre (Co(III) and Co(II)). In the beginning all cobalt centres within the sample are Co(III). This amount decreases with dose, finally leading to an equilibrium between the unreduced (Co(III)) and the reduced (Co(II)) state. Therefore, E_0 should reach a threshold at higher doses.

2.1.4 Dose calculation

The dose was determined in an automated process. Summation of the absorbed energies at every photon energy was performed using a Perl script. The theoretical X-ray absorption coefficients of the sample, the incident photon flux at the respective energy, the exposure time, sample thickness and mass, as well as the beam size were taken into account. Additionally, fluorescence escape and self-absorption of the X-ray fluorescence photons were included into the calculations.

The applied doses per spectrum for cyanocobalamin were 0.39 MGy, while for the iron compounds the doses per spectrum varied between 0.03 and 0.06 MGy, depending on the photon flux at the beamline and the different absorption coefficients determined for the compounds.

2.2 X-ray absorption measurements

Cyanocobalamin (fig. 2.1 (a)), potassium hexacyanoferrate (fig. 2.1 (b)), ammonium ferric citrate (fig. 2.1 (c)) and pyrite (fig. 2.1 (e)) were obtained from Sigma Aldrich. The organic iron sulphur cluster (μ-propyldithiolate diiron carbonylaminepropyl, fig. 2.1, in this work referred to as diiron-dithiolate (d)) was kindly provided by Dr. Ott from Stockholm university.[109]

XANES measurements of all compounds were performed during four beamtimes at the SuperXAS beamline (X10DA) at the Swiss Light Source, Villigen, Switzerland.

2.2.1 Sample preparation

Solid samples of cyanocobalamin, ammonium ferric citrate, potassium hexacyanoferrate, diiron-dithiolate and pyrite were measured in transmission geometry in boron nitride pellets. Boron nitride was used to obtain samples of sufficient thickness, so they would not break during the preparation and cooling process.

The compounds were pestled with boron nitride in a fixed ratio (see table 2.1 for details on the composition) until a homogeneous distribution was reached. The mixtures were then pressed into pellets of a thickness of 0.2 mm, cut into small pieces in dimensions of about 0.3×1 mm^2 and glued onto a sample holder.

For measurements in aqueous solution, cyanocobalamin was dissolved in water (see table 2.1 for concentration) and filled into quartz capillaries with a diameter of 1 mm and a wall thickness of 0.01 mm. The samples were measured in fluorescence geometry.

Ammonium ferric citrate was dissolved in water (see table 2.1 for concentration) and placed in a wet cell which consisted of a metal plate of 0.2 mm with a 1 mm drill hole containing the solution. The wet cell was then sealed with Kapton foil on both sides (see fig. 2.2). The samples were measured in transmission geometry.

Solid samples were measured at temperatures between 5 and 300 K for cyanocobalamin and between 100 and 300 K for the iron compounds. Aqueous solutions were measured at temperatures between 100 K and 250 K. This way they were kept in a solid state, thereby

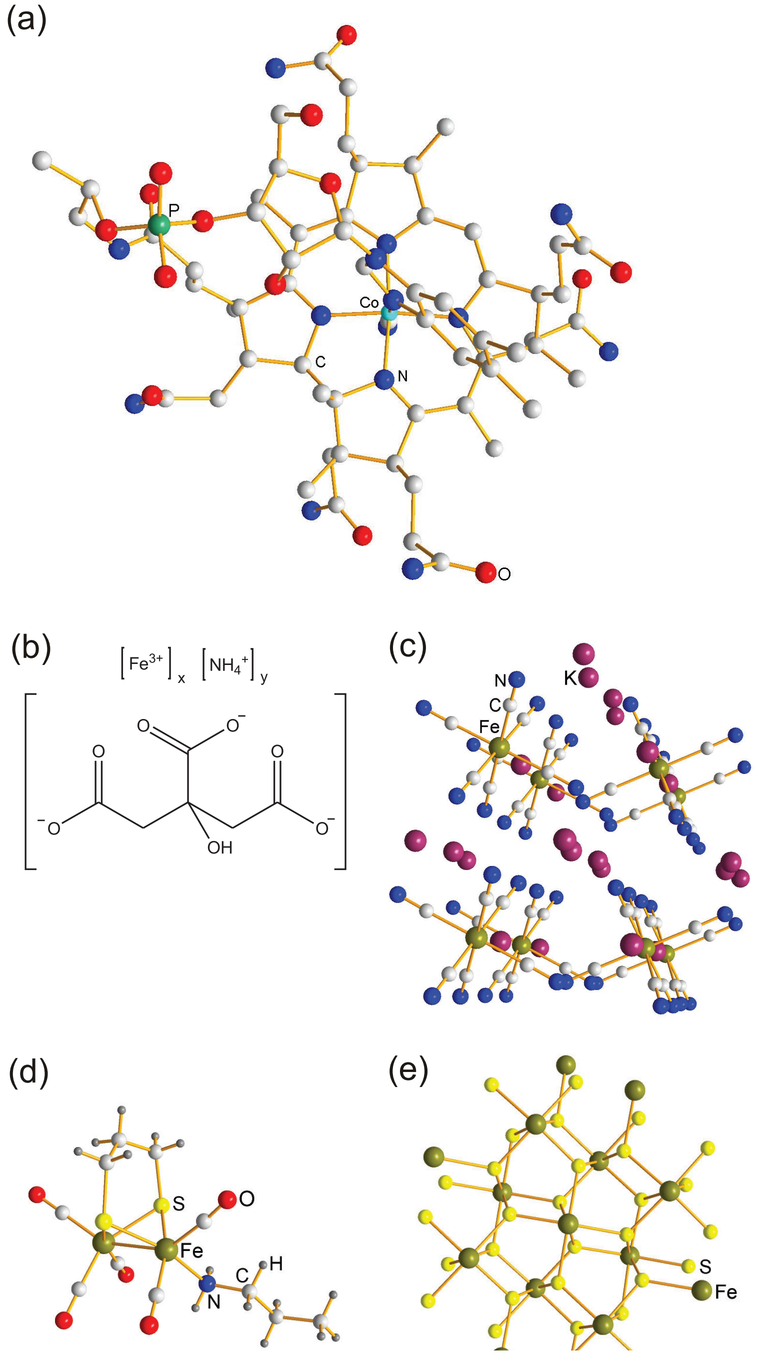

Figure 2.1: Compounds measured using XANES: Cyanocobalamin (a), ammonium ferric citrate (b), potassium hexacyanoferrate[108] (c), diiron-dithiolate[109] (d) and pyrite[110] (e).

inhibiting convection, which would cause diffusion of unirradiated material in the beam. Temperatures between 100 K and 300 K were realised using an open flow nitrogen cryostat. Temperatures below 100 K down to 5 K were achieved by a helium cryostat.

Table 2.1: Molecular formula, molecular weight and amount of the measured compounds. The overall molecular formula is obtained by determination of the ratio between the amount of the compound and the boron nitride/water.

Compound	**Molecular formula of compound**	**Molecular weight [g/mol]**	**Amount [mg]**	**Boron Nitride (24.83 g/mol) [mg]**	**Water (18.015 g/mol) [ml]**	**Overall molecular formula**
Solid cyanocobalamin	$CoC_{63}H_{88}N_{14}O_{14}P$	1355.39	94.30	106.0	-	$CoC_{63}H_{88}B_{61}N_{75}O_{14}P$
Aqueous cyanocobalamin	$CoC_{63}H_{88}N_{14}O_{14}P$	1355.39	61.50	-	200.0	$CoC_{63}H_{333}N_{14}O_{259}P$
Solid ammonium ferric citrate	$FeC_6H_5NO_7$	252.00	50.00	200.0	-	$FeC_6H_5B_{42}N_{43}O_7$
Aqueous ammonium ferric citrate	$FeC_6H_5NO_7$	252.00	105.00	-	0.3	$FeC_6H_{87}NO_{48}$
Potassium hexacyanoferrate	$K_3[Fe(CN)_6]$	329.22	50.00	350.0	-	$K_3[FeC_6B_{93}N_{99}]$
Diiron-dithiolate	$Fe_2C_{11}H_{15}NO_5S_2$	417.07	19.05	106.0	-	$Fe_2C_{11}H_{15}B_{94}N_{95}O_5S_2$
Pyrite	FeS_2	119.99	15.20	184.8	-	$FeS_2B_{59}N_{59}$

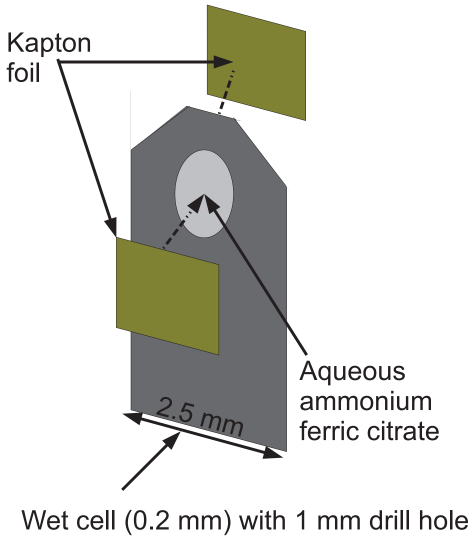

Figure 2.2: Illustration of the wet cell for XANES measurements of the aqueous ammonium ferric citrate solution.

2.2.2 Cyanocobalamin

For cyanocobalamin dose series of adjacent spectra were recorded using the full intensity of the X-ray beam. The samples were exposed to high doses of radiation during this procedure, so no further exposure time was needed after each spectrum. This led to equidistant steps in terms of dose, meaning that each dataset absorbed the same amount of dose.

Spectra of cyanocobalamin were collected for energies ranging from 7680 eV to 7890 eV. The pre-edge region ranged from 7680 eV to 7705 eV, the edge region of the spectra was ranging from 7705 eV to 7740 eV. Above 7740 eV up to 7890 eV the first few EXAFS oscillations were measured.

Measurements of the solid and aqueous compounds at temperatures between 100 K and 300 K in steps of 50 K were performed during the first beamtime.

During a second beamtime the photoreduction process of solid cyanocobalamin at temperatures of 5 K, 25 K, 50 K, 75 K and 100 K was investigated. The spectra appeared to be very noisy, most probably due to perturbations of the helium cryostream which lead to a movement of the sample within the beam and thus prevented a homogeneous irradiation. Therefore, extraction of the absorption edge position required a slightly different procedure than performed for samples cooled with nitrogen: The spectra were normalised as described above. Since the absorption edge was noisy, the E_0 position could not be directly derived as it was not only influenced by a possible shift, but mainly by the error of the obtained data. Although a direct extraction of the value E_0 would have been preferred, it was necessary to fit the absorption edge and first white line by a Gaussian function. This way it was possible to find a "corrected absorption edge position". E_0 was therefore extracted from the Gaussian fit instead of the noisy absorption edge itself in order to erase the error occuring due to the quality of the data.

2.2.3 Iron compounds

Series of adjacent spectra of all iron compounds were recorded by collecting spectra with a beam attenuated to 8% of the full photon flux. For beam attenuation a filter wheel equipped with boron nitride pellets of different thicknesses was placed in front of the first ion chamber. Each spectrum was followed by an exposure to the unattenuated beam at 7300 eV. Then a second XANES spectrum was taken, again followed by an exposure to the unattenuated beam and so on. The exposure time (t) after each spectrum (n) was increased exponentially according to the formula t [s] = $2 + 2^n$.

Radiation damage follows an exponential decay law. Therefore, it was necessary to obtain a large amount of data at lower doses to gather detailed information about the damage process. Plotting of the extracted parameters as function of dose lead to an exponential increase of the step-size between data points in terms of dose.

XANES spectra of all iron compounds were collected for energies from 7080 eV to 7300 eV. The pre-edge region was defined as the region from 7080 eV to 7105 eV. The edge region ranged from 7105 eV to 7150 eV and above this, the first oscillations of the EXAFS region followed.

Spectra of the solid samples were collected from all four compounds at temperatures of

100 K and 300 K. Ammonium ferric citrate was the only compound also measured in solution. In this case measurements were performed at 100 K and 200 K.

3 Neutron diffraction measurements

In this chapter, the experimental procedures for combined X-ray irradiation and neutron diffraction measurements on the two amino acids L-serine and L-alanine, as well as the nucleoside thymidine are explained. The goal of these measurements was to directly observe X-ray induced hydrogen abstraction and gain an understanding of the global damage processes of these compounds.

3.1 Neutron diffraction experimental strategy

Single crystal neutron diffraction data were collected from previously X-ray irradiated crystals and non-irradiated crystals of a control group, in order to investigate different states of X-ray damage.

3.1.1 Beamlines

F4 - DORIS III

X-ray irradiation of the crystals was conducted at the HASYLAB beamline F4. F4 is a bending magnet beamline at DORIS III, located 8 m from the source. It is a white X-ray beamline with a critical energy of 16 keV. The maximum beam size is 15 × 8 mm^2 (h × v).

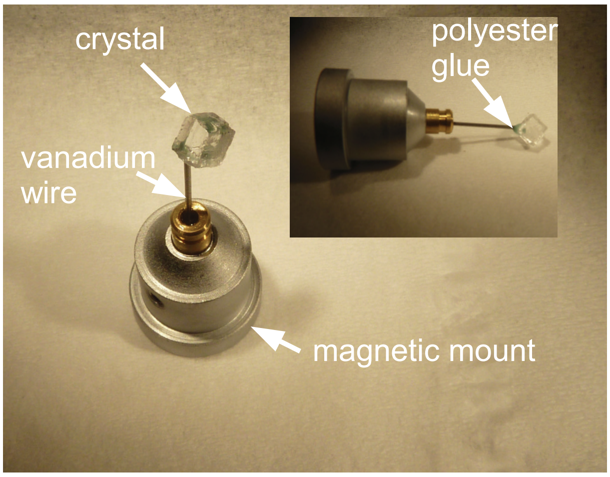

Figure 3.1: A crystal for neutron measurements mounted onto vanadium wire using polyester glue.

SXD - ISIS

Neutron measurements were conducted at the SXD-beamline at the ISIS neutron source. Beamline SXD is dedicated to single crystal neutron diffraction. It is equipped with a water moderator. The wavelengths at this beamline range from 0.2 to 10 Å. The beamsize at the sample position is about 15 mm.

The beamline provides eleven position sensitive detectors. The detectors are optically encoded ZnS scintillators, each with an active area of 192 × 192 mm^2 and 64 × 64 pixels. The resolution of the detectors is 3 × 3 mm^2.

Temperatures during measurements can be selected by using a closed cycle liquid helium cryostat which provides a temperature range from 1.5 K to 300 K.

3.1.2 Sample preparation

For the neutron diffraction measurements crystals were cut to pieces of the same size. L-serine and L-alanine crystals were cut using a Well 6234 wire saw equipped with a 0.5 mm thin diamond wire, which was immersed in water prior to cutting. Thymidine was cut into pieces of the same size using a scalpel.

The crystals were then glued onto a vanadium wire using a polyester-based two-

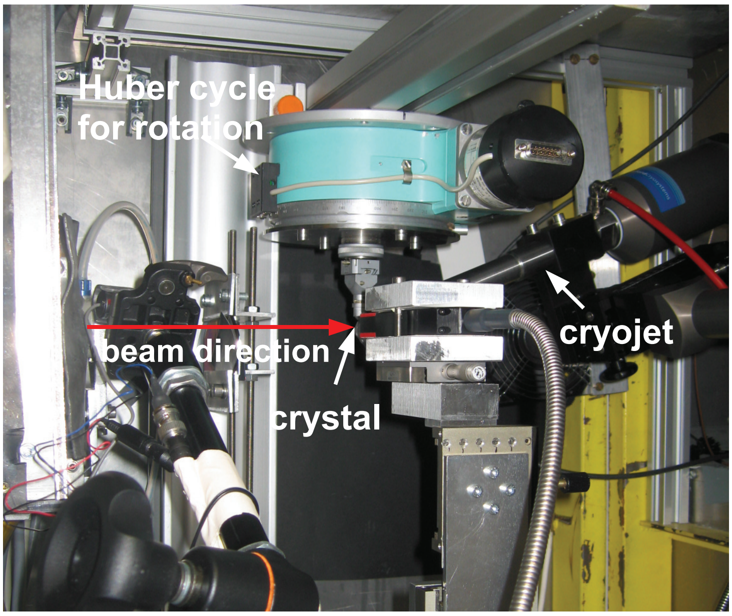

Figure 3.2: Experimental setup for X-ray irradiation.

component adhesive (fig. 3.1). The scattering length of neutrons for vanadium is close to zero,[111] so vanadium is almost transparent for neutrons. The chosen adhesive contains only few hydrogen atoms, so it did not contribute significantly to the neutron diffraction measurements and only added slightly to the background.[89]

3.1.3 X-ray irradiation

X-ray irradiation was performed beforehand at the HASYLAB white beam beamline F4 at DORIS III in Hamburg. For irradiation, the maximum beam size was used. This way, it was possible to expose the entire crystal volume to the X-ray beam. For irradiation crystals were mounted on a single axis goniostat and cooled to 100 K by an open flow nitrogen jet (fig. 3.2). Crystals were then centered into the beam and slowly rotated during X-ray exposure. The low energy X-ray spectrum of the incident photon flux was filtered out by a 500 μm silicon filter, that was positioned in front of the sample. This way, a more homogeneous dose deposition in the crystals was obtained. Since all crystals were of the same size and irradiation was performed with hard X-rays, the absorption was assumed to be similar for all crystals of one compound. Intensity changes due to the decay of the DORIS III ring current were taken into account and normalisation of the exposure time was performed for data evaluation.

After each X-ray irradiation crystals were unmounted and stored at liquid nitrogen temperatures until the neutron diffraction measurements.

3.1.4 Neutron data collection

Crystals were transferred to vanadium canes at liquid nitrogen temperatures. The canes containing the previously X-ray irradiated crystals were then transferred into the SXD cryostat whilst keeping them at liquid nitrogen temperatures. For the measurements the crystals were then further cooled to 5 K. Measurements took between 8 to 48 hours, depending on the damage level of the crystal.

3.1.5 Data evaluation and structure refinement

Data evaluation was conducted directly during measurements using an IDL-based analysis software.[91] For structure refinement SHELX[101] was used.

Determination of a possible hydrogen abstraction was performed by a refinement consisting of three steps. This refinement aimed at the investigation of the isotropic thermal displacement parameters which, as mentioned in section 4.1.1 in ***"Principles"***, represent a combination of the thermal displacement of an atom, the atomic displacement at specific sites by radiation damage and the general, global disorder generated by long exposures to X-ray irradiation.

As a first refinement step the occupancy as well as the anisotropic displacement factors of the heavy atoms and the hydrogen atoms were refined freely for the undamaged and slightly damaged crystals. The free refinement gave no significant occupancy decrease for the heavy atoms, but in case of damaged crystals an occupancy decrease for specific hydrogen atoms could be found.

In a second refinement step the occupancy of all atoms (including the hydrogens) was kept at 1.0 and the isotropic thermal displacement parameters (hereafter simply called "ITDPs", similar to X-ray data collection) were freely refined. The refinement was performed isotropically since no anisotropic refinement was possible for the more damaged crystals.

The third refinement step differed slightly for each compound and will be explained in the following sections.

L-serine

In the case of the X-ray irradiated crystals of L-serine free refinement of the occupancies as well as the ITDPs of all atoms showed an increase in ITDP and a decrease in occupancy for two specific hydrogen atoms (H5 and H6). In the second (isotropic) refinement step the occupancy of all atoms was kept at 1.0. A general increase in ITDPs as function of dose could be observed. However, the ITDPs of the two hydrogen atoms H5 and H6 showed a more pronounced increase.

In order to distinguish an increase in ITDP due to global damage of the crystal from an increase in ITDP due to a specific change in the position of a certain atom, the following procedure was applied: The strong increase in all ITDPs required the assignment of a common ITDP to all hydrogen atoms connected to the same heavy atom. By this, it is implied that all hydrogen atoms bound to a certain heavy atom are chemically equal.

Additionally, the relation of the hydrogen ITDPs to the respective heavy atom ITDP was determined. In case of the hydroxyl group (OH group), the ITDP increase was set in relation to the increase of the ITDPs of the methylene group (CH_2 group) (see fig. 1.4). All relations were kept constant during structure refinements for all X-ray irradiated crystals of L-serine. The occupancy of all hydrogen atoms was then refined freely, while the ITDP was kept fixed to a value calculated from the relation between the heavy and the corresponding hydrogen atom.

L-alanine and thymidine

In case of L-alanine, no global nor specific increase in ITDPs or decrease in occupancy could be observed in the first refinement step even at higher irradiation times. In the case of thymidine, an increase in a specific hydrogen ITDP could be observed in the first refinement step. The second refinement step confirmed the observations for both compounds. L-alanine did not show any pronounced increase in ITDPs and thymidine only showed an increase of the ITDP of hydrogen atom H7.

Since no significant global increase of the ITDPs was observed, even at long X-ray irradiation times, it was not necessary to find a relation between the hydrogen ITDPs and their heavy atoms. Therefore, a common ITDP was assigned to all hydrogen atoms connected to the same heavy atom in the third refinement step. This common ITDP was the mean value of the freely refined ITDPs obtained from the second refinement step. The occupancy of all hydrogen atoms was then refined freely in this final step.

3.2 Neutron diffraction measurements

Neutron diffraction measurements of crystals of L-serine, L-alanine and thymidine were performed at the ISIS SXD-beamline at the Rutherford Appleton Laboratory in England. Crystals were prepared as described in section 3.1.2 of this chapter. The exact crystal size and respective irradiation times are given in this section.

3.2.1 L-serine

L-serine crystals (fig. 3.3 (a)) were cut to cubes of $3 \times 3 \times 3$ mm^3 in size and were X-ray irradiated for 375, 600 and 1680 seconds. Additionally, unirradiated crystals were

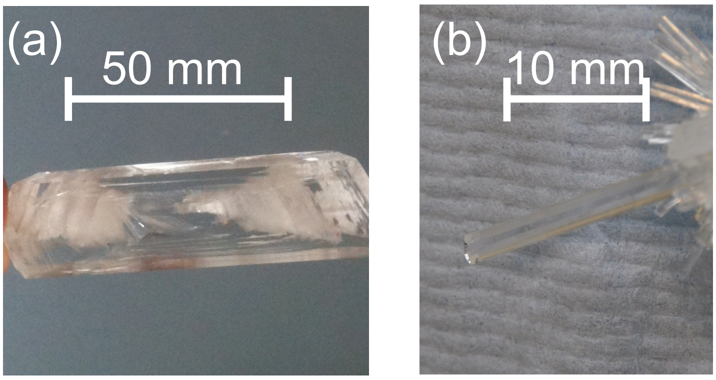

Figure 3.3: L-serine crystal (a) and thymidine crystals (b) grown from a saturated aqueous solution. The crystals were cut into small cubes of equal size for neutron diffraction measurements.

prepared as a control group.

3.2.2 L-alanine

The L-alanine crystals were slightly smaller than the L-serine crystals and were cut to cubes of $2 \times 2 \times 2\ \mathrm{mm}^3$ in size. X-ray irradiation was performed for 600 and 3600 seconds. No unirradiated crystal was investigated.

3.2.3 Thymidine

Thymidine crystals (fig. 3.3 (b)) were obtained as long needles and were cut to pieces of $2 \times 2 \times 1\ \mathrm{mm}^3$ in size. The crystals were X-ray irradiated for 600 and 1200 seconds. An unirradiated crystal was also measured.

IV Results

1 X-ray diffraction measurements

1.1 B12 cofactors

X-ray induced photoreduction of the two vitamin B12 cofactors cyanocobalamin and methylcobalamin was investigated at 100 K using X-ray diffraction. Additional diffraction measurements of cyanocobalamin at 200 K revealed a temperature-dependent behaviour. Furthermore, differences as well as similarities of the radiation damage process to cyanocobalamin and methylcobalamin could be found.

Detailed information on experimental details and crystallographic data for all crystals can be found in the appendix in section A.4. Fig. 1.1 shows the behaviour of different radiation parameters as function of dose for the two cyanocobalamin crystals (marked bright and dark red) and for the two methylcobalamin crystals (marked dark and light blue). The behaviour of these parameters for samples of the same compound with dose agrees well.

Fig. 1.1 (a) shows the absolute mean intensity for all four crystals. The starting value of the mean intensity of CNCbl 2 is much higher compared to the other crystals and decreases strongly with dose. Since the mean intensity depends on the diffraction properties on the crystal and the flux, normalised values had to be used for comparison. All normalised values used were obtained as described in section 1.1.4 in chapter 1 in ***"Experimental"***.

Fig. 1.1 (b) shows the normalised mean intensity for both cyanocobalamin (bright and dark red) and both methylcobalamin (dark and light blue) crystals.

Linear fitting (not shown) of the normalised mean intensity was performed for the two dose series of cyanocobalamin and the two dose series of methylcobalamin up to 34 MGy.

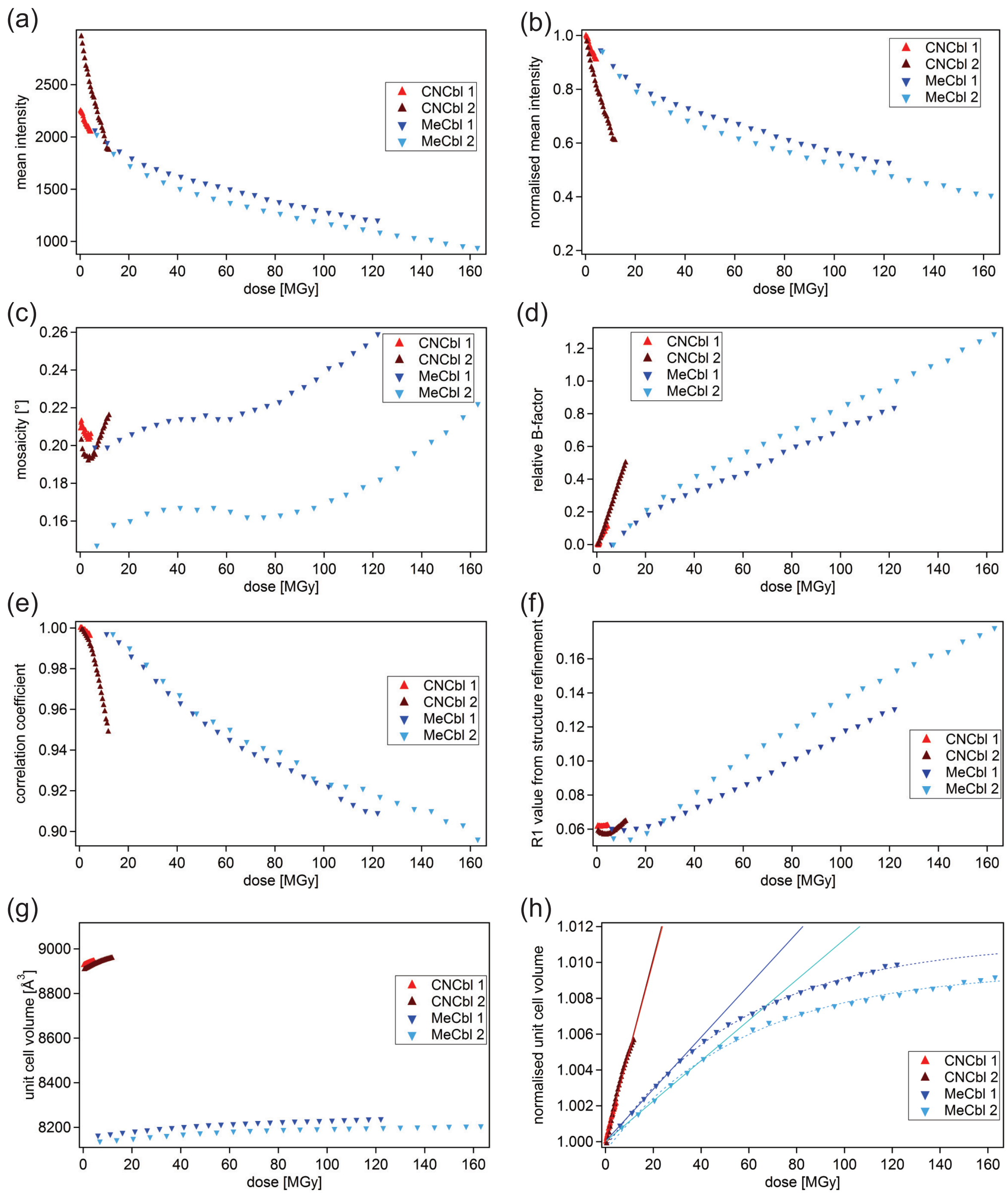

Figure 1.1: Absolute (a) and normalised (b) mean intensity, mosaicity (c), relative B-factor (d), correlation coefficient (e), R1 value from structure refinement (f), absolute (g) and normalised unit cell volume (h) of both cyanocobalamin crystals (red) and both methylcobalamin crystals (blue) measured at an energy of 16.45 keV and a temperature of 100 K as function of dose.

Comparison of the slopes reveals a three- to fourfold reduction of the mean intensity decay with dose for methylcobalamin with respect to cyanocobalamin.

Fig. 1.1 (c) shows the mosaicity changes as function of dose. In case of cyanocobalamin the mosaicity first slightly decreases from 0.20° to 0.19°, but then increases again with dose to 0.22°. Mosaicity values of the two methylcobalamin crystals show a similar behaviour to each other. The mosaicity value of MeCbl 1 starts at 0.20° and increases slightly to 0.22°. Above 20 MGy, it stays constant up to 60 MGy, where it continues to increase to 0.26° at the maximum dose of 120 MGy. MeCbl 2 starts at 0.14° and increases slightly to 0.16 at 20 MGy. Between 20 MGy and 80 MGy the mosaicity stays constant. Above 80 MGy, it continuously increases to 0.22° for 160 MGy.

The increase of the relative B-factor, obtained from scaling with XSCALE, with dose (fig. 1.1 (d)) reveals a fourfold higher radiation susceptibility of cyanocobalamin. For cyanocobalamin the B-factor increases from 0.0 to 0.5 after only 15 MGy of dose whereas for methylcobalamin a value of 0.5 is reached at 60 MGy. At a maximum dose of 160 MGy the relative B-factor of methylcobalamin reaches 1.3.

The correlation coefficients of the first to the subsequent datasets (fig. 1.1 (e)) of all four crystals show a behaviour similar to that of the normalised mean intensity: Both samples of the same compound show a similar decrease in correlation with dose. Cyanocobalamin shows a faster decrease with dose compared to methylcobalamin. In case of cyanocobalamin the correlation coefficient decreases from 1 to 0.945 after a dose of 18 MGy whereas for methylcobalamin a similar reduction occurs at a dose of 62 MGy.

The range of the R1 value from structure refinement with increasing X-ray dose is shown in fig. 1.1 (f). The R1 value starts at around 0.06 for all four samples. This value agrees well with literature data.[112] The R1 value for both cyanocobalamin crystals stays constant up to 8 MGy, at which the R1 value of the second crystal starts to increase linearly. The first cyanocobalamin crystal was not measured to this dose. Both R1 values for methylcobalamin first remain relatively constant up to a dose of around 20 MGy. At higher doses, the R1 value increases with dose in a more or less linear fashion.

Fig. 1.1 (g) shows the change of the absolute unit cell volume of all four crystals. The cell volumina for methylcobalamin are much smaller than for cyanocobalamin. Therefore, normalised values were used once again. Fig. 1.1 (h) shows the normalised unit cell volume increase as function of dose. In case of methylcobalamin the observed increase can be fitted by an exponential function. However, for comparison of both B12 cofactors a linear fit was applied for cyano- and methylcobalamin, respectively. Methylcobalamin was fitted linearly to a dose of 34 MGy. Fitting reveals a four- to fivefold stronger unit cell volume increase for cyanocobalamin (a slope of 0.00050, respective 0.00051 for cyanocobalamin, 0.00015, respective 0.00011 for methylcobalamin). The strong difference between both cyanocobalamin crystals observed for the decay of the normalised mean intensity could not be detected here. The normalised unit cell volume of methylcobalamin seems to reach a threshold at 1.012. In other words: The cell volume seems to increase by around 1.2% compared to the initial unit cell volume and seems to remain constant afterwards. However, this observation still has to be verified.

The R1 values from structure refinement of all four measurements were relatively small, which allows the analysis of bond length changes. Bond elongations between the upper (Co-C-bond) and lower (Co-N-bond) axial ligand (see fig. 1.1) of the cobalt centre have been of wide interest in investigations of the enzymatic mechanisms of B12 cofactors.[113–115] Therefore, it is essential to exclude that this effect is a result of radiation damage. Fig. 1.2 (a) and (c) show the absolute Co-C- and Co-N-bond length values for all four crystals. Bond length changes were investigated using normalised values which can be found in fig. 1.2 (b) for the Co-C- and fig. 1.2 (d) for the Co-N-bond, respectively. Both bond length changes were fitted by an exponential function in case of methylcobalamin. For the normalised Co-C-bond a plateau is reached at a value of 1.045 and 1.065, respectively. The normalised Co-N-bond also reaches a plateau at higher doses, in this case at 1.060. Similar to the normalised unit cell volume a linear fit was also applied for both bond length changes in order to compare the changes for both B12 cofactors. Both dose series of methylcobalamin were fitted linearly to a dose of 34 MGy. Both normalised bond lengths show a twofold linear increase for cyanocobalamin compared to methylcobalamin.

Fig. 1.3 (a) shows the normalised a-axis lengths as function of dose for both, cyanocobal-

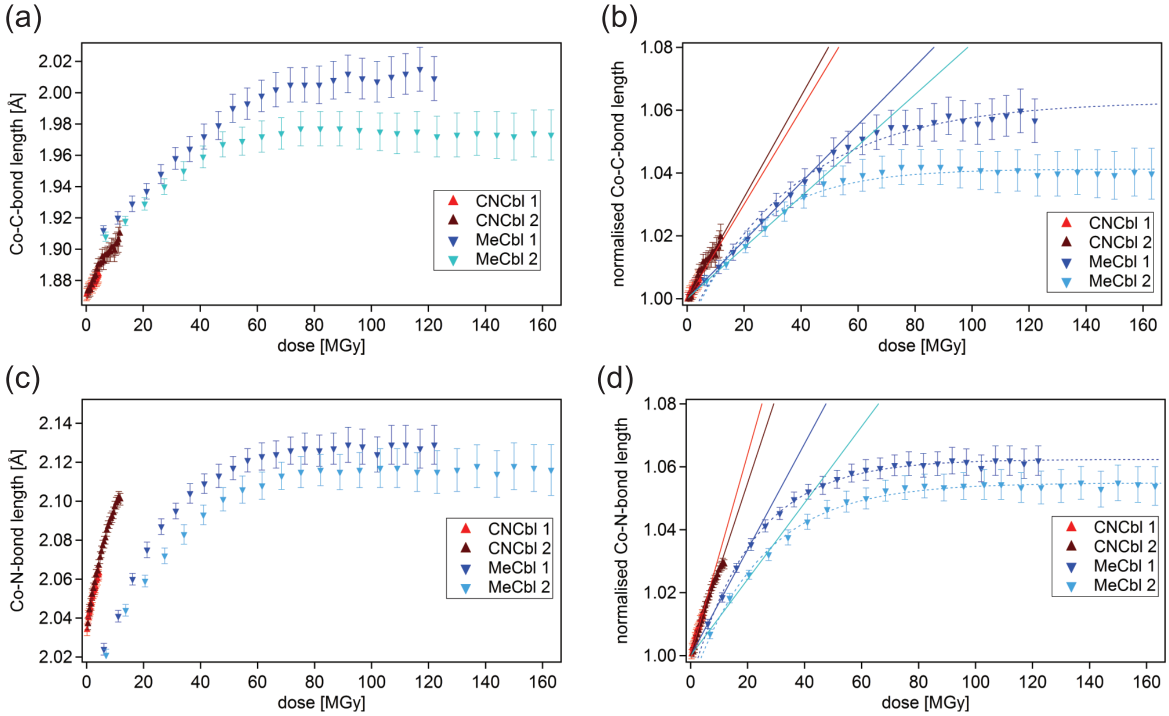

Figure 1.2: Co-C-bond length (a), normalised Co-C-bond length (b), Co-N-bond length (c) and normalised Co-N-bond length (d) for both cyanocobalamin crystals (red) and both methylcobalamin crystals (blue) at 100 K as function of dose.

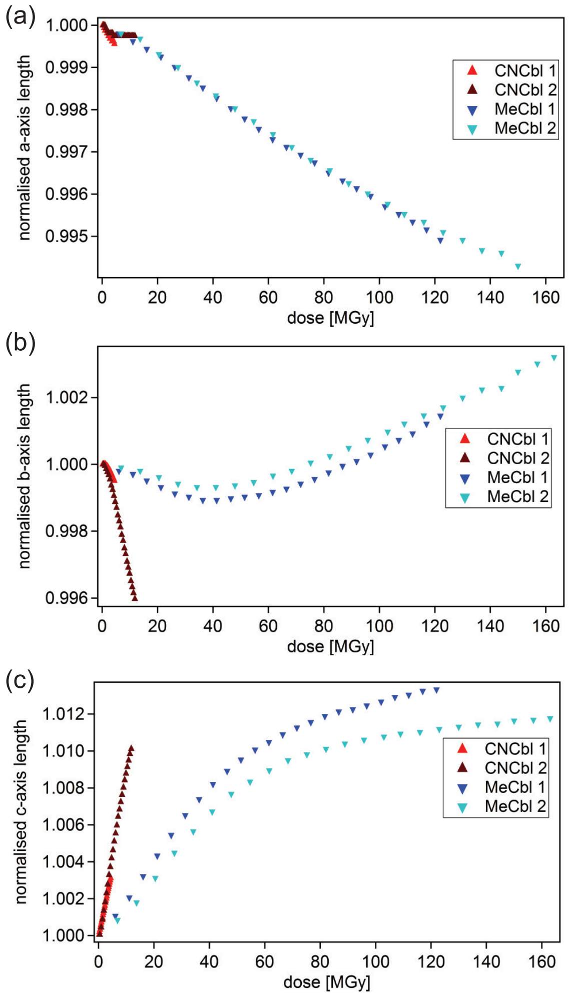

Figure 1.3: Normalised lengths of the a-axis (a), b-axis (b) and c-axis (c) for both cyanocobalamin crystals (red) and both methylcobalamin crystals (blue) at 100 K as function of dose.

amin and methylcobalamin. In case of both methylcobalamin crystals, it decreases linearly with dose. An overall decrease of 0.5% can be observed at maximum dose for the first methylcobalamin crystal and a decrease of 0.6% for the second crystal. In case of the first cyanocobalamin the normalised value decreases slightly with dose. In case of the second cyanocobalamin crystal, a more or less constant value can be observed.

The normalised b-axis lengths of all four samples are shown in fig. 1.3 (b). In case of the methylcobalamin crystals, the b-axis first slightly decreases, reaches a local minimum and then increases again at higher doses. In case of both cyanocobalamin crystals, the b-axis decreases strongly with dose. For the second cyanocobalamin crystal a shortening of 0.4% can be found.

Fig. 1.3 (c) shows the normalised c-axis lengths for all four samples as function of dose. The axis length increases in all four cases with the linear increase being three times more pronounced for cyanocobalamin with respect to methylcobalamin. In case of methylcobalamin the increase can be distinguished into two regimes. The axis length first increases strongly by 1.0% up to a dose of 60 to 80 MGy. At higher doses the increase is less pronounced. The increase for the second cyanocobalamin crystal also reaches 1.0% at maximum dose.

Both cyanocobalamin datasets show a drastic increase of the ITDP of one specific hydrogen atom, H9 (see fig. 1.5), which is part of a primary hydroxyl group, located at the ribose moiety of the cofactor. ITDPs of H9 for all four crystals are shown in fig. 1.4 (a). For methylcobalamin the hydrogen ITDP remains constant with dose, whereas for cyanocobalamin the ITDP strongly increases with dose. Fig. 1.4 (b) shows a plot of the ITDPs for cyanocobalamin on a dose scale between 0 and 15 MGy. The ITDP only increases slowly up to a dose of 2 MGy and then starts to grow rapidly. Above doses of 3 and 4 MGy, respectively, it reaches a constant value at 2.0000 Å^2 which corresponds to the diverging of the ITDPs. This is an indicator for an abstraction of the respective hydrogen atom.

Fig. 1.4 (c) and (d) show the absolute and normalised bond length change of the C56-O9-bond, at which the hydrogen abstraction appears to take place, respectively. A slight

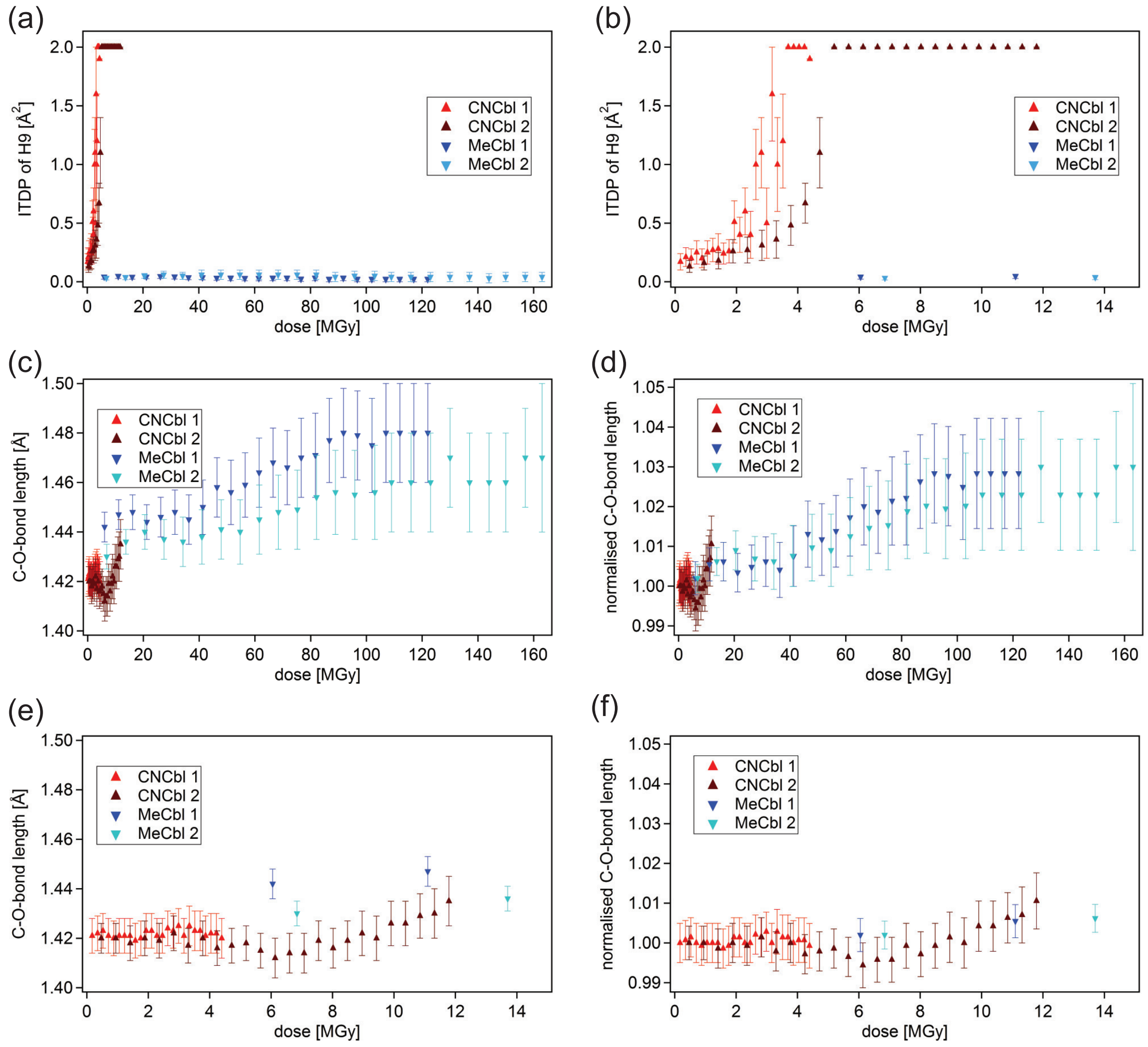

Figure 1.4: ITDPs of hydrogen atom H9 for cyanocobalamin (red) and methylcobalamin (blue) for the full dose series (a) and on a dose scale up to a maximum dose of 15 MGy (b). Absolute (c) and normalised (d) bond length change of the C56-O9-bond of cyanocobalamin (red) and methylcobalamin (blue) for the full dose series. Absolute (e) and normalised (f) bond length change of the C56-O9-bond up to a maximum dose of 15 MGy.

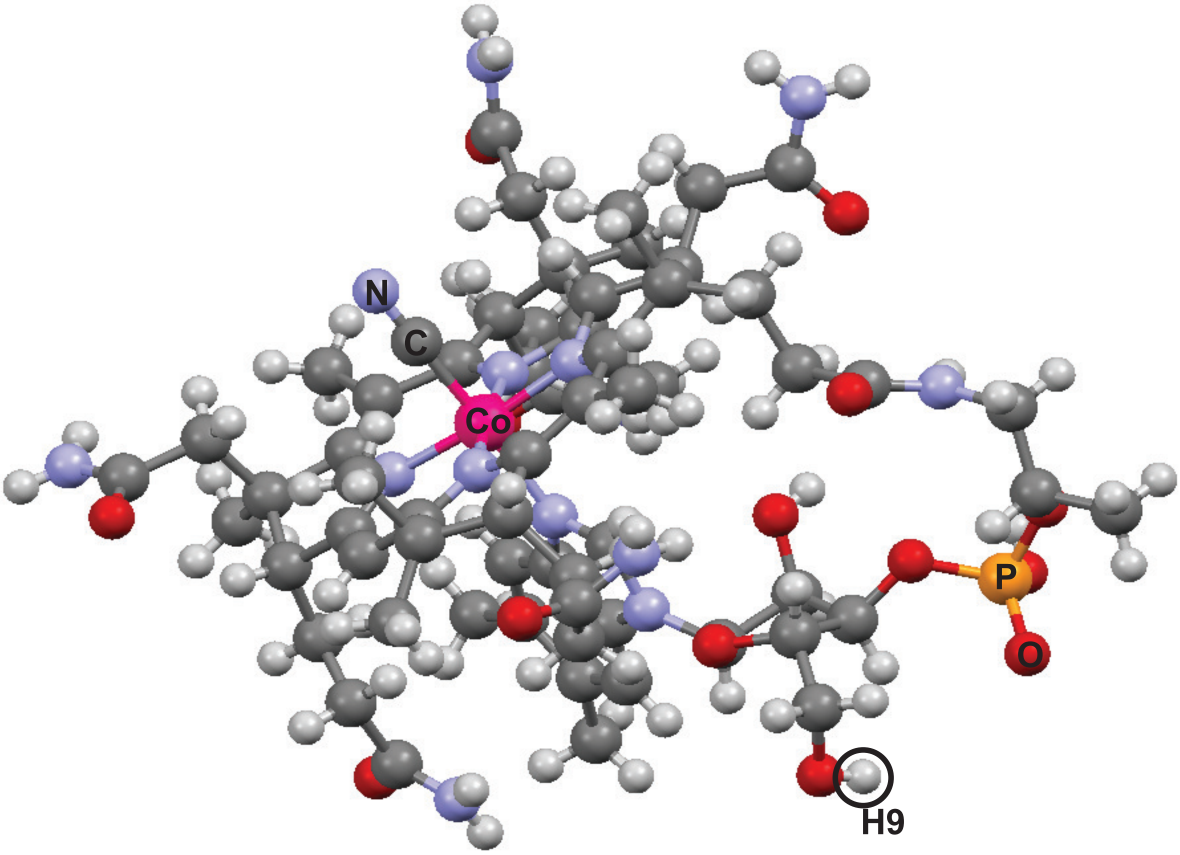

Figure 1.5: Position of the H9 atom in cyanocobalamin.

increase of the bond length can be observed for both methylcobalamin samples. However, the bond length change displays a large standard deviation at higher doses.
In fig. 1.4 the absolute (e) and normalised (f) bond length change for cyanocobalamin is shown on a dose scale between 0 and 15 MGy. Here, no pronounced change in the bond lengths can be observed for both cyanocobalamin crystals.

1.1.1 Temperature dependent X-ray diffraction measurements of cyanocobalamin

In this section, a comparison between dose series of cyanocobalamin collected at 100 K and 200 K is made. Detailed information on experimental details and crystallographic data for both crystals can be found in the appendix in section A.4. The data obtained for crystal CNCbl 2 was chosen as the 100 K dataset.
Fig. 1.6 (a) and (b) show the absolute and normalised mean intensity of cyanocobalamin at 100 K (red) and 200 K (blue) as function of dose, respectively. Since the measurements were conducted during the same beamtime with a similar incident photon flux, comparison of the absolute mean intensity values was performed. The absolute starting value of the mean intensity at 100 K is higher than the starting value for 200 K. However, it is possible that after only one full rotation the crystal measured at 200 K has suffered a significant loss in diffraction intensity and that the initial mean intensity is comparable. Evaluation of only the first 90° of the 200 K dataset was therefore performed. The initial mean intensity obtained from this evaluation, however, was not different from that obtained for the full rotation.
The decrease in intensity at 200 K takes place up to a dose of 6 MGy and remains constant afterward, whereas at 100 K the decrease appears to be more pronounced. The intensity keeps decaying above 12.5 MGy.
Fig. 1.6 (c) shows the mosaicity as function of dose at 100 K and 200 K. At 200 K the mosaicity increases linearly with dose up to 11 MGy where a sudden jump occurs, followed by a further linear increase to 0.6°. Above 20 MGy, no further increase in mosaicity can

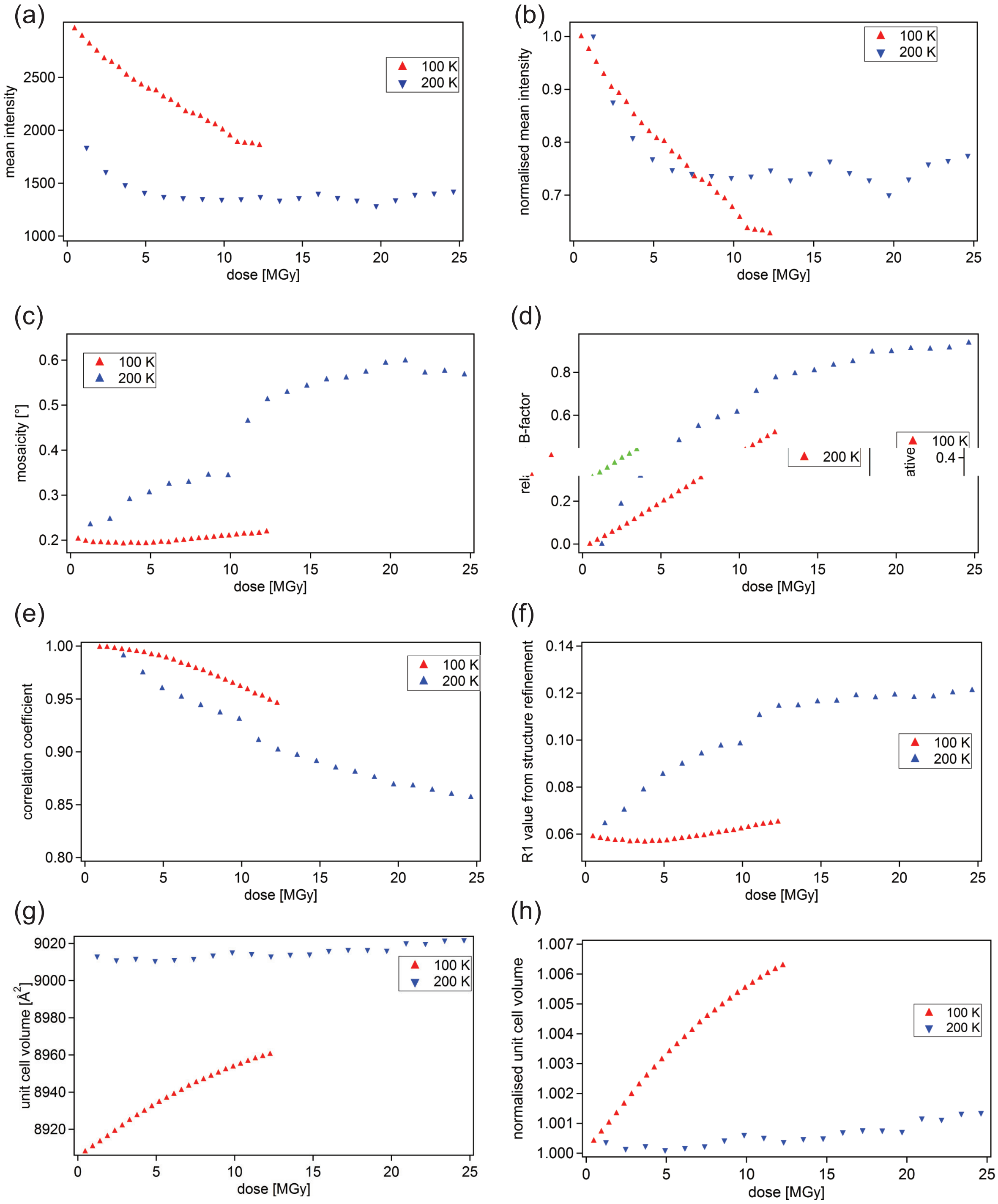

Figure 1.6: Absolute (a) and normalised (b) mean intensity, mosaicity (c), relative B-factor (d), correlation coefficient (e), R1 value from structure refinement (f), absolute (g) and normalised (h) unit cell volume of cyanocobalamin at 100 K (red) and 200 K (blue) as function of dose.

be observed. At 100 K the mosaicity stays approximately constant around 0.2° with only a slight increase at higher doses.

The relative B-factor shown in fig. 1.6 (d) shows a more or less linear decrease up to a dose of 14 MGy at 100 K. The relative B-factor at 200 K first increases strongly with dose, but shows a less pronounced increase at higher doses. A similar behaviour might also take place at 100 K, but is not visible due to the much lower dose on that sample.

The correlation coefficient for both measurements can be seen in fig. 1.6 (e). At 100 K the correlation coefficient remains nearly constant at first and starts to decrease in a linear manner above a dose of 8 MGy. At 200 K a linear decrease, which is more pronounced than at 100 K, is observed right from the start.

Fig. 1.6 (f) shows the increase of the R1 value from structure refinement at 100 K and 200 K as function of dose. The initial R1 value for 200 K is of the same order of magnitude as the R1 value for maximum dose at 100 K and increases strongly with dose. The R1 value from structure refinement at 200 K seems to reach a plateau at 0.12 at higher doses. In contrast to this, the initial R1 value at 100 K is around 0.06 and increases only slightly with dose.

The initial absolute unit cell volume shown in fig. 1.6 (g) differs significantly for both temperatures: at 100 K the unit cell volume first increases strongly and then increases in a less pronounced fashion above 8 MGy, whereas at 200 K the increase is more or less continuous.

Fig. 1.6 (h) shows the normalised unit cell volume increase for both temperatures. At 200 K a slight increase of 0.1% at 25 MGy can be observed while at 100 K it increases by 0.6% for a dose of 12 MGy.

Fig. 1.7 shows the absolute (a) and normalised (b) Co-C-bond length as well as the absolute (c) and normalised (d) Co-N-bond length at 100 K and 200 K. The 200 K dataset shows larger standard deviations. For the Co-C-bond the datapoints at doses above 10 MGy are widely spread and do not show any clear trend anymore. The initial Co-C-bond length, however, is similar for both temperatures (1.87 Å). At 200 K the Co-C-bond length stays constant up to 10 MGy while at 100 K it shows a clear increase. The

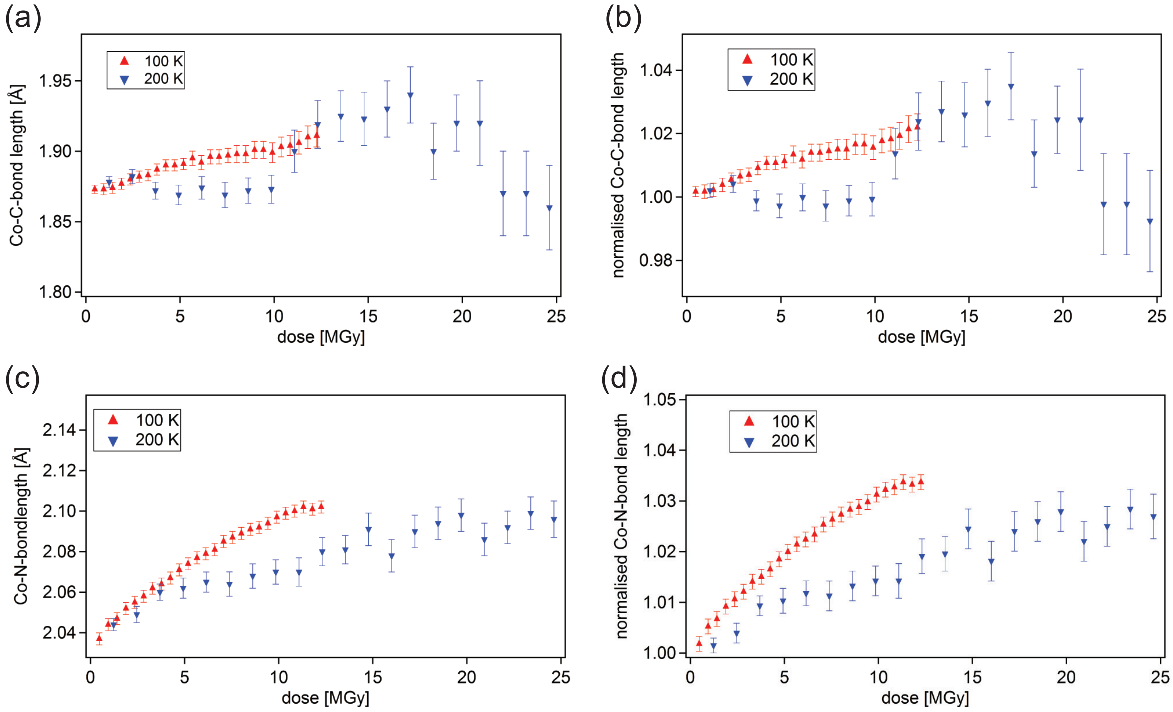

Figure 1.7: Absolute (a) and normalised (b) bond length changes of the Co-C-bond (upper axial ligand) and absolute (c) and normalised (d) bond length changes of the Co-N-bond (lower axial ligand) as function of dose.

relative bond length change reveals an elongation of the Co-C-bond by 2.0% at maximum dose.

The Co-N-bond length change follows a clear course for both temperatures. Starting at an initial value of 2.04 Å, the elongation with dose is more pronounced at 100 K. At maximum dose (13 MGy) the bond length reaches a plateau at 2.10 Å. The plateau at 200 K is reached at the same value, however, the error of this refinement is larger, resulting in less reliable data. The normalised bond length changes display an elongation of the Co-N-bond by 3.3% at 100 K and an elongation by 2.5% at 200 K.

Fig. 1.8 (a) and (b) show the absolute and normalised a-axis lengths at 100 K and 200 K, respectively. The initial a-axis length is longer at 200 K. At 100 K the cell axis length remains more or less constant for the whole dose series. At 200 K the a-axis length first increases by around 0.4% to 0.5% up to 15 MGy and increases only slightly at higher doses.

In fig. 1.8 (c) and (d) the absolute and normalised b-axis lengths at 100 K and 200 K are shown. In this case, the initial b-axis length is similar at both temperatures. At 100 K the axis length decreases in a linear fashion by about 0.5% at the maximum dose. At 200 K the decrease is five times more pronounced compared to 100 K. The length first decreases by about 2.0% to a dose of 15 MGy and decreases slower at higher doses.

Fig. 1.8 (e) and (f) show the absolute and normalised c-axis lengths at 100 K and 200 K as function of dose. The initial c-axis length is longer at 200 K compared to 100 K. The axis-length increases in both cases as function of dose. At 100 K a linear increase by about 1.0% at maximum dose can be observed. In case of the 200 K crystal, an increase by 1.6% with dose is found. Up to a dose of 10 MGy, a pronounced increase can be observed. At higher doses the increase is less pronounced.

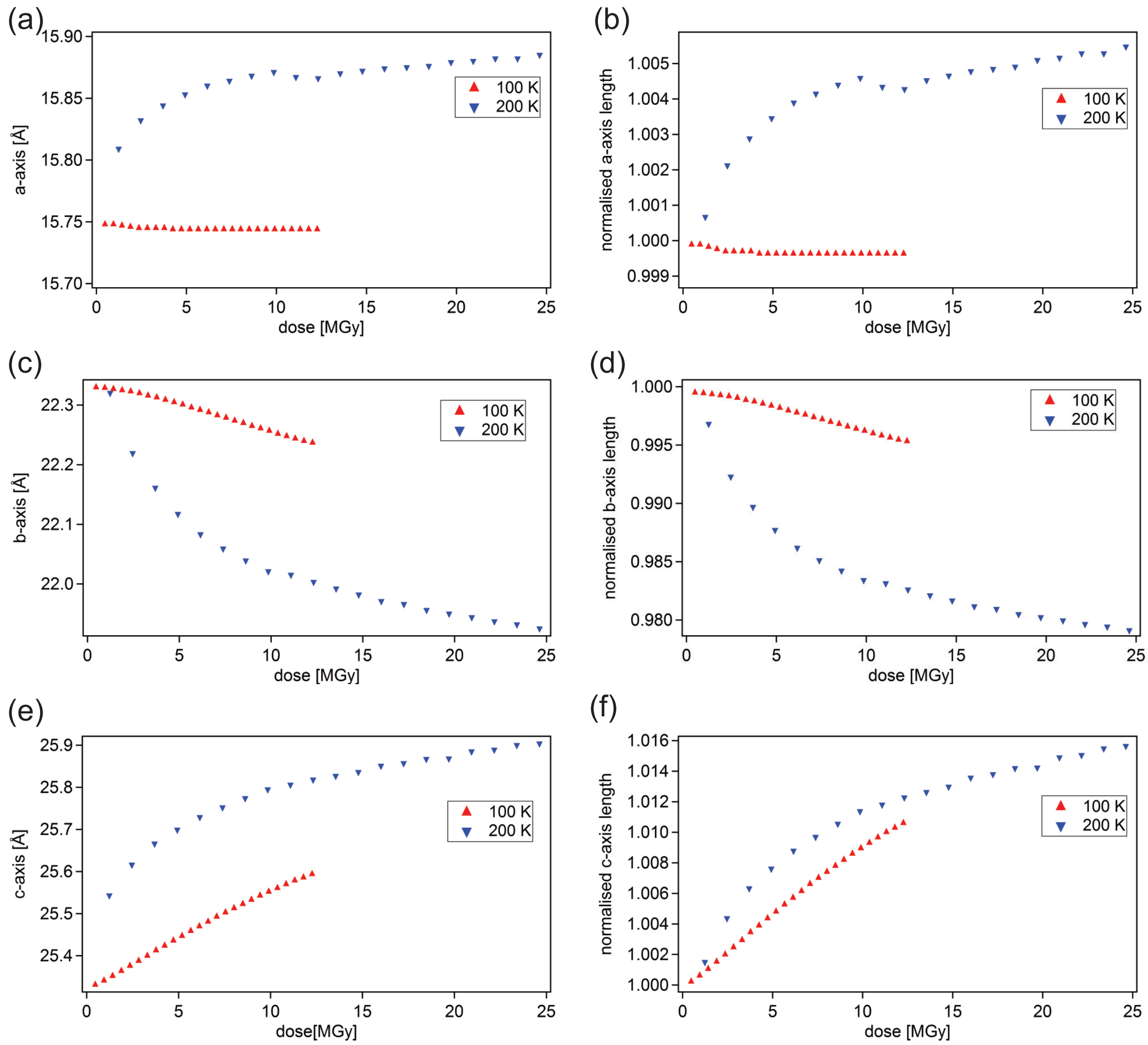

Figure 1.8: Absolute and normalised cell axis lengths of the a-axis (a and b), b-axis (c and d) and c-axis (e and f) at 100 K (red) and 200 K (blue) as function of dose, respectively.

1.2 Amino acids and thymidine

In the following section the results from crystallographic measurements on L-serine, L-alanine and thymidine are presented. Detailed information on experimental details and crystallographic data can be found in the appendix in section A.5.

1.2.1 L-serine

Fig. 1.9 (a) shows the radiation induced mean intensity decay of L-serine as function of dose obtained from X-ray diffraction measurements. It decreases in a linear fashion up to 80 MGy. Above 80 MGy, it remains approximately constant with a higher variability.

In fig. 1.9 (b) the crystal mosaicity is shown as function of dose. Up to 55 MGy, the mosaicity stays at around 0.20° and increases in a linear fashion to 0.58° above 55 MGy. A loss in data quality and reliability above 95 MGy is apparent here as well.

As shown in fig. 1.9 (c) the relative B-factor increases in an exponential manner from 0.0 to approximately 4.0 as function of dose.

In fig. 1.9 (d) the correlation coefficient between the first and the subsequent datasets of a dose series can be seen. The correlation coefficient continuously decreases up to 95 MGy. Above 95 MGy, it exhibits a higher variability and shows a more pronounced decrease.

The R1 value from structure refinement and the unit cell volume as function of dose are shown in fig. 1.9 (e) and (f), respectively. The R1 value from structure refinement remains below 0.040 for the first three data points and then increases in a linear fashion up to a value of nearly 0.080 at a dose of 80 MGy. At higher doses the R1 value starts to vary between 0.075 and 0.100. Overall, the increase shows a linear behaviour up to a R1 value of 0.110.

The unit cell volume increases in a linear fashion from around 445 Å^3 to around 470 Å^3. The loss in reliability above 80 MGy observed previously can be found here as well.

The bond length change of the C2-O3-bond up to 100 MGy is shown in fig. 1.11 (a). A significant bond shortening with dose is visible in this case.

Fig. 1.11 (b) shows the normalised bond lengths of all bonds in the compound up to a

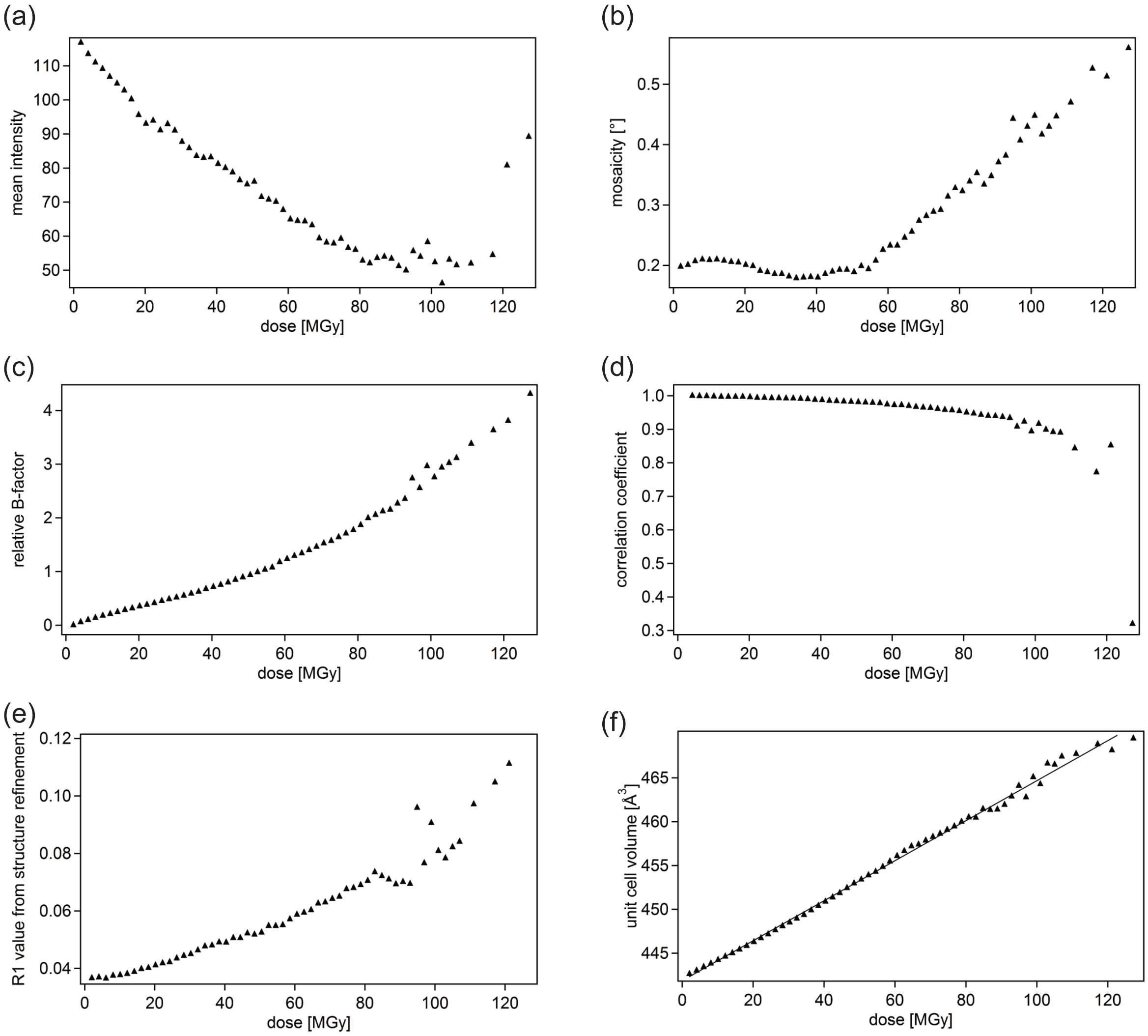

Figure 1.9: Mean intensity (a), mosaicity (b), relative B-factor (c), correlation coefficient (d), R1 value from structure refinement (e) and unit cell volume (f) of L-serine measured at an energy of 17.5 keV and a temperature of 100 K as function of dose.

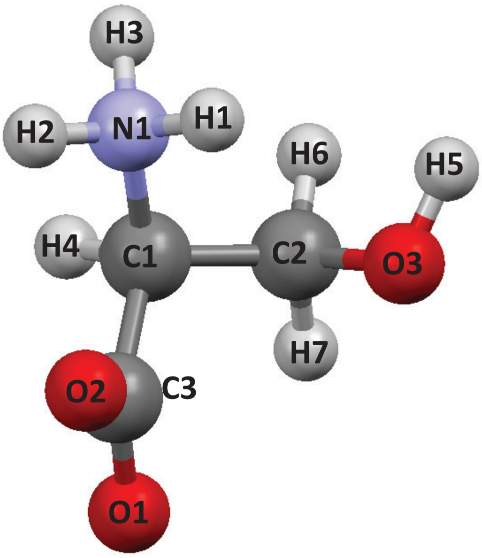

Figure 1.10: Labeling scheme for L-serine.

dose of 100 MGy. Although small changes can be found for almost all bonds at higher doses, a clearly pronounced change during the whole dose series can only be observed for the C2-O3 bond.

Fig. 1.11 (c) shows the refined ITDPs of all hydrogen atoms as function of dose up to 100 MGy. All hydrogen ITDPs are very small and only increase slightly with dose, except for H5 (located at the primary hydroxyl group of L-serine) which already displays a large value for the first dataset. The ITDP of H5 increases significantly with dose.

1.2.2 L-alanine

Fig. 1.12 (a) shows the mean intensity of L-alanine from X-ray measurements as function of dose. The mean intensity decreases from 160 to 145 for the dose series. The loss in intensity occurs in a linear fashion up to 20 MGy. Above 20 MGy, the mean intensity remains constant until above 40 MGy where the linear decrease continues.

The crystal mosaicity as function of dose is shown in fig. 1.12 (b). Except for one outlier, the mosaicity stays between 0.15° and 0.18° during the whole dose series.

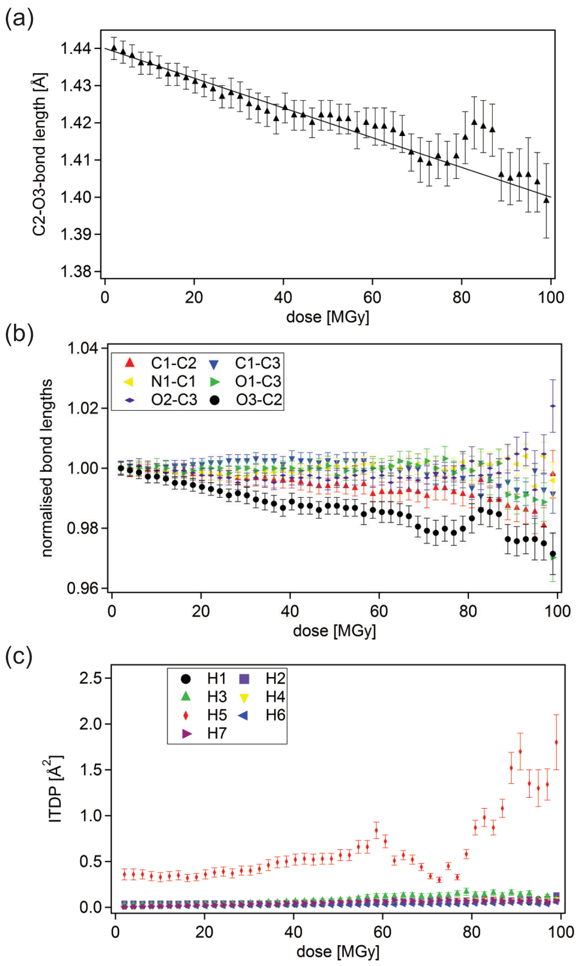

Figure 1.11: Absolute C2-O3-bond length (a), normalised bond lengths of all bonds (b) and ITDPs of all hydrogen atoms (c) of L-serine as function of dose, truncated to 100 MGy.

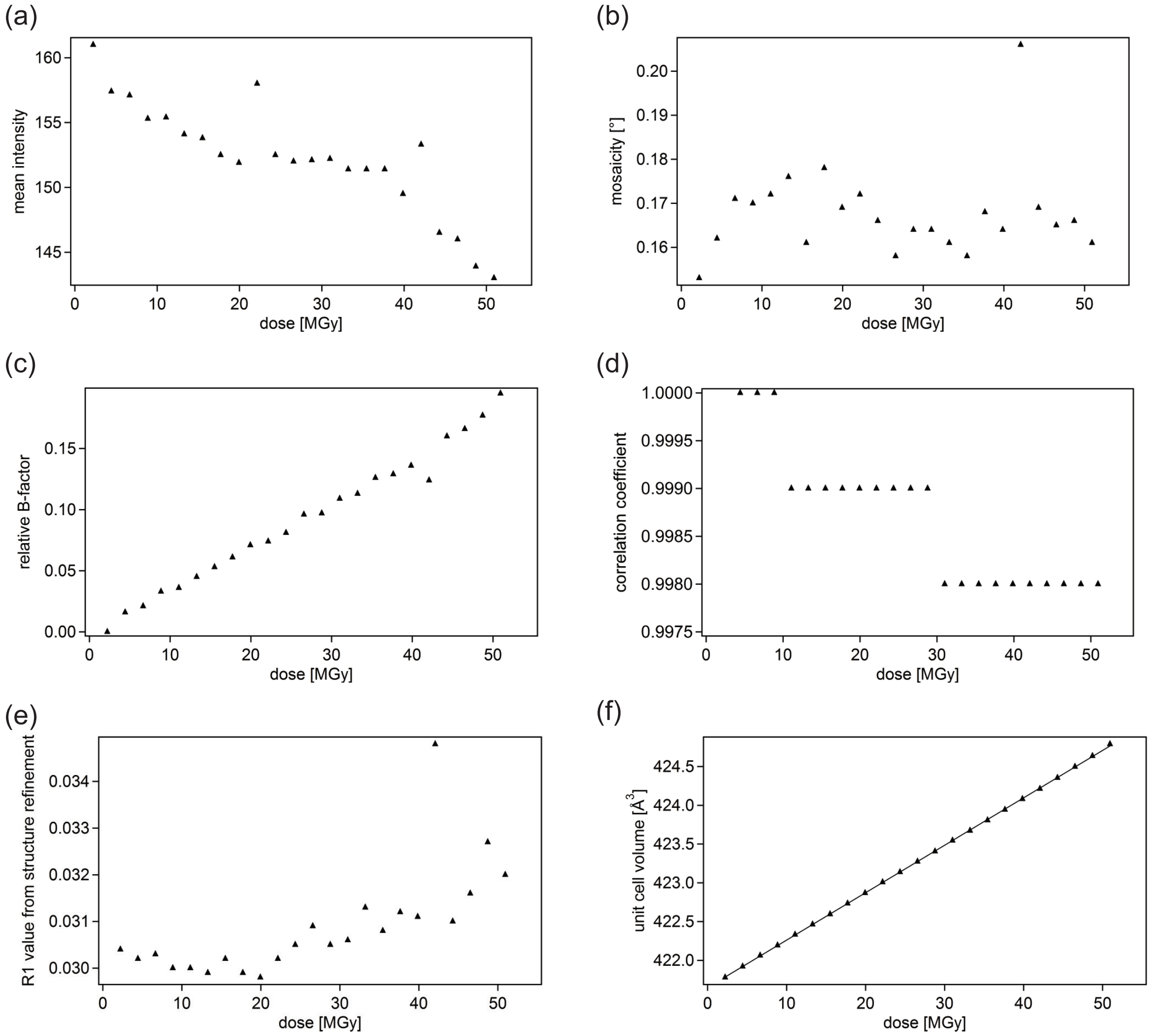

Figure 1.12: Mean intensity (a), mosaicity (b), relative B-factor (c), correlation coefficient (d), R1 value from structure refinement (e) and unit cell volume (f) of L-alanine measured at an energy of 16.4 keV and a temperature of 100 K as function of dose.

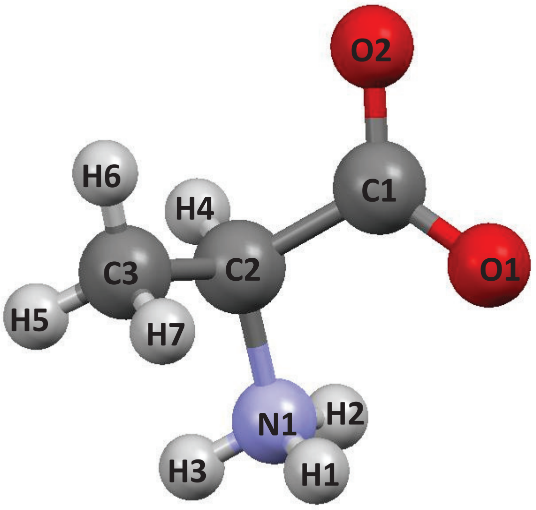

Figure 1.13: Labeling scheme for L-alanine.

Fig. 1.12 (c) shows the relative B-factor which increases from 0.0 to 0.2.

Changes in the correlation coefficient can be seen in fig. 1.12 (d). The loss in correlation with dose is minimal (1.000 at 0 MGy to 0.998 at 50 MGy).

In fig. 1.12 (e) the R1 value from structure refinement as function of dose is shown. It shows a slight increase of R1 from 0.030 at 0 MGy to 0.033 at maximum dose. The one outlier found for the mosaicity values can be seen in the R1 value as well.

Fig. 1.12 (f) shows the unit cell volume of L-alanine as function of dose. The unit cell volume increases linearly from around 421 Å to around 424 Å.

In Fig. 1.14 (a) the normalised bond lengths of all bonds within the L-alanine molecule are shown as function of dose. None of the bond lengths increases significantly with dose. Fig. 1.14 (b) shows the ITDPs of all hydrogen atoms within L-alanine (for labeling of all hydrogen atoms see fig. 1.13). For L-alanine no hydrogen atom shows a significant increase in its ITDP and all values remain within the range of 0.005 Å^2 and 0.020 Å^2.

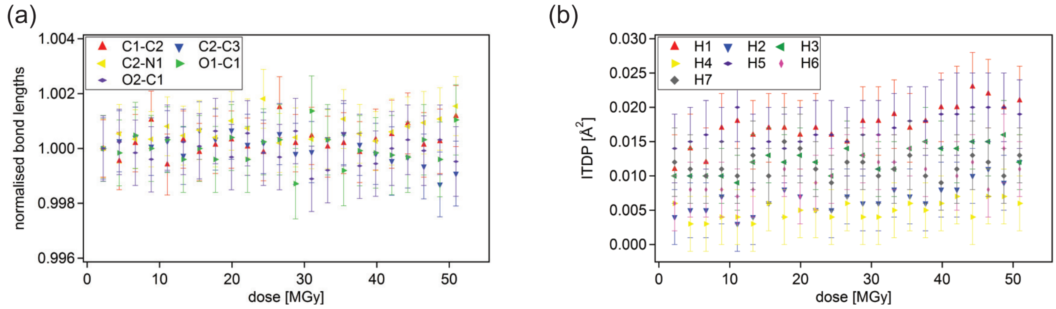

Figure 1.14: Normalised bond lengths (a) and ITDPs of all hydrogen atoms of L-alanine as function of dose.

1.2.3 Comparison between L-serine and L-alanine

For comparison between the radiation-induced behaviour of L-serine and L-alanine the normalised mean intensity (a), normalised unit cell volume (b), relative B-factor (c) and correlation coefficient are compared in fig. 1.15. The mean intensity decay is much more pronounced for L-serine than for L-alanine and the normalised unit cell volume increases three times faster for L-serine than for L-alanine (a pitch of 5.16×10^{-4} MGy^{-1} for L-serine compared to 1.45×10^{-4} MGy^{-1} for L-alanine).

The higher radiation hardness of L-alanine compared to L-serine is also reflected in the correlation coefficient: It remains nearly constant for the dose series of L-alanine, but decreases significantly with dose for L-serine (from 1.000 at 0 MGy to 0.998 at 50 MGy for L-alanine and from 1.000 at 0 MGy to 0.980 at 50 MGy for L-serine).

Finally the relative B-factors for both dose series are compared. While in the case of L-alanine only a slight increase with dose can be found the increase for L-serine is more pronounced. The relative B-factor of L-serine already reaches 1.0 at 50 MGy while L-alanine increases only to 0.2 at the same dose.

1.2.4 Thymidine

Fig. 1.16 (a) shows the mean intensity from X-ray diffraction measurements as function of dose. The intensity decreases in a linear fashion from 260 to 160 at maximum dose.

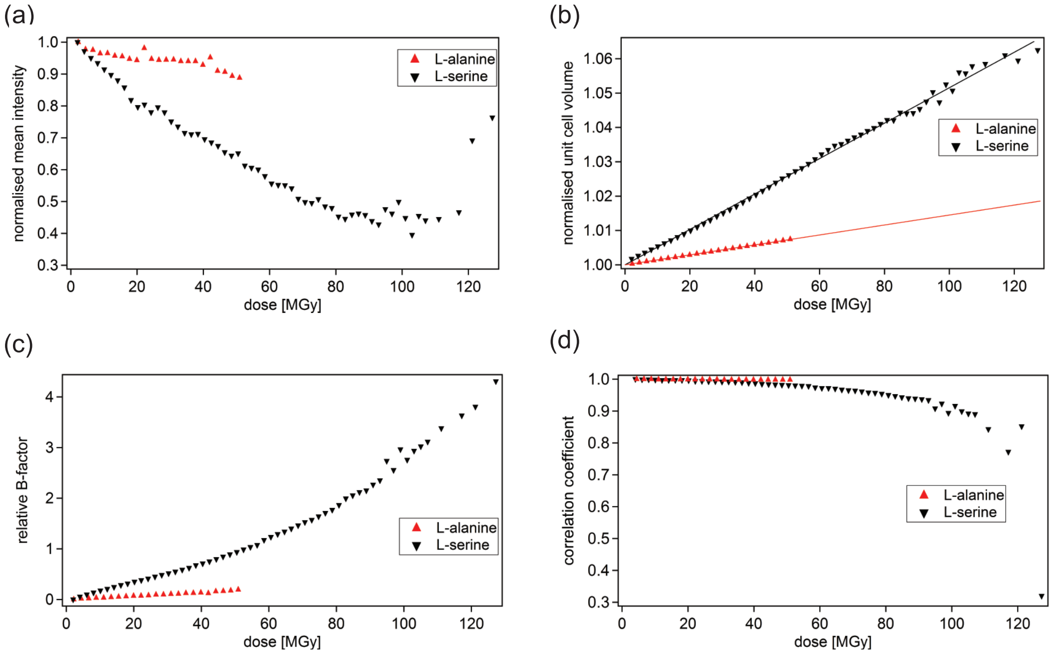

Figure 1.15: Comparison of the normalised mean intensity (a), normalised unit cell volume (b), relative B-factor (c) and correlation coefficient (d) of L-alanine (red) and L-serine (black).

In fig. 1.16 (b) the crystal mosaicity as function of dose is shown. The mosaicity value starts at 0.26°, decreases to a minimum of 0.14° between 40 MGy and 60 MGy and increases again to 0.26° at 100 MGy. Such an effect has been observed from time to time in our measurements. The reason for this is not understood so far.

Fig. 1.16 (c) shows the relative B-factor of the thymidine crystal which increases in a linear fashion to 0.9 at maximum dose.

The correlation coefficient shown in fig. 1.16 (d) decreases from 1.000 to 0.990 during the measurement.

The R1 value from structure refinement (fig. 1.16 (e)) starts at around 0.025 and increases to 0.050 at maximum dose. The value remains almost constant for the first few datasets up to 20 MGy and then increases continuously.

Fig. 1.16 (f) shows the unit cell volume of thymidine as function of dose. The initial unit cell volume is 1072 Å and increases with dose. At higher doses (above 50 MGy) the increase is less pronounced.

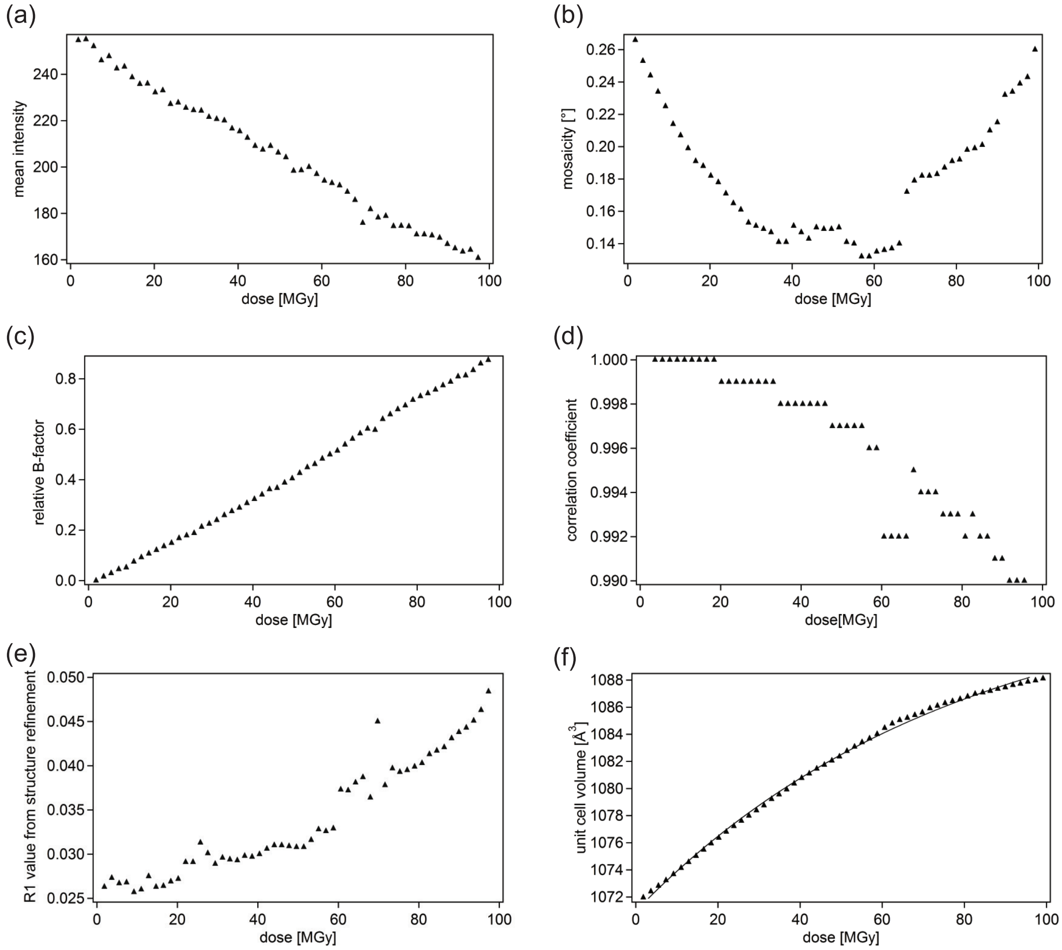

Figure 1.16: Mean intensity (a), mosaicity (b), relative B-factor (c), correlation coefficient (d), R1 value from structure refinement (e) and unit cell volume (f) of thymidine measured at an energy of 17.5 keV and a temperature of 100 K as function of dose. The decrease in mosaicity is a small effect sometimes observed in crystallographic data which has not been understood so far.

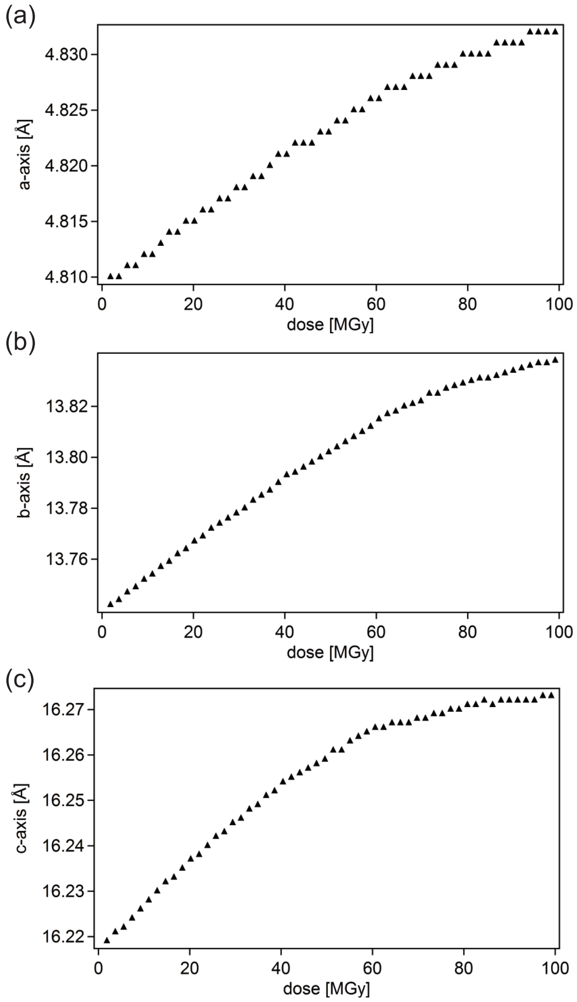

Figure 1.17: Lengths of the a-axis (a), b-axis (b) and c-axis (c) of the unit cell of thymidine as function of dose.

Figs. 1.17 (a), (b) and (c) show the lengths of the a-, b- and c-axis of thymidine as function of dose, respectively. The increase occurs in the same fashion for all three axes. The b-axis seems to be affected the most.
The a-axis increases by 0.02 Å for the whole dose series, whereas the b-axis increases by 0.10 Å. An increase by 0.05 Å can be observed for the c-axis.

The excellent R1 value obtained from the thymidine structure refinement allowed for an investigation of the bond length changes in the same fashion as for L-serine. Fig. 1.19 (a) shows the normalised bond lengths of all bonds in the thymidine molecule as function of

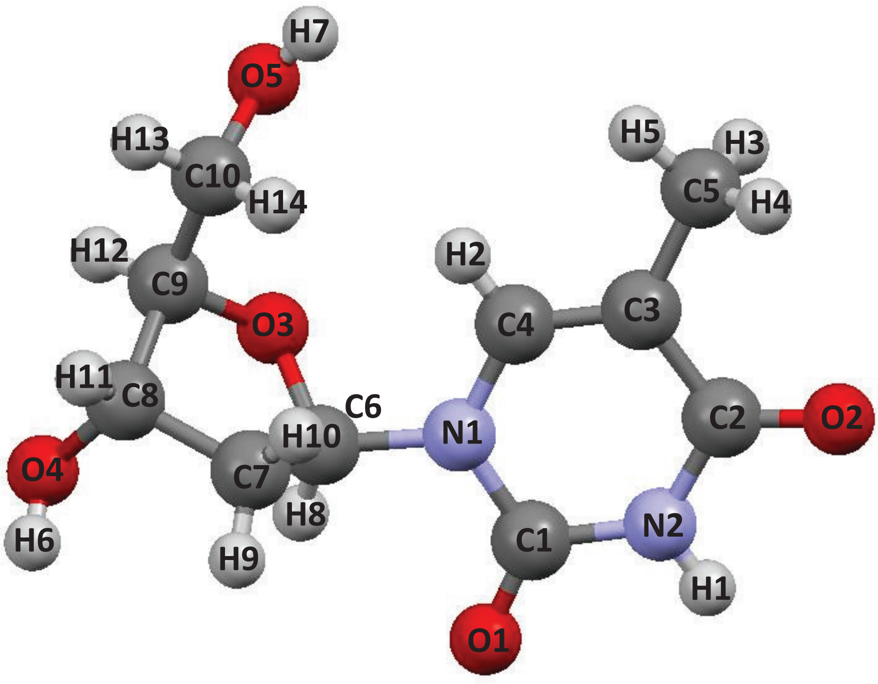

Figure 1.18: Labeling scheme for thymidine.

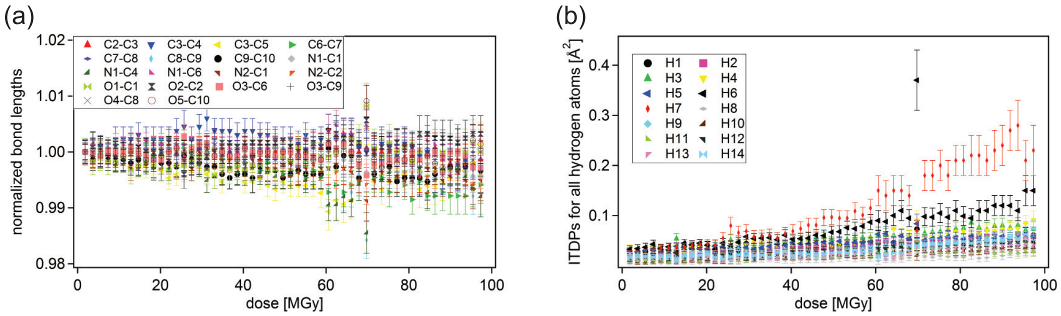

Figure 1.19: Normalised bond lengths (a) and ITDPs of all hydrogen atoms (b) of thymidine as function of dose.

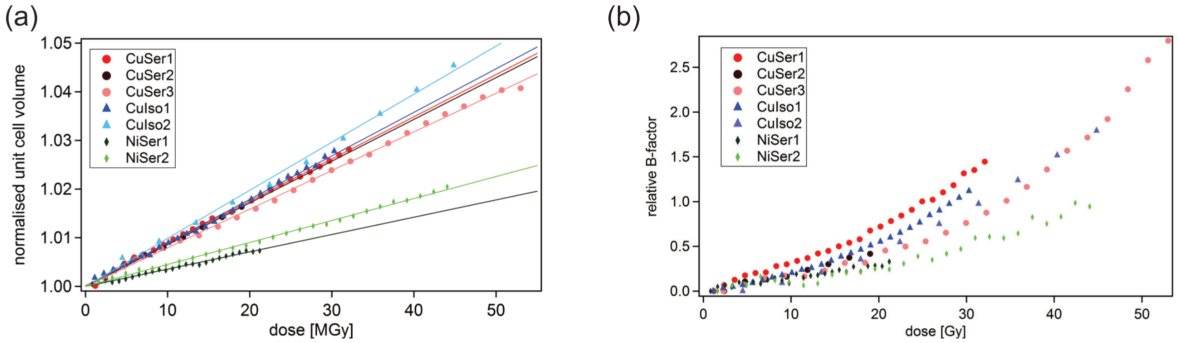

Figure 1.20: Normalised cell volume (a) and relative B-factor (b) increase for all crystals measured at an energy of 15.31 keV and a temperature of 100 K as function of dose.

dose. In this case, no significant changes could be observed.

In fig. 1.19 (b) the refined ITDPs of all hydrogen atoms of thymidine are shown. While all of them display a small linear increase, the increase of the ITDP of H7 is clearly more pronounced. H6 also shows a slightly stronger increase. Both hydrogen atoms are part of hydroxyl groups located at the ribose-moiety of thymidine (see fig. 1.18).

1.3 Metal amino acid complexes

Due to the poor data quality of the NiSer crystals, only the normalised unit cell volume increase and relative B-factor were used for comparison with CuSer and CuIso. Normalised mean intensity, correlation coefficient as well as R1 value from structure refinement were also extracted, but failed to provide conclusive results.

Detailed information on measurement values and crystal data can be found in the appendix in section A.6. Fig. 1.20 shows the normalised unit cell volume increase (a) and the relative B-factor (b) for all three compounds as function of dose. A linear fit function was applied to the unit cell volume.

The normalised unit cell volume increases in a similar fashion for all three CuSer datasets as well as for both CuIso datasets. The maximum dose absorbed by the samples is around

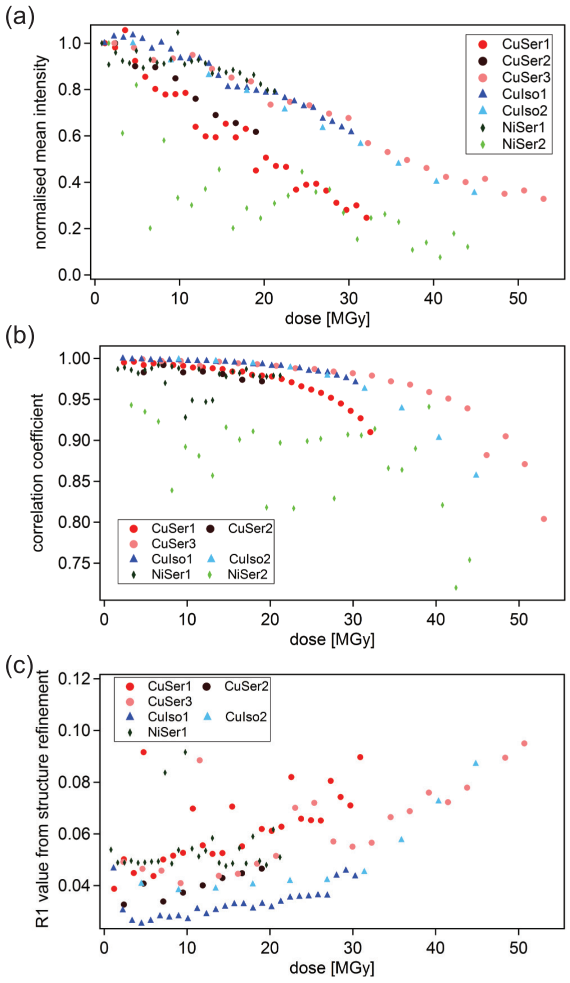

Figure 1.21: Normalised mean intensity (a), correlation coefficient (b) and R1 value (c) from refinement for all three compounds as function of dose. These values were not used for comparison of the damage processes because they gave no conclusive results for the nickel-serine crystals.

50 MGy. At 50 MGy, the unit cell volume increases by 4.5% for the first and second crystal of CuSer whereas for the third crystal the increase is only 4.0%. The CuIso crystals show a similar behaviour, increasing by 4.8% for the first and by 5.0% for the second crystal.

For NiSer the increase of the normalised unit cell volume is only half as pronounced as for the copper complexes. For a dose of 50 MGy an increase of only 2% can be observed. The relative B-factors shown in fig. 1.20 (b) do not show such pronounced differences between the nickel and copper complexes. A slightly slower increase can be seen for the two NiSer datasets, especially at higher doses. The relative B-factor increase for the second and third crystal of CuSer is slightly lower than the one determined for the first crystal. The second CuIso crystal shows a behaviour similar to that of the third CuSer crystal. The behaviour of the first CuIso crystal resembles that of the first crystal measured for CuSer. However, the data quality is not sufficient to draw final conclusions.

2 X-ray absorption measurements

2.1 Cyanocobalamin

Cyanocobalamin was measured at the Co(III) K-edge. The K pre-edge and edge region showed significant changes with dose for solid cyanocobalamin. Fig. 2.1 (a) shows a dose series of solid cyanocobalamin measured at 100 K. With increasing dose, the absorption edge clearly shifts toward lower energies. Additionally, the second pre-peak which is clearly visible in the first spectrum disappears at higher doses. The intensity of the first white line also decreases at higher X-ray doses. No significant changes can be observed above the white line.

Fig. 2.1 (b) shows a dose series of aqueous cyanocobalamin, measured at 100 K. Comparison of the dose series of solid and aqueous cyanocobalamin reveals no differences between the two sample environments.

In fig. 2.1 the E_0 values for all temperatures extracted from the measured spectra of solid (c) and aqueous (d) cyanocobalamin as a function of dose are shown. For both sample environments the same starting energy (7727.7 eV) can be observed. Exponential fitting reveals that the threshold value for the solid and aqueous samples differs slightly. In case of solid cyanocobalamin it is 7721.5 eV, whereas it decreases to 7720.9 eV for aqueous cyanocobalamin. The edge shift differs at different temperatures.

Fitting the different dose series by an exponential function revealed different exponential coefficients depending on the temperature. These exponential shift factors as function of temperature are shown in fig. 2.2 for solid (red) and aqueous (blue) cyanocobalamin. A sixfold reduced rate of photoreduction as function of dose can be found for solid

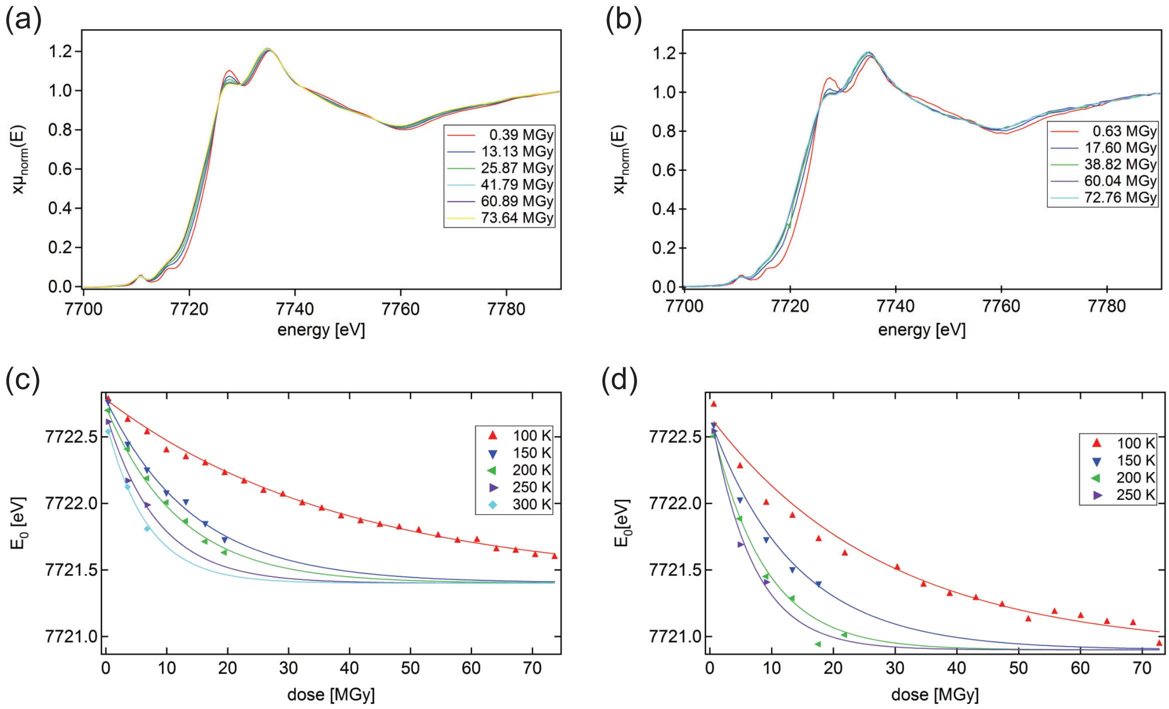

Figure 2.1: Dose series of XANES spectra of solid (a) and aqueous (b) cyanocobalamin collected at 100 K as function of energy and course of E_0 for solid (c) and aqueous (d) cyanocobalamin as function of dose.

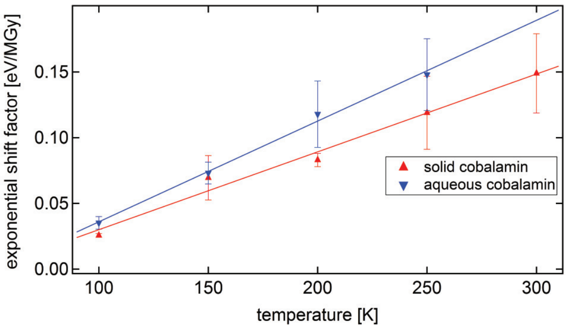

Figure 2.2: Exponential shift factors in [eV/MGy] as function of temperature for solid (red) and aqueous (blue) cyanocobalamin.

cyanocobalamin when decreasing the temperature from 300 K to 100 K. For aqueous cyanocobalamin a fivefold reduction is observed.

Additionally, measurements were performed at temperatures between 5 and 100 K using a helium cryostat. The spectra were noisy, as can be seen in fig. 2.3 (a) showing a dose series of XANES spectra at 5 K. This is probably due to turbulences caused by the cold helium gas stream. Similar to the measurements at 100 K using at nitrogen cryostat the disappearance of the second pre-edge peak, the shift of the K-edge and the intensity decrease of the first white line can be observed in the 5 K spectra as well.

Fig. 2.3 (b) shows the courses of the E_0 value extracted from fitting the absorption spectra as function of dose for all temperatures. Due to the fitting of the spectra a small difference in the initial E_0 value can be found. It varies between 7719.0 and 7719.4 eV, which is within the error of these experiments due to the noisy spectra (see section 2.2.2 in chapter 2 of the ***"Experimental"*** section). For higher X-ray doses the E_0 value shifts toward 7716.6 eV. In this case only a slight difference in the exponential energy shift factors could be observed for all measurements, as shown in fig. 2.3.

It has to be noted that the exponential shift factor at 100 K differs for the two measurements, performed with a liquid nitrogen and helium cryostat. The exponential shift factor obtained during the measurements between 100 K and 300 K was 0.0256 eV/MGy, whereas the exponential shift factor obtained during measurements between 5 K and 100 K was 0.0155 eV/MGy. This difference is most probably due to small inaccuracies in

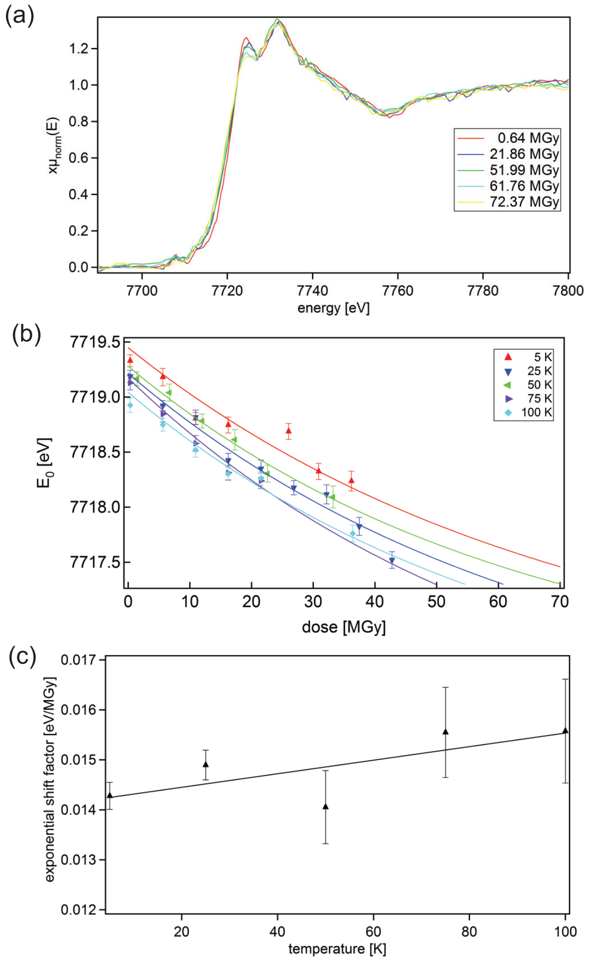

Figure 2.3: XANES spectra of cyanocobalamin at 5 K as function of energy (a), course of value E_0 for all temperatures as function of dose (b) and coefficient of the exponential fit ("exponential shift factor") as function of temperature (c). The slight difference within the values of E_0 is probably due to the noise within the spectra.

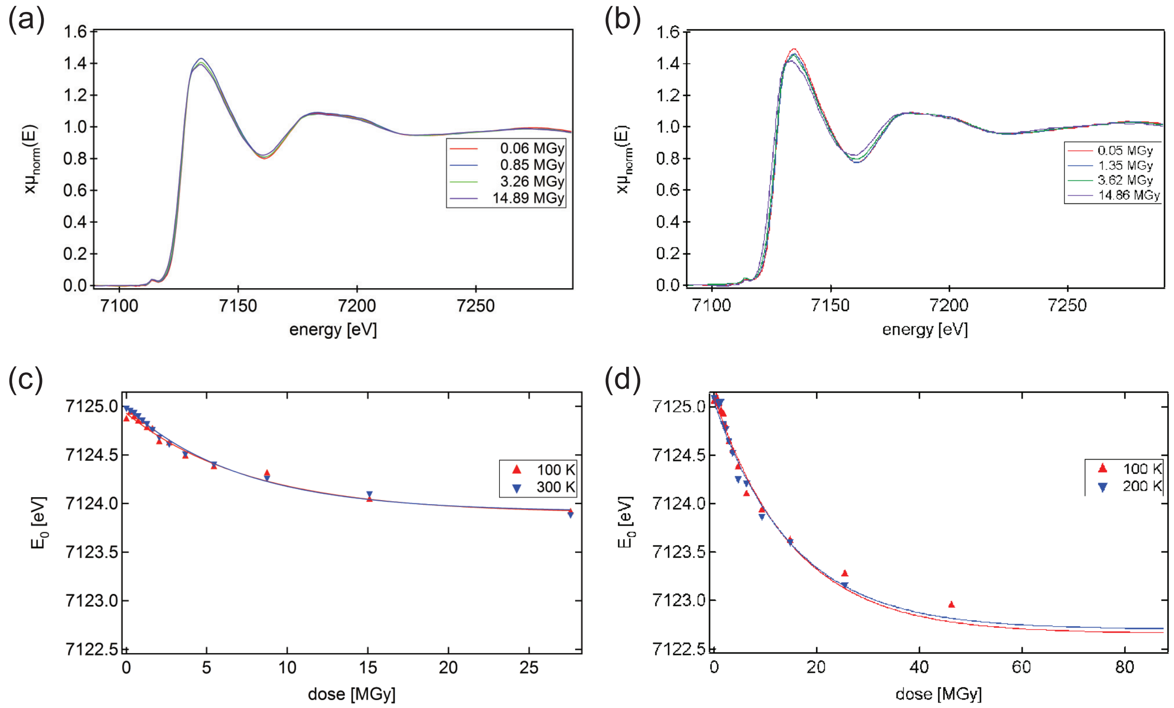

Figure 2.4: Dose series of XANES spectra of solid (a) and aqueous (b) ammonium ferric citrate at 100 K as function of energy and course of E_0 for solid (c) and aqueous (d) ammonium ferric citrate as function of dose.

photon flux determination and determination of the beam size at the sample, and, thus, in dose determination.

2.2 Iron compounds

2.2.1 Ammonium ferric citrate

All iron compounds were measured at the iron K-edge located around 7125 eV.

Ammonium ferric citrate was the only iron compound measured as a solid as well as in aqueous solution. Dose series of XANES spectra of solid (a) and aqueous (b) ammonium ferric citrate collected at 100 K are shown in fig. 2.4. Here, a shift of the absorption edge toward lower energies and a decrease of the intensity of the white line for higher X-ray

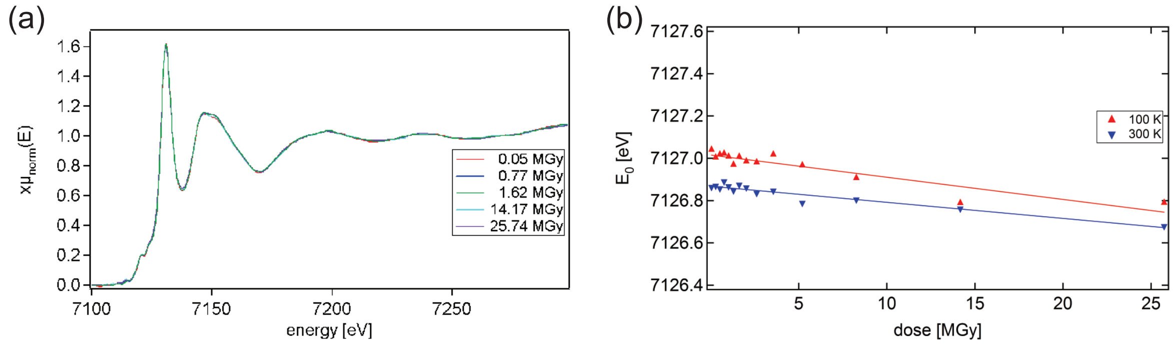

Figure 2.5: Dose series of XANES spectra of solid potassium hexacyanoferrate measured at 100 K as function of energy (a) and course of E_0 for solid potassium hexacyanoferrate as function of dose (b).

doses can be observed. Similarly to cyanocobalamin, the E_0 values were extracted and plotted as function of dose. The corresponding graphs are shown in figs. 2.4 (c) and (d). In agreement with the cyanocobalamin measurements, a larger edge shift can be observed in the aqueous solution compared to solid ammonium ferric citrate. In both cases E_0 starts at 77125.0 eV and shifts toward lower energies with dose, where it reaches a threshold value. For solid ammonium ferric citrate this threshold is 7123.9 eV and in case of the aqueous sample the threshold can be found at 7122.8 eV. In contrast to the cyanocobalamin measurements, the aqueous sample shows a reduced susceptibility to photoreduction compared to the solid sample. A temperature dependence as observed for cyanocobalamin is also not found in case of ammonium ferric citrate.

2.2.2 Potassium hexacyanoferrate

Dose series of XANES spectra of potassium hexacyanoferrate collected at 100 K are shown in fig. 2.5 (a). Long-term irradiation with X-rays did not lead to any significant spectral changes.

As shown in fig. 2.5 (b) the course of the extracted E_0 values shows only a slight linear decrease. This increase and the slight difference between the values obtained at 300 K and 100 K are within the energy resolution of the experiment and can therefore be neglected.

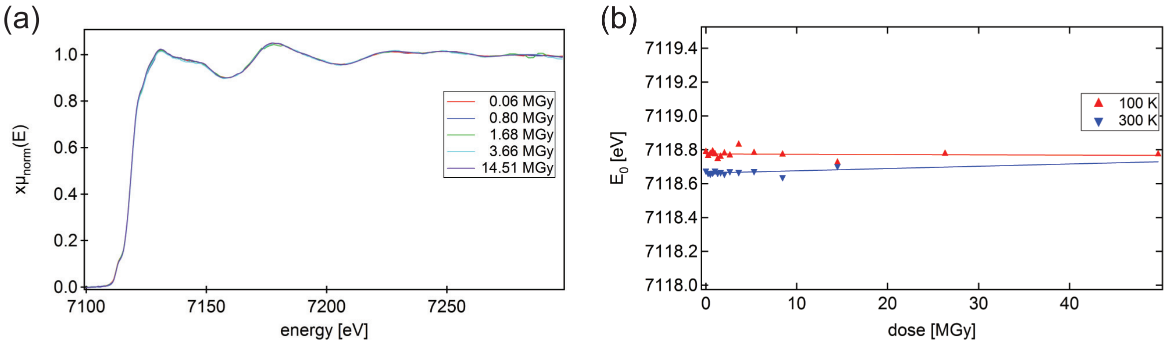

Figure 2.6: Dose series of XANES spectra of pyrite at 100 K as function of energy (a) and course of E_0 for pyrite as function of dose (b).

2.2.3 Pyrite

Dose series of pyrite collected at 100 K are shown in fig. 2.6 (a). No spectral changes can be observed and the course of E_0 also does not show any significant decrease as function of dose (see fig. 2.6 (b)).

2.2.4 Diiron-dithiolate

Dose series of spectra of diiron-dithiolate at 100 K and 300 K are shown in figs. 2.7 (a) and (b) respectively. Here, no shift of the absorption edge with dose is observed. At 100 K no significant spectral changes can be seen at all. In contrast to this, the spectra measured at 300 K show a significant increase of the white line with dose. The change of the white line (maximum value of $x\mu_{norm}$) as function of dose is given in fig.2.7 (c) for both temperatures.

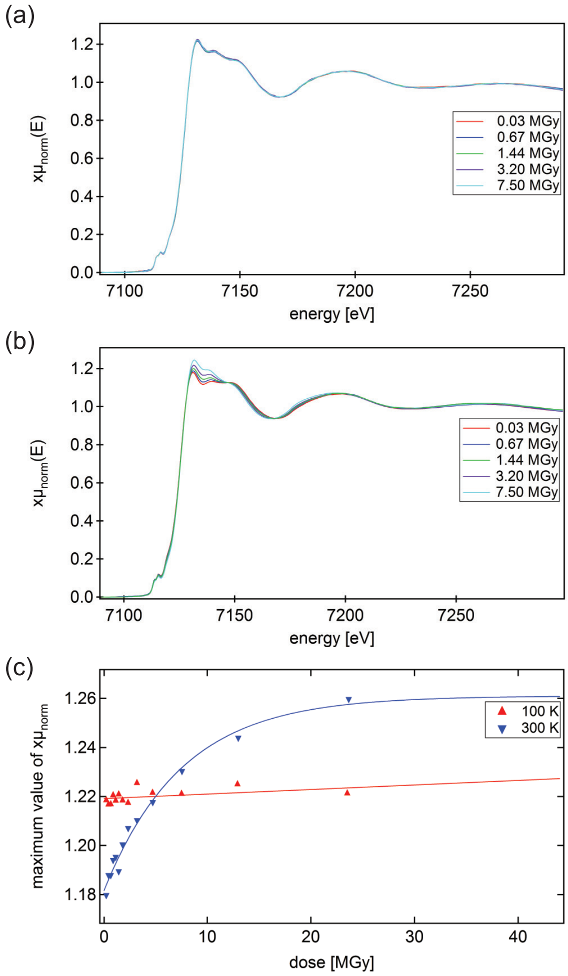

Figure 2.7: Dose series of XANES spectra of the organic iron cluster at 100 K (a) and 300 K (b) as function of energy and change of the white line at 100 K and 300 K as function of dose (c).

3 Neutron diffraction measurements

Since no conventional dose calculation was possible for white beam X-ray irradiation, the results of the neutron measurements were plotted as function of the (intensity corrected) X-ray exposure time, which can be assumed to be directly proportional to the dose.
Further information on refinement and occupancy values can be found in the appendix in section A.8.

3.1 L-serine

Fig. 3.1 (a) shows the unit cell volume increase determined by neutron diffraction as function of the X-ray exposure time. The unit cell volume increase was fitted by an exponential function as function of dose.
Fig. 3.1 (b) shows the freely refined occupancies of all seven hydrogen atoms of L-serine determined from neutron diffraction as function of the X-ray exposure time. The two hydrogen atoms H5 and H6 show a decrease in the occupancy of their position. All other hydrogen atoms show no significant occupancy changes in with increasing X-ray exposure time. The crystals which were not exposed to any X-ray irradiation (control group) are completely undamaged. In this dataset the occupancy values of the positions of all hydrogen atoms are 1.000(1) except for H3 showing an occupancy value of 0.976(1). The occupancy of the position of H3 is also lower than 1.000 (0.894(2)) at 375 seconds. However, after 600 seconds and 1680 seconds the occupancy of the position of H3 is 1.000 (with a higher standard deviation of between 0.001 and 0.007). Therefore it can be assumed that the position of H3 is fully occupied and that the discrepancy for the two

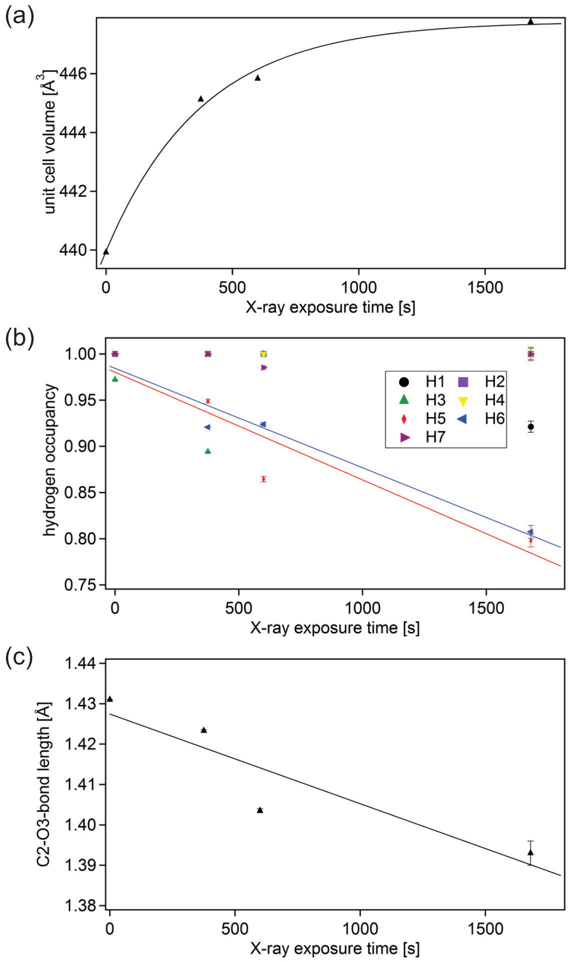

Figure 3.1: Unit cell volume increase of L-serine (a), occupancy change of the positions of all hydrogen atoms (b) and bond length change of the C2-O3-bond (c) as function of X-ray exposure time.

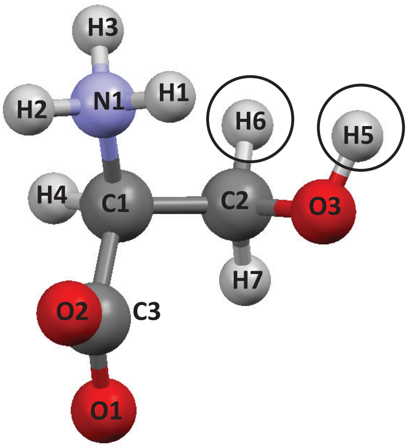

Figure 3.2: Labeling scheme for L-serine. The two hydrogen atoms showing a decrease in occupancy of their position are highlighted.

datasets originates from experimental errors.

In contrast to this, the positions of H5 and H6 display an occupancy of 1.000 for the unirradiated crystal. At 375 seconds of X-ray exposure both positions have decreased in occupancy significantly (0.95(2) for H5, 0.92(2) for H6). At 600 seconds of X-ray exposure the occupancy of the position of H5 has further decreased to 0.86(3) whereas that of the position of H6 stays constant at 0.92(2). For the maximum X-ray exposure time (1680 seconds) the position of H5 shows an occupancy of 0.80(8) and the one of H6 shows an occupancy of 0.81(7), which corresponds to a decrease in occupancy to around 80% for both crystals. After 1680 seconds X-ray exposure time, the position of H1 also shows a decrease in occupancy. ITDPs and occupancies can be found in tables A.33 to A.36 in section A.5.1 in the appendix.

Investigation of the bond lengths showed only one bond length contraction. Fig. 3.1 (c) shows the bond length change of this C2-O3-bond as function of X-ray exposure time. The bond length decreases from 1.430 Å to 1.393 Å.

The labeling scheme for L-serine with the two hydrogen atoms whose position show a decrease in occupancy can be seen in fig. 3.2.

3.2 L-alanine

Neutron diffraction data were collected from two previously X-ray irradiated crystals (X-ray irradiation times were 600 seconds and 3600 seconds, respectively) and the resulting occupancies of the positions of all hydrogen atoms were extracted from this measurement as described in 3.1. Table 3.1 shows the freely refined occupancies after 600 seconds of X-ray exposure time. All values remained at approximately 1.00(2) (except for the position of H7 which showed a slightly lower occupancy) for a ITDP around 0.2 Å^2.

Table 3.2 shows the freely refined occupancies after 3600 seconds. Here, a clear decrease in the occupancy of the positions for all three hydrogen atoms of the methyl group is visible. H5 decreases to 0.93(4), H6 decreases to 0.92(4) and H7 shows a decrease to 0.98(4).

Table 3.1: Occupancies and ITDPs of the positions of all 7 hydrogen atoms in the L-alanine molecule after 600 seconds of irradiation.

name	**occupancy**	**occupancy standard deviation**	**ITDP [Å^2]**
H1	1.00000	0.00200	0.02154
H2	1.00000	0.00200	0.02154
H3	1.00000	0.00200	0.02154
H4	1.00000	0.00200	0.02154
H5	1.00000	0.00200	0.02490
H6	1.00000	0.00200	0.02490
H7	0.99559	0.00200	0.02490

Fig. 3.3 shows the labeling scheme for L-alanine. The hydrogen atoms whose positions are decreasing in occupancy are highlighted.

3.3 Thymidine

Fig. 3.4 (a) shows the unit cell volume increase of thymidine as function of X-ray exposure time. The unit cell volume increases linearly with X-ray exposure time.

Table 3.2: Occupancies and ITDPs of the positions of all 7 hydrogen atoms in the L-alanine molecule after 3600 seconds of irradiation.

name	occupancy	occupancy standard deviation	ITDP [Å^2]
H1	1.00000	0.00400	0.01900
H2	1.00000	0.00400	0.01900
H3	1.00000	0.00400	0.01900
H4	1.00000	0.00400	0.01900
H5	0.92883	0.00400	0.02412
H6	0.91840	0.00400	0.02412
H7	0.97873	0.00400	0.02412

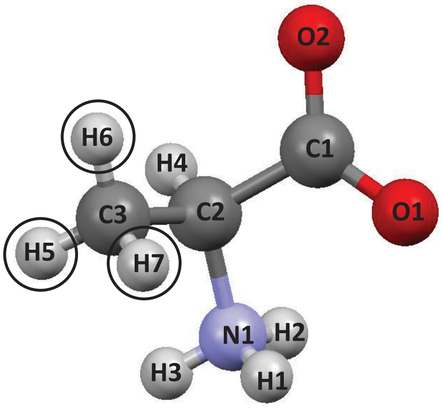

Figure 3.3: Labeling scheme for L-alanine. The three hydrogen atoms showing a decrease in occupancy of their position are highlighted.

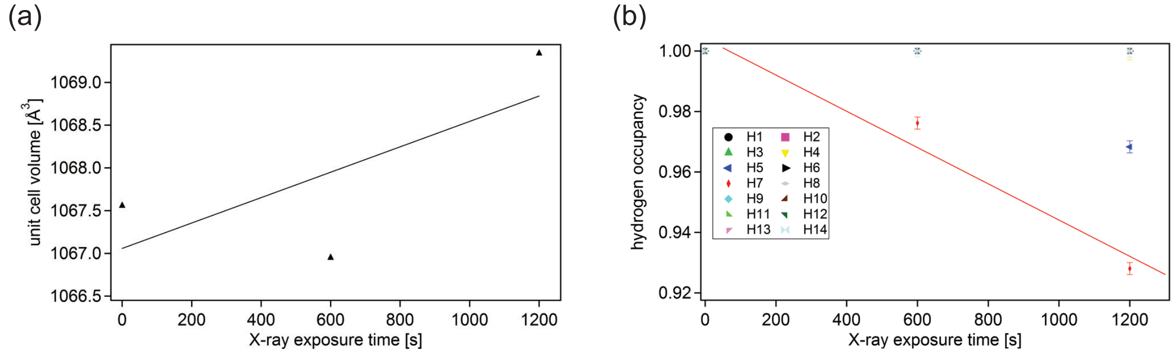

Figure 3.4: Unit cell volume increase of thymidine (a) and occupancy change of the positions of all hydrogen atoms extracted from neutron data (b) as function of X-ray exposure time.

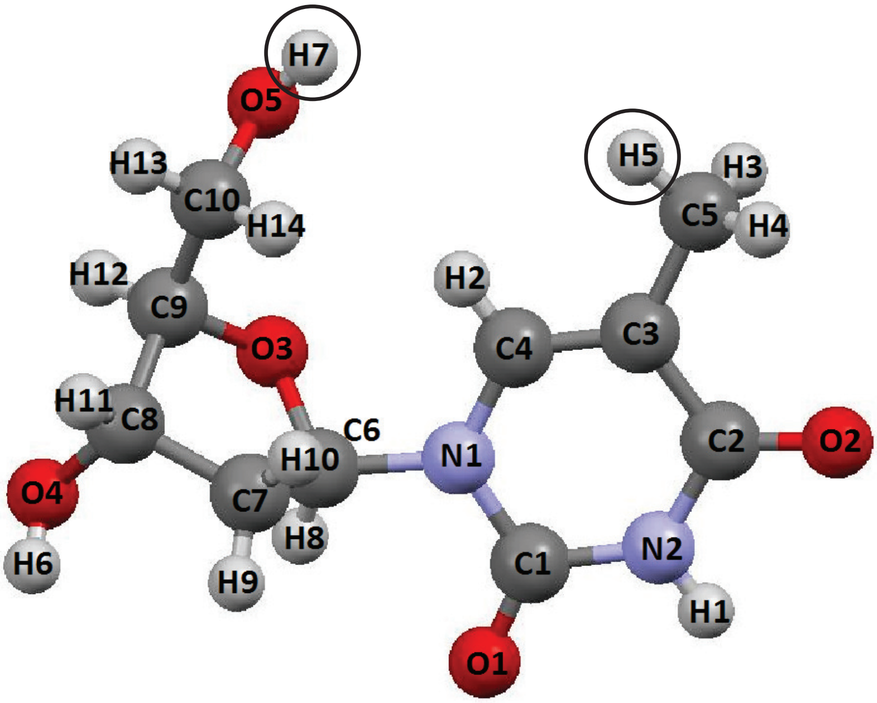

Figure 3.5: Labeling scheme for thymidine. The two hydrogen atoms showing a decrease in occupancy of their position are highlighted.

Fig. 3.4 (b) shows the freely refined occupancies of the positions of all hydrogen atoms as function of the X-ray exposure time. All values stay constant at 1.000, except for the position of H7 which continuously decreases to a final value of 0.93(2) after 1200 seconds of X-ray exposure time. The position of H5 also shows a decrease in occupancy to 0.97(2) after 1200 seconds. The remaining hydrogen atoms do not show such a behaviour. ITDPs and occupancies of the positions of all hydrogen atoms can be found in tables A.39 to A.41 in section A.5.3 in the appendix.

Fig. 3.5 shows the labeling scheme for thymidine. The two hydrogen atoms showing a decrease in occupancy of their position are highlighted.

V Discussion

1 Discussion

1.1 X-ray induced photoreduction

Oxidation state changes in metal organic complexes and metalloproteins have been widely discussed in the literature.[18,20,21,30–35] Knowledge about these processes is essential to understand many biological principles, such as oxygenic photosynthesis by photosystem I and photosystem II,[19,22,26] enzymatic reactions involving methionine synthase[51,116–119] or glutamate mutase[23,106,115,120–123] of protein-bound B12 cofactors, or Fe(III) transfer in the human body.[124,125]

Direct probing of the oxidation state by X-ray methods, such as X-ray Absorption Near Edge Spectroscopy (XANES), offers the possibility to gain further insight into biological principles. However, results from XANES measurements have to be treated with care, since X-rays themselves can often cause photoreduction of the metal centre within the sample.[26]

Metal ions, such as Co(III),[23] Fe(III),[29] Cu(II),[27] Ni(III)[24,25] or manganese in higher oxidation states[19] are well known for their susceptibility to X-ray induced photoreduction. Thus, X-ray induced changes in the oxidation state of compounds containing these metal centres are highly probable and can often lead to misinterpretations of biological principles.[22] Although X-ray induced photoreduction is an important factor in the investigation of metal organic complexes, no conclusive mechanism could be found so far.

In this work, a systematic study of X-ray induced photoreduction of cyanocobalamin and four iron-complexes (ammonium ferric citrate and potassium hexacyanoferrate, both containing Fe(III), as well as pyrite and diiron-dithiolate, both containing Fe(II)) were performed (see fig. 2.1, chapter 2 of the ***"Experimental"*** section). Influential factors, such as temperature, solvent content and chemical composition of the samples were investigated.

X-ray induced photoreduction could be observed for cyanocobalamin and ammonium ferric citrate. In both cases photoreduction took place in the presence and absence of solvent. Interestingly, no photoreduction was observed for potassium hexacyanoferrate, which also contains a photosensitive Fe(III) centre.

1.1.1 Temperature dependence

Cyanocobalamin was measured in dose series at temperatures between 5 and 300 K (see section 2.2.2 in ***"Results"***). Normalisation of the spectra was performed and the value E_0, at which the normalised absorption coefficient $x\mu_{norm}$ reaches 50%, was extracted for each spectrum of a dose series. E_0 was then plotted as function of dose to follow the shift of the absorption edge and, thus, the oxidation state of the sample (see section 2.1 in ***"Results"***). Fitting the value by an exponential function revealed a significant temperature dependence of X-ray induced photoreduction above 100 K. Photoreduction was reduced by a factor of three to four for experiments carried out at 100 K instead of 250 K for solid and aqueous samples, respectively (see fig. 2.2, section 2.1 in ***"Results"***). Such a temperature dependence of photoreduction is well known for other metal organic complexes, including metalloproteins.[21,27]

Cooling below 100 K did not lead to any further suppression of photoreduction. The exponential shift factors applied to the course of E_0 were comparable at all temperatures between 5 K and 100 K (see fig. 2.3 (c), section 2.1 in ***"Results"***).

Assuming direct photoreduction of Co(III) by low energy electrons generated upon X-ray irradiation,[8] photoreduction should be independent of temperature, which is not the case. Additionally, photoreduction should take place for all B12 cofactors which contain a Co(III) centre. However, measurements of Champloy *et al.*[23] contradict this implication. In these measurements methylcobalamin was investigated before and after irradiation with X-rays using XANES. No photoreduction was found for methylcobalamin, while cyanocobalamin was photoreduced. L-edge XANES measurements on methyl- and cyanocobalamin (see fig. A.24, section A.7 in the appendix) were performed to countercheck these results. L-edge XANES measurements supported the observation that methylcobalamin is either not or much slower photoreduced compared to cyanocobalamin.

It has been reported that excitation of cyanocobalamin with UV/VIS light leads to an excitation to a short-lived state with a reduced Co(II)* centre. Here the excited state is assumed to be a ligand-metal charge transfer (LMCT) state.[126] In contrast to this, the intermediate state upon excitation of methylcobalamin with UV/VIS light was characterised as a metal-ligand charge transfer (MLCT) state.[127,128] In this case, the majority of the excited Co(II)* centres will reportedly fall back into the ground state.[128] This means that the excited states for both B12 cofactors are different. Following this line of argument, one can conclude that similar short-lived excited states occur for both B12 cofactors for X-ray excitation. In this case, the excited state is obtained by low energy electron attachment.[129–133] It is assumed that the Co(III) centre in methylcobalamin is not photoreduced upon excitation with UV/VIS light due to the nature of the excited state,[126–128] whereas the nature of the excited state of cyanocobalamin allows a photoreduction to take place. A possible reason for this different behaviour might be the position of the upper axial ligand in the spectrochemical series[134–137] which causes a significantly different ligand field[138] around the Co(III) centre for both cofactors.

Investigation of cyanocobalamin showed that approximately 700 metal centres were photoreduced per absorbed photon*. This supports the aforementioned hypothesis that X-ray induced photoreduction cannot be a primary event. Cyanocobalamin was photoreduced in solid form as well as in aqueous solution. Photoreduction takes place independent of the

---

*This estimation was made for the 100 K dataset of solid cyanocobalamin, assuming that the exponential law describes the statistical distribution between Co(III) and Co(II). In order to estimate the amount of centres reduced per photon, the amount of photons absorbed by the sample for the fully reduced species were calculated. Furthermore the amount of molecules within the beam was determined while keeping the ratio of boron nitride and cyancobalamin in mind.

sample environment. This indicates that the oxidation reaction has to take place within the ligand. Abstraction of a hydrogen atom from a certain position within the ligand could be a possible oxidation process[48] (k_2 in fig. 1.1). With hydrogen gas as a leaving group the process is irreversible, therefore leading to an irreversible photoreduction of the compound.

The observed temperature dependence of the photoreduction of cyanocobalamin can also be explained by this process. Hydrogen abstraction is a temperature dependent process.[37, 139–141] Higher temperatures cause a stronger thermal movement of the atoms within the molecule and a higher mobility of the hydrogen atoms. Thus, the probability for the hydrogen atom to overcome the binding energy barrier and to be abstracted is much higher. Consequently, the abstraction takes place faster. Therefore, a temperature dependence is observed even if a direct interaction of the low energy electrons with the metal centre is taking place.

Such a hydrogen abstraction could be observed in X-ray diffraction measurements on single crystals of cyanocobalamin, where an increase in the ITDP of a specific hydrogen atom (H9), located at the primary hydroxyl group (CH_2-OH) of the ribose moiety, could be observed (see figs. 1.4 and 1.5, section 1.1 in ***"Results"***). A similar process could not be detected for methylcobalamin. This implies that abstraction of one specific hydrogen atom is taking place only in case of cyanocobalamin, which is photoreduced upon irradiation with X-rays. This hydrogen abstraction might be related to the photoreduction process.

Enzyme binding of B12 cofactors is of huge interest in biology. During these binding processes, bond elongations between the Co(III) centre and the upper and lower axial ligand were observed. It has been proposed in the literature that such bond elongations might be a consequence of the reduction of the metal centre from Co(III) to Co(II) upon enzyme binding.[113–115] Investigations have been performed whether these bond elongations are an artifact resulting from global X-ray radiation damage.[23] In this work, bond elongations between both axial ligands and the metal centre for B12 cofactors which are not bound to an enzyme could also be observed as a result of X-ray irradiation using single crystal X-ray diffraction. Bond elongations could be observed for cyano- as well as methylcobalamin (see fig. 1.2, section 1.1 in ***"Results"***). Given that methylcobalamin is not or only slightly photoreduced with dose, the bond elongations are most probably not originating from an X-ray induced photoreduction. Nonetheless, it can be concluded that they are a consequence of X-ray radiation damage. The observed bond elongations will therefore be further discussed in section 1.3.

Combining the observations from X-ray diffraction and absorption measurements, a model for the photoreduction process is proposed. Fig. 1.1 shows an illustration of the proposed mechanism. In this model, a low energy electron generated upon X-ray irradiation is attached to the metal centre. This results in a short-lived excited state with a reduced Co(II)* centre. This reaction takes place with a rate constant k_1. After the excitation, the metal centre can either react back to its initial state (methylcobalamin) if no oxidation reaction is induced (k_{-1}) or remain in a reduced state (cyanocobalamin) if an oxidation reaction of the ligand can be induced (k_2).

XANES measurements of ammonium ferric citrate, conducted at 100 K and 300 K, revealed that ammonium ferric citrate is also reduced at high doses of X-ray radiation (see section 2.2.1 in ***"Results"***). Approximately 150 metal centres were reduced by one incident photon[†]. In contrast to cyanocobalamin, no temperature dependence could be observed for ammonium ferric citrate, which indicates that a different photoreduction mechanism is taking place here.

Ammonium ferric citrate is well known to undergo photoreduction already upon irradiation with UV and blue light.[65] In this reaction, the citrate is first decomposed to acetonedicarboxylic acid, liberating carbon dioxide. The compound then further decomposes until it is stabilised.[66,67] Based on the results of this work, a similar mechanism is proposed for X-ray induced photoreduction of ammonium ferric citrate. As an initial step, a low energy electron attaches to the Fe(III) centre, yielding a short-lived excited state with a Fe(II)* centre (k_1). The electron then remains attached to the metal centre

---

[†] Estimation of this number was made similar to cyanocobalamin with the attenuation of the beam taken into account.

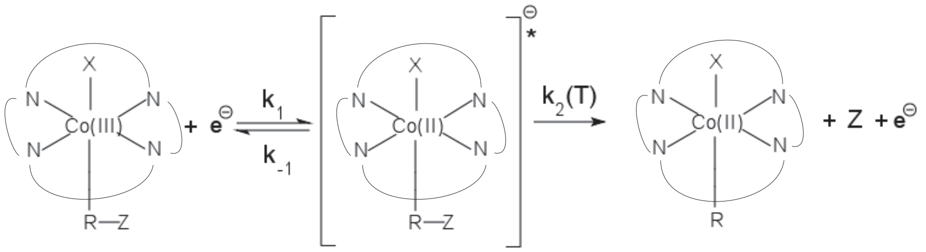

Figure 1.1: Proposed mechanism of X-ray induced photoreduction in B12 cofactors: the corrin ring around the metal center is shown schematically. X is representing the upper axial ligand, which defines the cofactor (e.g. X=CH_3 for methylcobalamin, X=CN for cyanocobalamin). R-Z and R are representing the lower axial ligand before and after oxidation, respectively. In an initial step, a low energy electron is attached to the Co(III) centre. This leads to a short-lived Co(II)* centre (k_1). The second step determines whether a photoreduction occurs: If the nature of the ligands does not allow and oxidation reaction within the ligands, the low energy electron will detach from the metal centre. This leads to a Co(III) centre (k_{-1}). If an oxidation reaction is possible, the low energy electron remains attached to the Co(II) centre. The process is made irreversible by the group Z leaving the compound (k_2). One possible oxidation reaction might be X-ray induced hydrogen abstraction with hydrogen gas as leaving group.

while the ligand is oxidised via an inelastic process (k_2). A possible oxidation reaction could be a decarboxylation of the citrate releasing carbon dioxide.[142–145] With carbon dioxide as leaving group, this is an irreversible reaction. Decarboxylation reactions are also well known to take place upon X-ray irradiation of biological samples[16] and occur already at much lower doses than classical dose limits[146] - even at cryogenic temperatures. It has been proposed that the mechanism of decarboxylation proceeds via electron hole transfer to a carboxyl group.[14] This leads to the formation of carbon dioxide. Thus, X-ray induced photoreduction of ferric ammonium citrate seems to proceed via a temperature independent decarboxylation reaction. A possible reduction mechanism, involving a decarboxylation reaction is shown in fig. 1.2.

Interestingly, no photoreduction was observed for potassium hexacyanoferrate, also containing Fe(III). At 100 K and 300 K no spectral changes could be observed at all (see fig. 2.5, section 2.2.2 in ***"Results"***). The observation that potassium hexacyanoferrate is not photoreduced by X-rays has been made before.[69] Given that the ligand of the Fe(III)

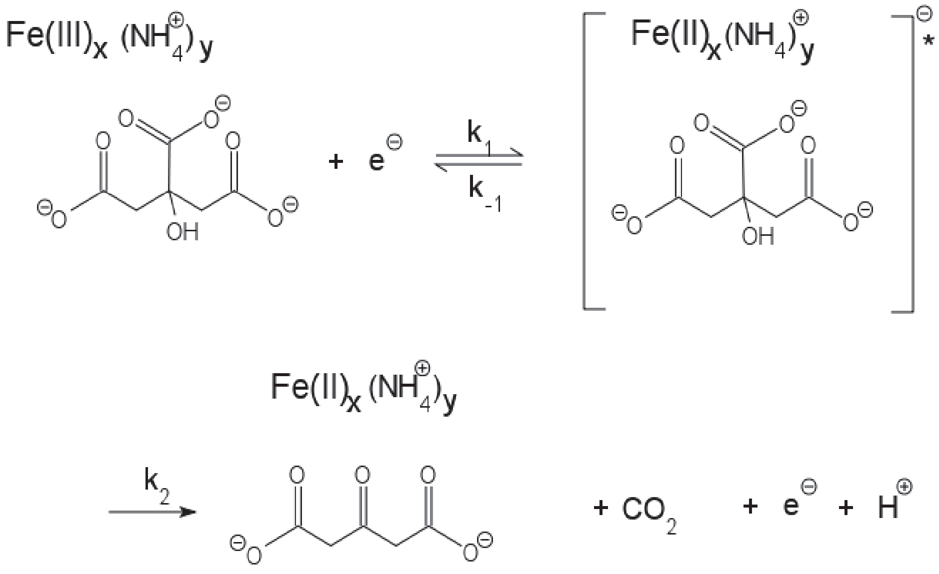

Figure 1.2: Proposed mechanism of the X-ray induced photoreduction in ammonium ferric citrate: As an initial step, a low energy electron is attached to the metal centre, leading to a short-lived excited state with a reduced Fe(II)* centre (k_1). In case of ammonium ferric citrate the following process is then dominated by k_2: The electron remains attached to the centre while the ligand is oxidised (k_2). A possible oxidation reaction is a decarboxylation of the citrate, leading to acetonedicarboxylic acid with carbon dioxide as leaving group. Such a reaction has been proposed for the photoreduction of ammonium ferric citrate by UV light.[66, 67]

centre is cyanide, this is most probably not due to the nature of the ligand field around the metal centre. It either means that no low energy electron attachment to the metal centre takes place or that the ligand cannot be oxidised. In both cases no irreversible photoreduction can take place.

Pyrite and diiron-dithiolate were also measured at 100 K and 300 K. Since they already contained Fe(II), no photoreduction was expected. For pyrite, no radiation induced changes could be observed in the XANES spectra for both temperatures (see fig. 2.6, section 2.2.3 in ***"Results"***). In case of diiron-dithiolate, a clearly different behaviour could be observed for both temperatures (see fig. 2.7, section 2.2.4 in ***"Results"***). This behaviour did not imply a photoreduction, but a different damage process which will be discussed in section 1.3.1 of this chapter.

1.1.2 Solvent dependence

It has been proposed in the literature that the presence of solvent in the sample increases the susceptibility of a compound to X-ray induced photoreduction and X-ray radiation damage in general.[16,31] The radicals in the solvent are supposed to accelerate the damage process within the sample.

First investigations indicated that X-ray induced photoreduction might not take place in the absence of a solvent, since this reaction was suspected to be a result of X-ray induced water photolysis which led to free electrons that could propagate through the sample, even at cryogenic temperatures.[31]

XANES measurements revealed that the influence of water on the susceptibility to X-ray induced photoreduction of cyanocobalamin is very small or even not present at temperatures below 250 K (see fig. 2.2, section 2.1 in ***"Results"***). Cyanocobalamin is photoreduced independent of the presence or absence of water. At 100 K, the susceptibility of anhydrous cyanocobalamin and an aqueous cyanocobalamin solution to X-ray induced photoreduction is the same. At 250 K, the aqueous solution shows a higher susceptibility of 24%, as defined by the exponential coefficient from fitting of the E_0 values, to X-ray induced photoreduction compared to the anhydrous sample. The increased susceptibility to photoreduction in presence of water at higher temperatures might be explained by additional radical formation in the solvent and a higher radical mobility at higher temperatures.[16,147]

In contrast to the findings for cyanocobalamin, ammonium ferric citrate shows a clear solvent dependence (see fig. 2.4, section 2.2.1 in ***"Results"***). Dissolution in water reduces the susceptibility to photoreduction of ammonium ferric citrate by a factor of two.

Assuming that a decarboxylation reaction within the ligand causes the photoreduction of ammonium ferric citrate (see fig. 1.2), the release of carbon dioxide could be hampered by the surrounding ice matrix. The generated carbon dioxide gas is trapped by the ice matrix and induces pressure in the sample. This would change the chemical equilibrium between the unreduced and the reduced state in the direction of the unreduced species and thus decrease the susceptibility to X-ray induced photoreduction (Le Chatelier's principle[148]).

A similar observation was made in the field of explosives, where X-ray induced decomposition of these compounds causes a gas release. Here, it was found that X-ray induced decomposition can be significantly slowed down by application of high pressures,[149] since high pressures prevent the gas release and therefore shift the equilibrium of the system in direction of the educt.

1.1.3 Influence of chemical composition

X-ray diffraction as well as K-edge and L-edge XANES measurements of cyano- and methylcobalamin have shown that X-ray induced photoreduction does not only depend on the metal centre, but also on the ligand of the complex. Both compounds only differ in their upper axial ligand (methyl and cyanide, respectively). The fact that cyanocobalamin is photoreduced, whereas methylcobalamin is not, is a first implication that X-ray induced photoreduction is depending on the ligand. This theory is supported by the fact

that potassium hexacyanoferrate is not photoreduced even at a dose of 25 MGy while ammonium ferric citrate, which also contains Fe(III), is photoreduced. This further supports the hypothesis that photoreduction only takes place if the ligand is oxidised. Since photoreduction occurs independent of the state of the sample (solid or aqueous), this oxidation reaction must take place within the molecule itself. Ligand dependence of the photoreduction process has been addressed in the literature.[69, 145]
Measurements on pyrite and diiron-dithiolate also showed a different damage behaviour, albeit both containing Fe(II) (see sections 2.2.3 and 2.2.4 in ***"Results"***). Pyrite remained unaffected at high doses of X-ray radiation at 100 K and 300 K while diiron-dithiolate did not show any spectral changes at 100 K, but significant changes in the white line at 300 K. Since they both contain Fe(II) (see fig. 2.1, section 2.2 in the ***"Experimental"*** section), this different behaviour originates from a difference in their chemical composition. Taking into account the results for cyano- and methylcobalamin and the role of hydrogen abstraction in the X-ray induced photoreduction of cyanocobalamin, the abstraction of hydrogen atoms might play a role in case of the diiron-dithiolate as well. The influence of hydrogen abstraction on global and specific damage processes will be discussed in sections 1.2 and 1.3.3 of this chapter.

1.1.4 Proposed mechanism for X-ray induced photoreduction in metal organic complexes

Based on the results of this work, a general model for X-ray induced photoreduction in metal organic complexes is proposed. Measurements indicate that X-ray induced photoreduction is part of a redox reaction within the molecule. The surrounding solvent does not participate in this reaction. It is suggested that the photoreduction process in metal organic complexes consists of two subsequent reactions which are taking place.

Fig. 1.3 shows a schematic illustration of the proposed mechanism of X-ray induced photoreduction in a metal organic complex consisting of a metal centre M^{n*} and the lig-

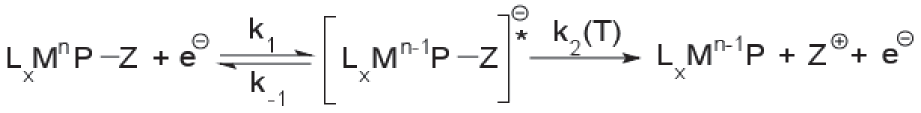

Figure 1.3: Proposed mechanism for X-ray induced photoreduction of metal organic complexes: The initial metal complex consisting of the metal centre M^n in oxidation state n is coordinated by the x ligands L, where all ligands can be different, and at least one ligand P-Z. In the initial step, a low energy electron generated in the sample upon X-ray irradiation is attached to the metal centre, yielding a short-lived excited state with a reduced metal centre $M^{n-1}*$. This reaction occurs with rate constant (k_1). Depending on the nature of the ligand, the following step either leads to an unreduced species M^n (k_{-1}), where the electron is released again without oxidation of the ligands, or a reaction to a reduced species M^{n-1} ($k_2(T)$) if an oxidation reaction is induced in the ligand P-Z yielding ligand P after release of leaving group Z. Charge conservation is guaranteed by the release of an electron. The rate constant $k_2(T)$ determines the temperature dependence of the photoreduction process.

ands L_x, which can all be different, and at least one ligand P-Z. The incident low energy electron interacts with the metal centre in oxidation state (n). This leads to a short-lived excited state with a reduced metal centre $M^{n-1}*$ (k_1). Permanent photoreduction will only occur if the nature of the excited state allows to induce an oxidation reaction of the ligand. If this is not the case, the electron will detach from the metal centre with a rate constant k_{-1}, leading to the unreduced species in the ground state. In case of an oxidation reaction with rate constant k_2(T), the low energy electron remains at the metal centre. This process is made irreversible by a group Z that is leaving the compound. Charge conservation of the system is guaranteed by the release of an electron from the ligands. The interaction of the low energy electrons with the metal centre is always temperature independent, however, the second reaction step can either be temperature dependent or not.

It has to be mentioned that this proposed mechanism still has to be verified. Further investigations using femtosecond spectroscopy could further clarify how an excitation by interaction with the low energy electrons takes place.

1.2 Hydrogen abstraction

Hydrogen abstraction has been proposed as a consequence of exposure of a sample to ionising radiation.[150–154] The connection between the abstraction of hydrogen atoms from specific sites of the molecule and radiation damage to a sample has only recently been made.[37,47] The formation of bubbles of gaseous radiation products in DNA as result of electron irradiation has recently been reported.[70] This work further supports the idea that the abstraction of hydrogen atoms plays an important role in many processes leading to radiation induced changes in a sample.

In electron paramagnetic resonance (EPR) studies on DL-serine the abstraction of a hydrogen atom from the hydroxyl group of the sample has been proposed as a consequence of X-ray irradiation.[155] Upon irradiation, the bond between the oxygen and hydrogen atom of the hydroxyl group was cleaved homolytically, which led to the a hydrogen radical and an alkoxy radical, and, thus, to an EPR-signal of the otherwise EPR silent compound DL-Serine.

Unfortunately, hydrogen atoms are only poorly visible in X-ray diffraction measurements. In order to directly observe hydrogen abstraction, it is therefore necessary to engage other analytical methods, such as single crystal EPR, neutron diffraction or Raman spectroscopy. This work used a combined X-ray and neutron diffraction study to systematically investigate the hypothesis of hydrogen abstraction as an important contributor to global and specific radiation damage.

Crystals of the two amino acids L-serine and L-alanine, as well as the nucleoside thymidine (see fig. 1.4) have been investigated using X-ray as well as neutron diffraction. The crystals were X-ray irradiated beforehand in order to investigate different X-ray irradiation states of the samples with neutron diffraction (see section 3.1 in ***"Experimental"***). X-ray diffraction dose series revealed a different susceptibility to radiation damage for all three compounds. L-serine was the most susceptible, thymidine was less affected than L-serine but more than L-alanine, which was very radiation hard (see fig. 1.9, section 1.2.1, table 1.12, section 1.2.2 and fig. 1.16, section 1.2.4 in ***"Results"***). Structure refinement

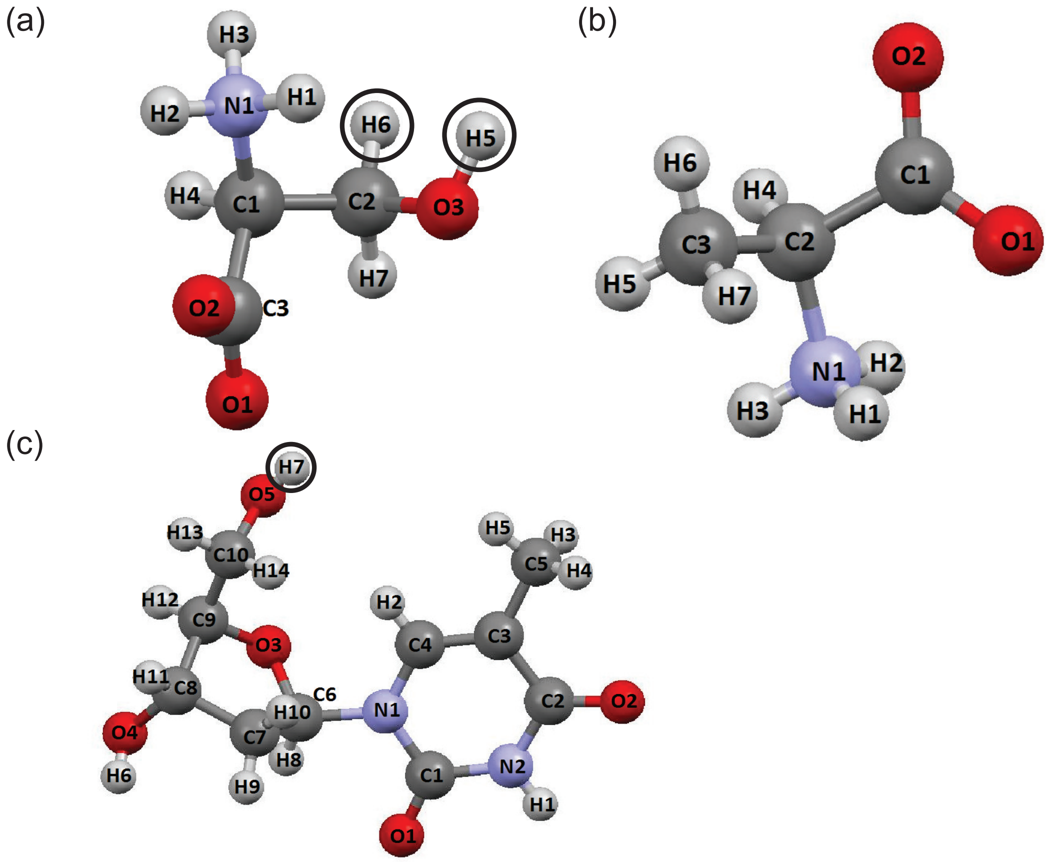

Figure 1.4: Labeling scheme of L-serine (a), L-alanine (b) and thymidine (c). The abstracted hydrogen atoms are marked.

of the L-serine and thymidine X-ray data showed increased ITDPs of specific hydrogen atoms, located at primary hydroxyl groups (see figs. 1.11, section 1.2.1 and 1.19, section 1.2.4 in ***"Results"***). In case of thymidine an ITDP increase of the hydrogen atom at a secondary hydroxyl group (CH-OH group) could be observed, but it was less pronounced than the ITDP increase of the hydrogen atom at the primary hydroxyl group. These observations were in good agreement with the findings from cyanocobalamin, where an increased ITDP was observed for the hydrogen atom at the primary hydroxyl group of the ribose moiety as well. Increased ITDPs are a result of localised changes in the occupancy of the position of a certain atom. These changes can either be caused by disorder or radiation induced displacements of specific atoms. It is therefore assumed that hydrogen abstraction might take place.

In order to be more sensitive to the occupancies of the positions of all hydrogen atoms, neutron diffraction experiments were carried out. Neutron diffraction data of L-serine showed a site-specific hydrogen abstraction for high doses of X-ray radiation. A decrease in the occupancy of the positions of two hydrogen atoms (namely H5 and H6) from the molecule was observed. This abstraction was accompanied by an X-ray radiation induced bond contraction of the C2-O3-bond. The initial bond length for zero dose is 1.430 Å and is reduced upon X-ray irradiation to 1.393 Å at maximum dose (see fig. 3.1, section 3.1 in ***"Results"***). This bond length implies that the ratio between single and double bond is 80% to 20%. X-ray diffraction experiments also gave a C2-O3-bond length between a single (1.430 Å) C-O-bond and a double (1.200 Å) C=O-bond.

Independent analysis of the occupancies of the positions of H5 and H6 obtained from neutron diffraction experiments showed that for the final dataset 20% of these two atoms have been abstracted. This is in good agreement with the observed bond length change. At lower doses the differences in the occupancies of the positions of H5 and H6 are more pronounced. The occupancy of the position of hydrogen atom H5 seems to decrease faster than the occupancy of the position of hydrogen atom H6. It is therefore proposed that the radiation-induced changes at L-serine involve the attachment of a low energy electron to the primary hydroxyl group. This leads to a cleavage of the O3-H5-bond and a L-serine

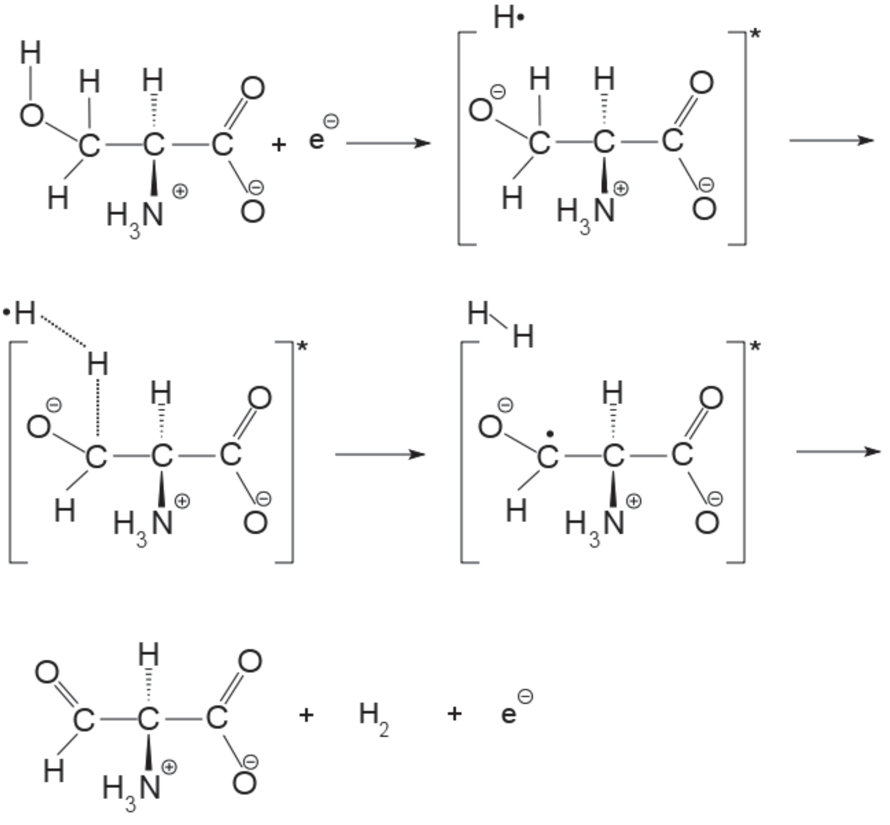

Figure 1.5: Proposed mechanism for X-ray radiation damage in L-serine: Upon irradiation a low energy electron is attached to the primary hydroxyl group, leading to the abstraction of the hydrogen atom from this group. This abstraction leads to a second hydrogen abstraction from the adjacent methylene group, resulting in the formation of hydrogen gas and a carbonyl group. During this step, the electron is released from the molecule.

molecule in an excited state. The abstracted hydrogen then leads to the abstraction of a second hydrogen atom from the the adjacent methylene group (H6), probably due to its spatial proximity to H5 (2.11 Å) and to the favourable torsion angle with respect to the hydroxyl group (28.99° for H6-C2-O3-H5 and 147.08° for H7-C2-O3-H5). This results in hydrogen gas release and the formation of a double bond between the oxygen (O3) and the carbon (C2) atom. During this step, the low energy electron is ejected from the molecule (see fig. 1.4 (a) for labeling and fig. 1.5 for the mechanism). The normalised C2-O3-bond lengths from X-ray and neutron diffraction were used for a rough dose estimation of the

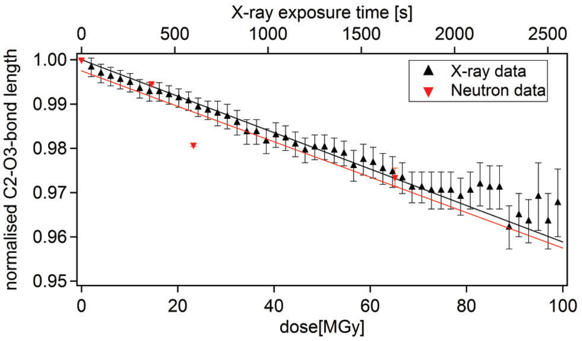

Figure 1.6: Normalised bond length of the C2-O3-bond obtained from single crystal X-ray (black) and neutron (red) diffraction. This normalised bond length change was used for a rough dose estimation.

X-ray irradiated crystals measured with neutrons (see fig. 1.6). According to this estimation the dose per second delivered to the L-serine crystals was approximately 36.9 kGy, resulting in a dose of 62.0 MGy for the crystal irradiated for 1680 seconds.

Neutron measurements on two L-alanine crystals, which were X-ray irradiated for 600 and 3600 seconds, respectively, were in agreement with the findings from X-ray data. L-alanine can withstand larger amounts of X-ray radiation compared to L-serine. In contrast to L-serine, no hydrogen abstraction could be observed after 600 seconds of X-ray irradiation. After 3600 seconds, hydrogen abstraction of all three hydrogen atoms from the methyl group could be detected (see table 3.2, section 3.2 in ***"Results"***). This further indicates that a compound not containing a hydroxyl group is radiation harder and does not suffer significantly from specific damage.

Neutron diffraction on single crystals of thymidine, which were X-ray irradiated for 0, 600 and 1200 seconds, revealed an occupancy decrease of the positions of two hydrogen atoms (see fig. 3.4, section 3.3 in ***"Results"***). The occupancy during the full series of measurements decreased from 1.00(2) to 0.92(2) for the position of H7, meaning only 8% of the hydrogen atoms were affected after 1200 seconds of irradiation. The position of the second hydrogen atom, H5, did not show any decrease until the very last dataset (from 1.00(2) to 0.96(2)). This implies that the primary effect takes place at the position of H7. H5 might be abstracted in a secondary step at higher doses. Interestingly, the primary

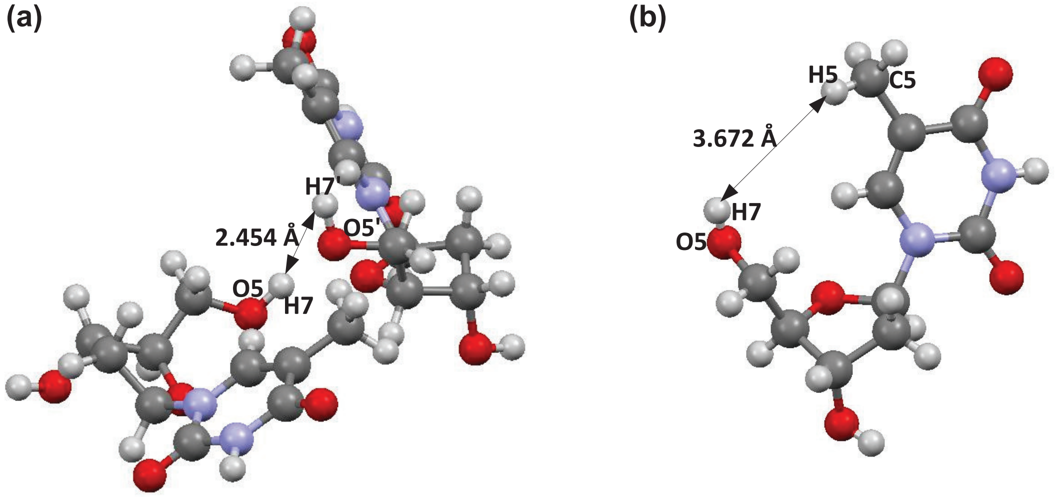

Figure 1.7: Hydrogen - hydrogen distance of the hydrogen atoms belonging to two primary hydroxyl groups of two adjacent thymidine molecules(a) and two hydrogen atoms belonging to the primary hydroxyl and the methyl group of the same thymidine molecule (b).

abstraction could be observed from a primary hydroxyl group, similar to L-serine. In contrast to L-serine, no second hydrogen atom was abstracted from the adjacent methylene group. This is most probably a results of the larger torsion angle between the hydroxyl and the adjacent methylene group in the thymidine molecule (80.95° for H13-C10-O5-H7 and -38.34° for H14-C10-O5-H7 in thymidine compared to 28.99° for C2-H6-O3-H5 and 147.08° for C2-H7-O3-H5 in case of L-serine) and the distance between the hydrogen atoms in this group (2.23 Å for thymidine, compared to 2.11 Å in case of L-serine). Furthermore, in contrast to the X-ray data, no decrease in occupancy of the position of the hydrogen atom at the secondary hydroxyl group could be observed.

Investigation of the hydrogen - hydrogen distances within the thymidine crystal structure revealed a hydrogen bond between two primary hydroxyl groups of two adjacent thymidine molecules. This hydrogen bonds results in a distance of 2.45 Å between the hydrogen atoms belonging to these primary hydroxyl (fig. 1.7 (a)). It has been proposed that hydrogen abstraction as a radical process is feasible for a distance of 2.70 Å.[156] Hence, it is possible that one hydrogen atom is abstracted from a primary hydroxyl group and then leads to the abstraction of a second hydrogen atom from an adjacent primary hydroxyl

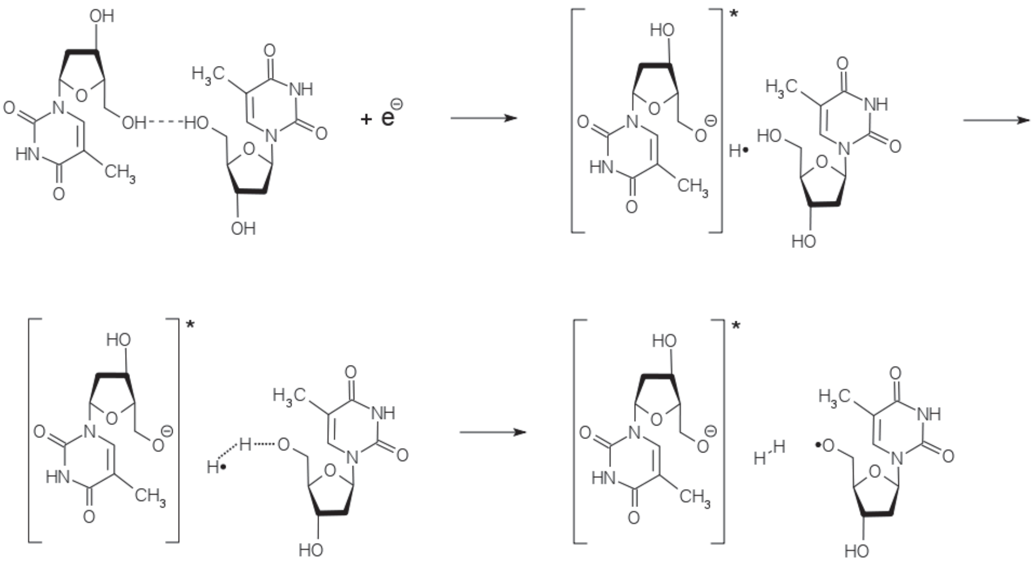

Figure 1.8: Proposed damage mechanism of thymidine: By attachment of a low energy electron a hydrogen atom is abstracted from the primary hydroxyl group. This leads to a thymidine molecule in an excited state and a hydrogen radical. This radical can then abstract a second hydrogen atom from the primary hydroxyl group of the adjacent molecule. This leads to the generation of hydrogen gas, a thymidine radical and a thymidine anion in an excited state. The last reaction step cannot be determined from the data of this work.

group to form hydrogen gas. The proposed mechanism for this would involve the attachment of a low energy electron to the primary hydroxyl group of the thymidine molecule, leading to an excited state and a cleavage of the H7-O5-bond. The abstracted hydrogen radical would then abstract a second hydrogen radical from an adjacent primary hydroxyl group, thereby generating hydrogen gas, leaving a thymidine radical and an thymidine molecule in an excited state (see fig. 1.8). The further reaction cannot be determined from this data.

An intramolecular abstraction of a second hydrogen atom from the methyl group within the same thymidine molecule is also possible but far more unlikely due to the larger distance between these two hydrogen atoms (3.672 Å for H5-H7 compared to 2.454 Å for H7-H7', see fig. 1.7 (b)).

Since only one hydrogen atom was abstracted from one site of the compound, no double bond is formed and hence no bond length changes were observed for the C-O-bond. This is in good agreement with the results from X-ray diffraction.

It is assumed that the hydrogen atom (H7) is homolytically cleaved from the oxygen atom. This hydrogen atom might abstract the second hydrogen atom (H7') to form hydrogen gas which cannot be released easily from the crystal at low temperatures due to the surrounding ice matrix.

Based on these findings, it is proposed that X-ray induced damage originates from a site-specific hydrogen abstraction, preferentially from a primary hydroxyl group.

1.3 Global radiation damage

The influence of temperature as well as the contribution of X-ray induced photoreduction and site-specific hydrogen abstraction to global radiation damage was investigated by X-ray diffraction. (Normalised) mean intensity, correlation between the first and the subsequent datasets, mosaicity, relative B-factor, unit cell volume and R1 value from structure refinement were evaluated and compared.

It was shown that in the case of B12 cofactors temperature is an important factor, probably due to the higher mobility of the formed radicals and hydrogen gas.[37,147]

Furthermore, it could be found that specific damage processes such as X-ray induced photoreduction or site-specific hydrogen abstraction are the main contributors to the global damage process. Additionally, our measurements have shown that only a small proportion of the molecules within a crystal is photochemically changed before the crystal lattice starts to deteriorate. This leads to the conclusion that the main part of the crystal lattice remains in its initial state. In the graphical description of global radiation damage, the crystal lattice can hence be seen as a factor that is changing instead of being rearranged due to molecular changes. Therefore, the crystal lattice changes themselves might lead to molecular changes, such as bond elongations.

Our measurements led to the conclusion that global damage is a result of specific damage:

First specific changes take place, which then result in unspecific processes, such as unit cell expansion and an increase in mosaicity, causing a loss in crystalline order and diffraction power. A compound possessing only little site-specific changes is also less susceptible to global damage compared to one that shows more site-specific changes.

1.3.1 Temperature dependence

X-ray diffraction measurements of single crystals of cyanocobalamin at 100 K and 200 K showed a clear temperature dependence of global radiation damage (see section 1.1.1 in ***"Results"***). The decay of the mean intensity occurred much faster at 200 K, indicating that the crystal was damaged faster. Correlation coefficient, relative B-factor and R1 value from structure refinement further supported this observation. Comparison of the results for both temperatures shows a nearly constant unit cell volume for the whole dose series at 200 K, whereas at 100 K the unit cell volume is constantly increasing. In contrast to this, the mosaicity is increasing at 200 K, but remains approximately constant at 100 K. This indicates that either a unit cell expansion can be observed or an increase in mosaicity. This also is in agreement with the findings from the 100 K data of methylcobalamin (see section 1.3.2 in ***"Results"***).

Investigation of the three cell axis at both temperatures showed a significant difference for the a- and b-axis (see fig. 1.8, section 1.1.1 in ***"Results"***). At 100 K the a-axis remained more or less constant and the b-axis contracted slightly with dose. At 200 K an elongation of the a-axis could also be observed as well as a contraction of the b-axis. The elongation of the c-axis, however, is only slightly different at both temperatures. Interestingly, the Co-C- and Co-N-bonds (upper and lower axial ligand) of the B12 cofactors are aligned along this c-axis for both, cyano- and methylcobalamin. As stated before, X-ray and neutron diffraction measurements of irradiated L-serine and thymidine crystals have shown that global damage to a crystal involves site-specific changes to only a minority of molecules within a crystal before unspecific damage takes place. This effect leads to a

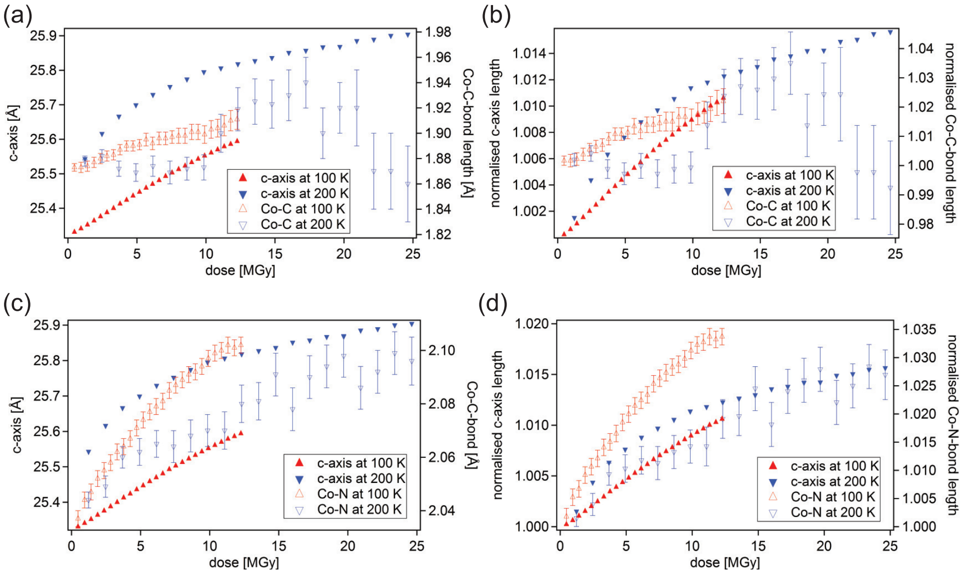

Figure 1.9: C-axis and Co-C-bond (a), normalised c-axis length and normalised Co-C-bond length (b), c-axis and Co-N-bond (c), normalised c-axis and normalised Co-N-bond length (d) of cyanocobalamin as function of dose for both, 100 K and 200 K.

complete deterioration of the crystal lattice (see fig. A.14 in the appendix). Hence, one can argue that the crystal lattice itself does not rearrange, but changes slightly due to the chemical changes within the molecules. It can be assumed that this process is applicable also for larger compounds, such as B12 cofactors. Therefore, one can assume that a unit cell expansion and axis elongation takes place in a given crystal lattice. A possible explanation for the bond elongations might then be given by the fact that the unit cell expansion mainly takes place along the c-axis. The bond elongations might be resulting from the axis elongation and, thus, from global radiation damage.

Fig. 1.9 (a) shows the c-axis (left) and Co-C-bond (right) as function of dose for 100 K and 200 K, respectively. The normalised values are shown in fig. 1.9 (b). The Co-N-bond and the c-axis as function of dose are shown in fig. 1.9 (c) and the normalised values are shown in fig. 1.9 (d). The Co-C-bond is not following a clear course at 200 K, so no definite conclusions can be deduced from these results. The slope for the Co-N-bond is comparable to the slope of the c-axis for both temperatures. However, comparing the normalised values, the Co-N-bond elongates by 3.5% and the c-axis increases by 1.0% at

100 K, whereas for 200 K the Co-N-bond elongates by 3.0% and the c-axis by 1.5%. The slope of the bond length change of the Co-N-bond indicates that the bond elongations might in fact be connected to the c-axis elongation.
Based on this data it is proposed that the underlying damage mechanism in cyanocobalamin is a temperature dependent reaction within the complex. Upon irradiation global damaging of the crystal takes place with a much faster damage progression at 200 K compared to 100 K. The abstraction of specific hydrogen atoms observed at 100 K could be a temperature dependent factor (see section 1.1.1 in this chapter). Upon X-ray irradiation, hydrogen gas is generated which exerts stress onto the crystal structure. Since a crystal possesses an anisotropic modulus of elasticity, this stress is exerted onto each cell axis differently, explaining the strong elongation of the c-axis compared to the a- and b-axis. At a certain dose, the stress onto the unit cell axes results in cracking of the crystal and, thus, an increase in the crystal mosaicity. This explains why the expansion of the unit cell can be observed before an increase in mosaicity is detected.

XANES measurements of diiron-dithiolate revealed a temperature dependent damage behaviour for this compound (see fig. 2.7, section 2.2.4 in ***"Results"***). While no spectral changes could be observed at 100 K, a clear increase in the intensity of the white line could be found at 300 K. Since the compound contains Fe(II), an X-ray induced photoreduction can be excluded. Normalisation errors were also excluded by repeated evaluation of the spectra. Therefore, it is proposed that another damage process is taking place which causes the spectral changes. This process is clearly temperature dependent and only takes place above 100 K. The fact that pyrite, which does not contain any hydrogen atoms, was not damaged, while severe damage to diiron-dithiolate could be observed, indicates that the abstraction of hydrogen atoms could play a role here. However, to obtain any structural information it would be necessary to collect EXAFS spectra.

1.3.2 Contribution of X-ray induced photoreduction

XANES investigations of cyano- and methylcobalamin showed that cyanocobalamin is X-ray reduced upon irradiation, whereas methylcobalamin is not. Thus, X-ray diffraction data of these two compounds are well suited to investigate the contribution of X-ray induced photoreduction on the global damage process of B12 cofactors.

Decay of the mean intensity and the correlation coefficient as well as an increase in mosaicity and relative B-factor as function of dose showed a three- to fourfold higher susceptibility to X-ray radiation damage for cyanocobalamin compared to the biologically active methylcobalamin (see fig. 1.1, section 1.1 in ***"Results"***). Fitting the normalised unit cell volume increase by a linear function revealed a four- to fivefold higher susceptibility to X-ray radiation damage for cyanocobalamin compared to methylcobalamin. Additionally, the normalised unit cell volume of methylcobalamin was fitted by an exponential function. The fit revealed a unit cell volume increase by about 1.2%. Interestingly, a significant increase in mosaicity can only be found from 60 MGy to 80 MGy for methylcobalamin, the dose at which the normalised unit cell volume starts to reach a plateau. This reinforces the idea proposed in section 1.3.1 that the crystalline order, expressed in terms of mosaicity, does not deteriorate significantly before the unit cell expansion process reaches a more or less constant value.

Linear fitting of the normalised elongations of the bonds between the upper (Co-C) and lower (Co-N) axial ligand of the cobalt centre revealed only a twofold faster increase of both bond lengths for cyanocobalamin compared to methylcobalamin. The fact that the elongations were observed for both compounds led to the conclusion that they are not directly connected to the photoreduction of the metal centre. Hence, investigation of all three cell axes of both B12 cofactors was conducted. In both cases, a pronounced elongation of the c-axis could be found. The upper and lower axial ligand are oriented along this axis. For the a-axis, only a slight shortening could be observed, whereas for the b-axis, the axis length increases slightly in case of methylcobalamin and decreases slightly for cyanocobalamin. Damage induced changes therefore mainly take place along the c-axis of the crystal structure. Hence, it can be concluded that, although X-ray induced photoreduction is an important contributor to global radiation damage, it is not the only factor influencing the susceptibility of a compound to X-ray radiation damage.

The influence of the standard electrode potential of a metal centre, and thus, the potential of the metal centre to be photoreduced, on the susceptibility to global radiation damage has been investigated by X-ray diffraction measurements on the nickel(II) and copper(II) complexes of L-serine (NiSer and CuSer, respectively). These two metal centres were chosen due to the fact that the standard electrode potential of their metal ions for a M^{2+}/M^{+} redox reaction differs significantly (+0.159 V for copper(II) to copper(I), whereas nickel(II) is not reduced to nickel(I)[76]). It can be assumed that, while the value of the standard electrode potential changes for a metal organic complex of the respective metal ion, the probability of the two metal centres to be photoreduced is still in relation with the probability for the pure metal ion in solution. In addition to CuSer and NiSer, the copper(II) complex of L-isoleucine (CuIso) was investigated in order to determine the influence of the amino acid on the global damage process.

Due to the poor crystal quality and low resolution during the measurements, the dose series of NiSer and CuSer as well as CuIso were of poor data quality, so only the relative B-factor as well as the normalised unit cell volume increase were investigated in detail (see fig. 1.20, section 1.3 in ***"Results"***). All metal amino acid complexes showed radiation induced changes. The normalised unit cell volume increase as function of dose implies a twofold higher susceptibility to X-ray radiation damage for CuSer and CuIso compared to the NiSer. The normalised unit cell volume increase for CuSer and CuIso showed a similar behaviour. This indicates that the amino acid itself seems to have no influence on the global damage process, at least at 100 K.

The relative B-factor also shows a slightly more pronounced increase with dose for, CuSer and CuIso, compared to NiSer. Based on these findings, it is proposed that a X-ray induced redox reaction takes place within the copper complexes. CuSer and CuIso are likely to be involved in a M^{2+}/M^{+} redox reaction while NiSer does not undergo this kind of reduction. Therefore, CuSer and CuIso are probably reduced upon irradiation. During this, the ligands are probably oxidised.

Unit cell expansion as well as increase of the relative B-factor are known to occur as results of global radiation damage. All findings from this work imply that the specific redox process contributes to global damage.

It can be assumed that different space groups do not influence the expansion behaviour of the unit cell since CuSer ($P2_1$) as well as CuIso ($P2_12_12_1$) did not show any significant differences in their unit cell expansion.

The coordination sphere of the metal centre might be another influential factor. In case of the copper(II) complexes a square pyramidal coordination is observed, whereas for NiSer an octahedral coordination can be found. This factor cannot be completely excluded at the moment. Further investigations on complexes with metal centres with a comparable coordination sphere will be performed in the future to clarify this subject.

1.3.3 Contribution of hydrogen abstraction

Comparison of X-ray diffraction measurements of L-serine, L-alanine and thymidine was performed to investigate the contribution of site-specific hydrogen abstraction to the global radiation damage process.

It was found that L-serine is severely damaged upon exposure to large doses of X-ray radiation (see fig. 1.9, section 1.2.1 in ***"Results"***). The unit cell volume of L-serine obtained from X-ray measurements increases in a linear manner with absorbed dose. The crystal mosaicity is not affected until a dose of approximately 55 MGy is reached. A second "dose limit" can be observed at about 80 MGy. At this point all investigated parameters show an increased variability - as reflected especially in the R1 value from structure refinement. Hydrogen abstraction from a primary hydroxyl group might be an influential factor in this case. It has been suspected that the primary hydroxyl group within DL-serine is very susceptible to X-ray radiation induced changes.[155] Therefore, a hydrogen abstraction from this site might take place as specific damage process within L-serine as well. L-alanine is lacking this group and, thus, such a damage process should not take place in this compound.

Dose series of L-alanine did not show significant changes of all extracted values (see fig. 1.12, section 1.2.2 in ***"Results"***). Mean intensity and correlation coefficient as well as relative B-factor and R1 value from structure refinement only showed slight changes with dose. The mosaicity is not affected at all, even at the maximum dose of 55 MGy.

Comparison of the results for L-serine and L-alanine revealed a reduced susceptibility to radiation damage for L-alanine, although absorption coefficients and chemical composition for both compounds are comparable (see fig. 1.15, section 1.2.3 in ***"Results"***). This implies that the damage mechanisms of L-alanine and L-serine are different.

It is therefore proposed that the hydrogen abstraction from a primary hydroxyl group and the adjacent methylene group acts as a main contributor to radiation damage of L-serine. In contrast to this, L-alanine shows only little site specific hydrogen abstraction. This leads to L-alanine being more radiation hard than L-serine. It probably undergoes a less selective hydrogen abstraction. This kind of damage becomes more pronounced and affects the crystal structure at higher doses than selective hydrogen abstraction (L-serine).

X-ray measurements of thymidine also revealed a continuous damage process (see fig. 1.16, section 1.2.4 in ***"Results"***). Thymidine seems to be slightly radiation harder than L-serine: Correlation coefficient (0.981 for L-serine, 0.997 for thymidine at 50 MGy), relative B-factor (0.94 for L-serine, 0.43 for thymidine) and relative cell volume increase (1.03 for L-serine, 1.01 for thymidine) display a less pronounced damage progression with dose for thymidine compared to L-serine. Even at a dose of 100 MGy, an R1 value from structure refinement of thymidine of 0.049 was obtained. The crystal mosaicity also did not increase above 0.26° at maximum dose. The "dip" in correlation (see fig. 1.16, section 1.2.4 in ***"Results"***) within the dose series is probably caused by evaluation problems of the correlation between the first and the three datasets showing this "dip".

Mean intensity decay, linear increase of the relative B-factor and the only slightly exponential increase of the cell volume imply a damage process similar to that of L-serine. However, in contrast to L-serine, no bond length changes could be found in the X-ray data.

Investigation of the cell axes as function of dose showed a similar behaviour for all three axes. All axes increase with increasing X-ray dose. The order of magnitude of the increase differed strongly depending on the axis: The b-axis and c-axis were affected significantly stronger than the a-axis.

Therefore, it can be concluded that site specific hydrogen abstraction is an important contributor to the global damage process. The main difference between thymidine and L-serine is the percentage of hydrogen atoms abstracted from the compounds with dose. Within one L-serine molecule two hydrogen atoms are abstracted and form one molecule of H_2. In contrast to this, thymidine shows an abstraction of only one hydrogen atom leading to half a H_2 molecule per thymidine molecule.

The hydrogen gas generated in the crystal deteriorates the crystal structure. The more hydrogen gas is formed the more damage occurs in the crystal. This leads to the increased susceptibility to X-ray radiation of L-serine compared to thymidine.

Another factor might be the formation of the carbonyl group in case of L-serine, which might cause rearrangements in the crystal and, thus, disrupt the crystalline order.

1.3.4 Proposed global damage mechanism in single crystals

The results of this work indicate a global damage mechanism that can be divided into different steps. It has been shown that compounds which do not contain hydrogen atoms are less susceptible to damage by X-ray irradiation. Hence, it can be assumed that hydrogen abstraction is an important contributor in accelerating the global damage process. The susceptibility to selective hydrogen abstraction clearly depends on the chemical composition of the compound. The more hydrogen is abstracted from the compound, the more hydrogen gas is formed. This leads to more global damage to the sample and, thus, to a higher susceptibility to X-ray radiation damage.

The hydrogen gas formed in the sample exerts stress on the crystal lattice. Due to their anisotropic nature, crystals usually possess an elasticity tensor. Depending on the crystal symmetry, this results in a different expansion or contraction behaviour of the cell axes with dose. The changes in the unit cell axes generally cause an overall expansion of the unit cell. With increasing dose the amount of gas produced inside the crystal increases, leading to increasing stress within the crystal. At a certain dose, the stress is exceeding the tensile strength of the crystal. This leads to a disruption of the crystal lattice, which is reflected in an increase of mosaicity. Such an effect has been observed in the case of cyanocobalamin. Measurements at 100 K and 200 K have shown that either an expansion of the unit cell volume can be observed or an increase in mosaicity. Measurements on methylcobalamin supported the idea that the mosaicity increase becomes more pronounced after the unit cell volume increase reaches a plateau.

The Co-C- and Co-N-bond elongations observed for cyano- and methylcobalamin (see section 1.3.2 in ***"Results"***) can also be explained by this model: The bonds are aligned along the c-axis and, thus, elongated together with the c-axis.

The contribution of X-ray induced photoreduction can be explained if it is assumed that the reduced metal centre can act as kind of a hydrogen "generator" and, thus, accelerate the radiation damage process in the crystal. However, this subject still has to be investigated in further detail.

VI Conclusion and Outlook

Conclusion and Outlook

In this work, a systematic study of X-ray radiation damage was conducted using single crystal X-ray diffraction, X-ray absorption spectroscopy and neutron diffraction. This led to new models for X-ray induced photoreduction of metal organic complexes and global radiation damage to organic compounds in general. It could be revealed that hydrogen abstraction is an important contributor to both X-ray radiation damage processes. Further details on the different aspects are given in this chapter.

X-ray Absorption Near Edge Spectroscopy (XANES) and single crystal X-ray diffraction were applied to investigate several aspects of X-ray induced photoreduction of B12 cofactors.

XANES is a useful tool to directly probe the oxidation state of an atom. A systematic XANES study on cyanocobalamin, two Fe(III) and two Fe(II) complexes revealed a temperature, solvent and ligand dependence of X-ray induced photoreduction. From these measurements, a plausible model could be derived that describes the underlying mechanism of X-ray photoreduction as a redox reaction within the molecule.

High resolution single crystal X-ray diffraction offers the possibility to observe even very small structural changes and could therefore give first hints for a possible hydrogen abstraction at the ribose moiety of cyanocobalamin. This hydrogen abstraction could not be observed for methylcobalamin. In contrast to cyanocobalamin, methylcobalamin is not photoreduced, even at higher X-ray doses. Hence, the hydrogen abstraction is probably related to the photoreduction process.

XANES measurements on ammonium ferric citrate and potassium hexacyanoferrate, both containing the photosensitive Fe(III), also showed that X-ray induced photoreduction is a ligand dependent process. Upon irradiation, ammonium ferric citrate was photoreduced, going along with a decarboxylation of the ligand as oxidation reaction. The release of carbon dioxide makes the process irreversible. In contrast to this, potassium hexacyanoferrate was not photoreduced by X-rays.

Based on these results, a conclusive photoreduction mechanism for metal organic compounds could be proposed. It is suggested that X-ray induced photoreduction takes place within the molecule and involves a redox reaction between the metal centre, which is reduced, and the ligands, which are oxidised. This oxidation reaction is ideally accompanied by a leaving group being released from the molecule, making the reaction irreversible.

As an initial step of X-ray induced photoreduction, a low energy electron attaches to the metal centre yielding a short-lived excited state with a reduced metal centre.[129–132] Depending on the nature of the ligands, two different processes can take place following this excitation: If an oxidation reaction is induced in the ligand(s), the metal centre is permanently reduced. The reaction is made irreversible by a group that is leaving the compound. Charge conservation of the system is guaranteed by the release of an electron from the ligands. If no oxidation reaction takes place, the metal centre will react back to the initial oxidised state, going along with the release of the captured electron.

The results of this work indicate that hydrogen abstraction plays an important role in the process of X-ray induced photoreduction. In order to obtain fully conclusive results, it is necessary to perform further neutron diffraction experiments of unirradiated and X-ray photoreduced B12 samples to prove the possible hydrogen abstraction from the ligands. A combination of X-ray and neutron studies on B12 cofactors should therefore give further insight into the photoreduction mechanism of these samples and reveal a possible hydrogen abstraction in the ligands.

In this work, only static processes were investigated. The dynamics behind the X-ray photoreduction process can be investigated using time-resolved pump-probe XANES.[157,158] M-edge XANES experiments on B12 cofactors with femtosecond time resolution at free electron lasers, such as FLASH in Hamburg, can be used to gain further insight into the direct interaction between the low energy electrons and the metal centres. The short-lived change of the oxidation state of the metal centre by low energy electron attachment should be detectable by such experiments.

In addition to this, time-resolved diffraction studies conducted at hard X-ray lasers, such as LCLS in Stanford and the future XFEL in Hamburg, offer information about temporary structural changes.[159–162] Detection of structural changes within molecules such as B12 cofactors could be used to observe the assumed short-lived excited state upon interaction of the low energy electrons with the metal centre. This should reveal whether bond length changes between the ligands and the metal centre are a consequence of X-ray induced photoreduction or global radiation damage, since both processes follow a different timescale.

The findings of this work furthermore imply that the application of high pressures could mitigate the photoreduction process, if a gas release is involved as in the case of ammonium ferric citrate, since according to Le Chatelier's principle this will shift the chemical equilibrium within the sample, hereby reducing the gas volume and hence causing less damage to the sample. Therefore, a higher radiation dose would be required to cause the same effects as at standard pressure. XANES measurements of ammonium ferric citrate at high pressures are in preparation.

Hydrogen abstraction is assumed to play an important role in X-ray radiation damage. In this work, combined X-ray and neutron diffraction studies at cryogenic temperatures have been conducted to investigate selective hydrogen abstraction from organic samples. The amino acids L-serine and L-alanine as well as the nucleoside thymidine were chosen as model compounds for this study.

High resolution X-ray diffraction data gave a first hint for a possible hydrogen abstraction, which could be observed at a primary hydroxyl group in case of L-serine and thymidine. For L-alanine, which does not contain this group, no hints for a possible hydrogen abstraction could be found up to a dose of 55 MGy.

In order to obtain fully conclusive results, neutron diffraction was applied on previously

X-ray irradiated crystals of all three compounds. Measurements on L-serine revealed a selective hydrogen abstraction of two hydrogen atoms from the hydroxyl group and the adjacent methylene group. This abstraction went along with the formation of a carbonyl group, as indicated by a significant bond contraction between the carbon and the oxygen atom. Such a bond contraction was also found independently in X-ray data.

In case of thymidine, neutron diffraction showed a selective abstraction of a single hydrogen atom, also at a primary hydroxyl group. L-alanine did not show such a selective hydrogen abstraction. Here, a less selective abstraction of the three hydrogen atoms at the methyl group was observed at higher doses. It is therefore concluded that hydrogen abstraction is taking place preferentially from a primary hydroxyl group and that a compound lacking such a group can withstand higher doses of X-ray radiation.

It was assumed that the different damage behaviour of L-serine, from which two hydrogen atoms were abstracted, and thymidine, which showed the abstraction of only one hydrogen atom from each molecule, can be explained by the intramolecular hydrogen distance and the torsion angle of the hydroxyl group with respect to the adjacent methylene group. The influence of the intramolecular hydrogen distances and the torsion angle on the damage mechanism in organic compounds will be investigated in the future by neutron measurements on the nucleoside adenosine (see fig. 1.10), which displays similarities to L-serine regarding the distance and orientation of the hydrogen atoms of the primary hydroxyl group and the adjacent methylene group.

In-situ Raman spectroscopy[163] at 100 K on single crystals during irradiation is a useful tool to investigate radiation induced changes in particular groups of a molecule. Since Raman spectroscopy is independent of the sample state, X-ray induced changes can still be followed using this method, even if the crystalline order has deteriorated too strongly to obtain diffraction images. Raman investigations of L-serine could offer the possibility to investigate a change at the primary hydroxyl and the adjacent methylene group and even observe the growth of an hydrogen gas signal if the sensitivity of the setup is high enough.

K-edge EXAFS of the carbon within the samples could also be a useful tool to investigate

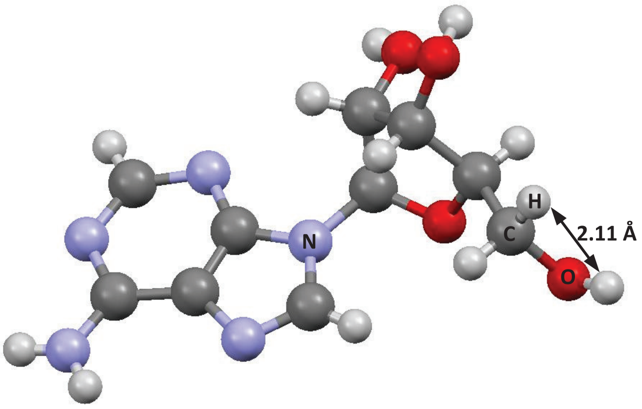

Figure 1.10: Structure of adenosine obtained from X-ray diffraction, with the respective H - H distance.

structural changes, especially at higher doses, where the crystal structure has already been severely affected.

Analytical methods such as Nuclear Magnetic Resonance (NMR),[164,165] Electron Paramagnetic Resonance (EPR),[166–168] Correlation Spectroscopy (COSY),[169] Mass Spectrometry (MS)[170] and High-Performance Liquid Chromatography (HPLC)[171,172] could be used to investigate the different reaction products that are produced upon irradiation of L-serine. One has to consider that most of these methods are not typically conducted at 100 K but at room temperature. Warming of the crystals from 100 K to room temperature will most probably lead to further reactions in the molecule.

Single crystal X-ray diffraction and neutron diffraction were applied to investigate global radiation damage. Upon irradiation with high doses of X-ray radiation, all compounds showed a decrease in mean intensity and correlation coefficient as well as an increase in the relative B-factor, an expansion of the unit cell volume and an increase in mosaicity. Results from X-ray diffraction indicate that a significant increase of the mosaicity can be observed after the unit cell expansion nearly reaches a plateau.

A combination of X-ray and neutron diffraction measurements showed that compounds, in which selective hydrogen abstraction from a primary hydroxyl group takes place, are more susceptible to radiation damage than the ones lacking this group. It could furthermore be shown that a compound from which two hydrogen atoms are abstracted per molecule is more susceptible to radiation damage as one, from which only a single hydrogen atom is abstracted.

This systematic behaviour led to a general model for global radiation damage. The unit cell expansion is caused by the formation of hydrogen gas, that is formed upon hydrogen abstraction from the compound. An expansion of the unit cell is the consequence of this process. Due to the anisotropic nature of the crystal, X-ray radiation affects each unit cell axis differently. The more gas is formed inside the crystal, the more stress is exerted on the crystal lattice. This causes each of the unit cell axes to either elongate or contract. This anisotropic behaviour is probably a consequence of the anisotropic elasticity tensor. At a certain dose, the stress exerted by the gas in the crystal exceeds the tensile strength, which leads to cracks in the crystalline structure. This effect is reflected in a mosaicity increase after a certain dose is reached.

The higher susceptibility of photoreduced compounds compared to the ones, that are not photoreduced, can be explained by the metal centre acting as kind of a hydrogen generator, which leads to an accelerated production of hydrogen gas and therefore an acceleration of the global damage process.

Further support for this proposed model could be made by comparison of the modulus of elasticity of a crystal to the X-ray induced damage behaviour in the crystal.

Bibliography

[1] A.A. McDowell, R.S. Celestre, N. Tamura, R. Spolenak, B. Valek, W.L. Brown, J.C. Bravman, H.A. Padmore, B.W. Batterman, J.R. Patel, Nucl. Instrum. and Meth. Phys. Res. A **467** **468**, 936 943, 2001

[2] D. Grolimund, M. Senn, M. Trottmann, M. Janousch, I. Bonhoure, A.M. Scheidegger, M. Marcus, Spect. Acta B **59**, 1627 - 1635, 2004

[3] O. Hignette, P. Cloetens, G. Rostaing, P. Bernard, C. Morawe, Rev. Sci. Instrum. **76**, 063709-1 - 063709-5, 2005

[4] C. Nave & E.F. Garman, J. Synchrotron Rad. **12**, 257 - 260, 2005

[5] R.B.G. Ravelli & E.F. Garman, Current Opinion in Structural Biology **16**, 624 - 629, 2006

[6] J.M. Holton, J. Synchrotron Rad. **16**, 133 - 142, 2009

[7] E.F. Garman, Acta Cryst. D **66**, 339 - 351, 2010

[8] B. Ziaja, R.A. London, J. Hajdu, J. Appl. Phys. **97**, 064905 - 064909, 2005

[9] E.F. Garman, Current Opinion in Structural Biology **13**, 545 - 551, 2003

[10] C. Nave, Radiat. Phys. Chem. **45**, 483 -490, 1995

[11] W.P. Burmeister, Acta Cryst. D **56**, 328 - 341, 2000

[12] M. Weik, R.B.G. Ravelli, I. Silman, J.L. Sussman, P. Gros, J. Kroon, Protein Sci. **10**, 1953-1961, 2001

[13] J. Cadet & M. Berger, Int. J. Rad. Biol. **47**, 127 - 143, 1985

[14] R.B. Ravelli & S.M. McSweeney, Structure **8**, 315 - 328, 2000

[15] Y. Zubavichus, O. Fuchs, L. Weinhardt, C. Heske, E. Umbach, J.D. Denlinger, M. Grunze, Radiation Research **161**, 346 - 358, 2004

[16] M. Weik, R.B.G. Ravelli, G. Kryger, S. McSweeney, M.L. Raves, M. Harel, P. Gros, I. Silman, J. Kroon, J.L. Sussman, PNAS **97**, 623 - 628, 2000

[17] Y. Matsui, K. Sakai, M. Murakami, Y. Shiro, S. Adachi, H. Okumura, T. Kouyama, J. Mol. Biol. **324**, 469 - 481, 2002

[18] I. Schlichting, J. Berendzen, K. Chu, A.M. Stock, S.A. Maves, D.E. Benson, R.M. Sweet, D. Ringe, G.A. Petsko, S.G. Sligar, Science **287**, 1615 - 1622, 2000

[19] J. Yano, J. Kern, K.D. Irrgang, M.J. Latimer, U. Bergmann, P. Glatzel, Y. Pushkar, J. Biesiadka, B. Loll, K. Sauer, J. Messinger, A. Zouni, V.K. Yachandra, PNAS **102**, 12047 - 12052, 2005

[20] T. Beitlich, K. Kühnel, C. Schulze-Briese, R.L. Shoeman, I. Schlichting, J. Synchrotron Rad. **14**, 11-23, 2007

[21] M.C. Corbett, M.J. Latimer, T.L. Poulos, I.F. Sevrioukova, K.O. Hodgson, B. Hedmann, Acta Cryst. D **63**, 951 - 960, 2007

[22] H. Dau, P. Liebisch, M. Haumann, Phys. Chem. Chem. Phys. **6**, 4781 - 4792, 2004

[23] F. Champloy, K. Gruber, G. Jogl, C. Kratky, J. Synchrotron Rad. **7**, 267 -273, 2000

[24] J. Wuerges, J.-W. Lee, Y.-I. Yim, H.-S. Yim, S.-O. Kang, K. Djinovic-Carugo, PNAS **101**, 8569 - 8574, 2004

[25] O. Carugo & K. Djinovic-Carugo, TIBS **30**, 213 - 219, 2005

[26] M. Haumann, A. Grundmeier, I. Zaharieva, H. Dau, Science **310**, 17384 - 17389, 2008

[27] J. E. Penner-Hahn, M. Murata, K.O. Hodgson, H.C. Freeman, Inorg. Chem. **28**, 1826 - 1832, 1989

[28] R.F. Roberts, J. El. Spec. Rel. Phenom. **4**, 273 - 291, 1974

[29] I. Arčon, J. Kolar, A. Kodre, D. Hanžel, M. Strlič, X-ray Spectrom. **36**, 199 - 205, 2007

[30] B. Chance, P. Angiolillo, E.K. Yang, L. Powers, FEBS Lett. **112**, 178 - 182, 1980

[31] E.-G. Niemann, *Biophysics*, edited by W. Hoppe, W.H.M. Lohmann & H. Zegler, Springer, 289 - 300, 1983

[32] W. Choi & M.R. Hoffmann, Environ. Sci. Technol. **29**, 1646 - 1654, 1995

[33] M.V. Rama Rao & T. Shripathi, J. El. Spec. Rel. Phenom. **87**, 121 - 126, 1997

[34] E. Paparazzo & G.M. Ingo, J. El. Spec. Rel. Phenom. **95**, 301 - 304, 1998

[35] M. Grabolle, M. Haumann, C. Müller, P. Liebisch, H. Dau, J. Biol. Chem. **281**, 4580 - 4588, 2006

[36] G.I. Berglund, G.H. Carlsson, A.T. Smith, H. Szoke, A. Henriksen, J. Hajdu, Nature **417**, 463 - 468, 2002

[37] A. Meents, S. Gutmann, A. Wagner, C. Schulze-Briese, PNAS **107**, 1094 - 1099, 2010

[38] C.V. Iancu, E.R.Wright, J.B. Heymann, G.J. Jensen, J. Structural Biol. **153**, 231 - 240, 2006

[39] H. Hope, Acta Cryst. B **44**, 22 - 26, 1988

[40] E.F. Garman & T.R. Schneider, J. Appl. Cryst. **30**, 211 - 237, 1997

[41] E. Garman, Acta Cryst. D **55**, 1641 - 1653, 1999

[42] A. Meents, A. Wagner, R. Schneider, C. Pradervand, E. Pohl, C. Schulze-Briese, Acta Cryst. D **63**, 302 - 309, 2007

[43] B.L. Hanson, J.M. Harp, K. Kirschbaum, C.A. Schall, K. DeWitt, A. Howard, A.A. Pinkerton, G.J. Bunick, J. Synchrotron Rad. **9**, 375 - 381, 2002

[44] U. Chinte, B. Shah, Y.-S. Chen, A. A. Pinkerton, C. A. Schall, B. L. Hanson, Acta Cryst. D **63**, 486-492, 2007

[45] M. Haumann, P. Pospisil, M. Grabolle, C. Mueller, P. Liebisch, V.A. Sole, T. Neisius, J. Dittmer, L. Iuzzolino, H. Dau, J. Synchrotron Rad. **9**, 304 - 308, 2002

[46] M. Haumann, P. Liebisch, C. Mueller, M. Barra, M. Grabolle, H. Dau, Science **310**, 1019 - 1021

[47] A. Meents, B. Dittrich, S. Gutmann, J. Synchrotron Rad. **16**, 183 - 190, 2009

[48] M.P. Philpott, S.C. Hayes, C.L. Thomsen, P.J. Reid, Chem. Phys. **263**, 389 - 400, 2001

[49] E.L. Rickes, N.G. Brink, F.R. Koniuszy, T.R. Wood, K. Folkers, Science **107**, 396 - 397, 1948

[50] R. Banerjee, *Chemistry and Biochemistry of B12*, John Wiley & Sons Inc., 1999

[51] C.L. Drennan, R.G. Matthews, M.L. Ludwig, Current Opinion in Chemical Biology. **4**, 919 - 929, 1994

[52] F. Watanabe, Exp. Biol. Med. **232**, 1266 - 1274, 2007

[53] J.R. Roth, J.G. Lawrence, T.A. Bobik, Annual Rev. Microbiology. **50**, 137 - 181, 1996

[54] B. Kräutler, D. Arigoni, B.T. Golding, *Vitamin B12 and B12-proteins*, Wiley-VCH Verlag GmbH, 1998

[55] H.G. Alt, Angew. Chem. **96**, 752 - 769, 1984

[56] S. Pehknonen, Analyst. **120**, 2655 - 2663, 1995

[57] R.R. Crichton, J.-L. Pierre, BioMetals **14**, 99 - 112, 2001

[58] R.E. Dickerson & I. Geis, *Hemoglobin: Structure, function, evolution, and pathology.*, Benjamin/Cummings Pub. Co., 1983

[59] I. Lalezari, P. Lalezari, C. Poyart, M. Marden, J. Kister, B. Bohn, G. Fermi, M. F. Perutz, Biochemistry **29**, 1515 - 1523, 1990

[60] J.B. Wittenberg & B.A. Wittenberg, Annu. Rev. Biophys. Biophys. Chern. **19**, 217 - 241, 1990

[61] H. Oexle, E. Gnaiger, G. Weiss, Biochim. Biophys. Acta **1413**, 99 - 107, 1999

[62] D. Richardson & E. Baker, J. Bio. Chem. **267**, 13972 - 13979, 1992

[63] D. Trinder & E. Morgan, J. Am. Phys. Soc. **275**, G279 - G286, 1998

[64] I. Gautier-Luneau, C. Merle, D. Phanon, C. Lebrun, F. Biaso, G. Serratrice, J.-L. Pierre, Chem. Euro. J. **11**, 2207 - 2219

[65] H.B. Abrahamson, J. Chem. Educ. **78**, 301, 2001

[66] J.L. Frahn, Aust. J. Chem. **11**, 399 - 405, 1958

[67] J.H. Bennett, E.H. Lee, D.T. Krizek, R.A. Olsen, J.C. Brown, J. Plant Nutrition **5**, 335 - 344, 1982

[69] S.J. George, J. Fu, Y. Guo, O.B. Drury, S. Friedrich, T. Rauchfuss, P.I. Volkers, J.C. Peters, V. Scott, S.D. Brown, C.M. Thomas, S.P. Cramer, Inorg. Chim. Acta **361**, 1157 - 1165, 2008

[70] W. Wu, J.A. Thomas, N. Cheng, L.W. Black, A.C. Steven, Science **335**, 182, 2012

[71] C. von Sonntag, *The Chemical Basis of Radiation Biology*, Taylor & Francis, 1987

[72] R. Garrett & C.M. Grisham, *Biochemistry*, Brooks/Cole, 2010

[73] R.B. Ravelli, P. Thevenau, S.M. McSweeney, M. Caffrey, J. Synchrotron Rad. **9**, 355 - 360, 2002

[74] T.-Y. Teng & K. Moffat, J. Synchrotron Rad. **9**, 198 - 201, 2002

[75] A.J. Bard, J. Jordan, R. Parsons, *Standard Potentials in Aqueous Solution*, Marcel Dekker, 1985

[76] A.F. Hollemann & N. Wiberg, *Lehrbuch der Anorganischen Chemie*, Walter de Gruyter & Co., 1995

[77] M.M. Woolfson, *An Introduction to X-ray crystallography*, Cambride University Press, 1997

[78] J. Als-Nielsen & D. McMorrow, *Elements of Modern X-ray Physics*, John Wiley & Sons Ltd., 2001

[79] C.S. Barrett, *Structure of Metals*, McGraw-Hill Book, 1952

[80] W.C. Röntgen, *Über eine neue Art von Strahlen.*, Sitzungsberichte der Physikalisch Medizinischen Gesellschaft Würzburg, 137 - 147, 1895

[81] H.D. Flack, Acta Cryst. A **39**, 876 - 881, 1983

[82] H.D. Flack & G. Bernadinelli, Acta Cryst. A **55**, 908 - 915, 1999

[83] D.C. Koningsberg, R. Prins, *X-ray Absorption: Principles, Applications, Techniques of EXAFS, SEXAFS and XANES*, John Wiley & Sons, 1988

[84] G. Bunker *Introduction to XAFS*, Cambridge University Press, 2010

[85] S.R. Bare, *XANES Measurements and Interpretation*, EXAFS Data Collection and Analysis Course, NSLS, July 14-17, 2003

[86] P.A. Lee, C.H. Citrin, P. Eisenberger, B.M. Kincaid, Reviews of Modern Physics **53**, 769 - 806, 1981

[87] C.C. Wilson, *Single Crystal Neutron Diffraction from Molecular Materials*, World Scientific, 2000

[88] J. Chadwick, Nature **129**, 312, 1932

[89] G.L. Squires, *Introduction to the theory of thermal neutron scattering*, Dover Publications, 1978

[90] E. Fermi & L. Marshall, Phys. Rev. **71**, 666 - 677, 1947

[91] D.A. Keen, M.J. Gutmann and C.C. Wilson, J. Appl. Cryst. **39**, 714 - 722, 2006

[92] L.K. Mansur, A.F. Rowcliffe, R.K. Nanstad, S.J. Zinkle, W.R. Corwin, R.E. Stoller, J. Nucl. Mat. **329-333**, 166 - 172, 2004

[93] W. Kockelmann, G. Frei, E.H. Lehmann, P. Vontobel, J.R. Santisteban, Nucl. Instr. Meth. Phys. Res. A **578**, 421 - 434. 2007

[94] E.F. Garman & C. Nave, J. Synchrotron Rad. **9**, 327 - 328, 2002

[95] R. Henderson, Proc. Roy. Soc. Lond. B **23**, 6 8, 1990

[96] T.Y. Teng, J. Appl. Crystallograph. **25**, 387 - 391, 1990

[97] A.J.C. Wilson, Nature **150**, 156, 1942

[98] G.D.D. Jones, J.S. Lea, M.C.R. Symons, F.A. Taiwo, Nature **330**, 772 773, 1987

[99] P. Persson, S. Lunell, A. Szoke, B. Ziaja, J. Hajdu, Protein Sci. **10**, 2480 2484, 2001

[100] W. Kabsch, Acta Cryst. D **66**, 125 - 132, 2010

[101] G.M. Sheldrick, Acta Cryst. A **64**, 112 - 122, 2007

[102] R.J. Dejus & M.S. del Rio, Rev. Sci. Instrum. **67**, 9, 1996

[103] D. van der Helm, W.A. Franks. Acta Cryst. B **25**, 451 - 457, 1969

[104] D. van der Helm, M. Bilayet Hossain. Acta Cryst. B **25**, 457 - 463, 1969

[105] C.M. Weeks, A. Cooper, D.A. Norton. Acta Cryst. B **25**, 443 - 450, 1969

[106] K. Gruber, C. Kratky. Current Opinion in Chemical Biology. **6**, 598 - 603, 2002

[107] M. Newville. J. Synchrotron Rad. **8**, 322 - 324, 2001

[108] Y. Morioka, K. Yoriumi, T. Ito, A. Saito, I. Nakagawa, J. Phys. Soc. Jpn. **54**, 2184 - 2189, 1985

[109] L. Schwartz, J. Ekström, R. Lomoth, S. Ott, Chem. Commun., 4206 - 4208, 2006

[110] P, Bayliss, American Mineralogist **74**, 1168 - 1176, 1989

[111] Neutron News **3**(3), 29-37, 1992

[112] F.P.A. Fabbiani, G. Buth, B. Dittrich, H. Sowa, CrystEngComm **12**, 2541 - 2550, 2010

[113] F. Mancia, N.H. Keep, A. Nakagawa, P.F. Leadlay, S. McSweeney, B. Rasmussen, P. Bosecke, O. Diat, P.R. Evans. Structure **4**, 339 - 350, 1996

[114] R. Reitzer, K. Gruber, G. Jogl, U.G. Wagner, H. Bothe, W. Buckel, C. Kratky. Structure **7**, 891 - 902, 1999

[115] N. Shibata, J. Masuda, T. Tobimatsu, T. Toraya, K. Suto, Y. Morimoto, N. Yasuoka. Structure **7**, 997 - 1008, 1999

[116] R.V. Banerjee, R.G. Matthews, FASEB Journal **4**, 1450 - 1459, 1990

[117] J.T. Drummond, R.G. Matthews, Biochemistry **33**, 3732 - 3741, 1994

[118] D.M. Hoover, J.T. Jarrett, R.H. Sands, W.R. Dunham, M.L. Ludwig, R.G. Matthews, Biochemistry **36**, 127 - 138, 1997

[119] J.T. Jarrett, D.M. Hoover, M.L. Ludwig, R.G. Matthews, Biochemistry **37**, 12649 - 12658, 1998

[120] N. Shibata, J. Masuda, Y. Morimoto, N. Yasuoka, T. Toraya, Biochemistry **41**, 12607 12617, 2002

[121] K. Gruber, R. Reitzer, C. Kratky, Angew. Chem. Int. Ed. **40**, 3377 - 3380, 2001

[122] F. Champloy, G. Jogl, R. Reitzer, W. Buckel, H. Bothe, B. Beatrix, G. Broeker, A. Michalowicz, W. Meyer-Klaucke, C. Kratky, J. Am. Chem. Soc. **121**, 11780 11789, 1999

[123] S. Van Doorslaer, G. Jeschke, B. Epel, D. Goldfarb, R.-A. Eichel, B. Kräutler, A. Schweiger, J. Am. Chem. Soc. **125**, 5915 5927, 2003

[124] J. Coves & M. Fontecave, Eur. J. Biochem. **211**, 635 - 641, 1993

[125] P.M. Harrison & P. Arosio, Biochim. Biophys. Acta **1275**, 161 - 203, 1996

[126] J.J. Shiang, A.G. Cole, R.J. Sension, K. Hang, Y. Weng, J.S. Trommel, L.G. Marzilli, T. Lian, J. Am. Chem. Soc. **128**, 801 - 808, 2006

[127] J.J. Shiang, L.A. Walker II, N.A. Anderson, A.G. Cole, R.J. Sension, J. Phys. Chem. B **103**, 10532 - 10539, 1999

[128] R.J. Sension, D.A. Harris, A.G. Cole, J. Phys. Chem. B **109**, 21954 - 21962, 2005

[129] L.M. Chanin, A.V. Phelps, M.A. Biondi, Phys. Rev. **128**, 219 - 230, 1962

[130] K. Aflatooni, G.A. Gallup, P.D. Burrow, J. Phys. Chem. A **102**, 6205 - 6207, 1998

[131] B. Boudaïffa, P. Cloutier, D. Hunting, M.A. Huels, L. Sanche, Science **287**, 1658 - 1660, 2000

[132] R. Barrios, P. Skurski, J. Simons, J. Phys. Chem. B **106**, 7991 - 7994, 2002

[133] S. Ptasinska, S. Denifl, P. Scheier, E. Illenberger, T.D. Mrk, Angew. Chem. Int. Ed. **44**, 6941 - 6943, 2005

[134] R.A.D. Wentworth & T.S. Piper, Inorg. Chem. **5**, 709 - 714, 1965

[135] A.B.P. Lever, *Inorganic Electronic Spectroscopy*, Elsevier, 1984

[136] P. Kofod, Inorg. Chem. **34**, 2768 - 2770, 1995

[137] S.M. Chemaly, Dalton Trans. **42**, 5766 - 5773, 2008

[138] H.L. Schläfer, G. Gliemann, *Basic principles of ligand field theory*, Wiley-Interscience, 1969

[139] M. Schwartz, P. Marshall, R.J. Berry, C.J. Ehlers, G.A. Petersson, J. Phys. Chem. A **102**, 10074 - 10081, 1998

[140] R.D. Cates, M.T. Bowers, W.T. Huntress Jr, J. Phys. Chem. **85**, 313 - 315, 1981

[141] E. Würzberg & P.L. Houston, J. Chem. Phys. **72**, 5915 - 5923, 1980

[142] F.H. Grau & W.J. Halliday, Nature **179**, 733 - 734, 1957

[143] H.C. Box & E.E. Budzinski, J. Chem. Phys. **55**, 2446 - 2448, 1971

[144] M.D. Sevilla, J.B. D'Arcy, K.M. Morehouse, J. Phys. Chem. **83**, 2887 - 2892, 1979

[145] H.B. Abrahamson , A.B. Rezvani, J.G. Brushmiller, Inorg. Chim. Acta **226**, 117 - 127, 1994

[146] J.W. Murray, E. Rudino-Pinera, R.L. Owen, M. Grininger, R.B.G. Ravelli, E.F Garman, J. Synchrotron Rad. **12**, 268 - 275, 2005

[147] M. Warkentin, R. Badeau, J. Hopkins, R.E. Thorne, Acta Cryst. D **67**, 792 - 803, 2011

[148] E.B. Smith *Basic Chemical Thermodynamics*, Imperial College Press, 1973

[149] H. Giefers, M. Pravica, H.-P. Liermann, W. Yang, Chem. Phys. Let. **429**, 304 - 309, 2006

[150] E. Balanzat, N. Betz, S. Bouffard, Nucl. Instr. Meth. Phys. Res. B **105**, 46-54, 1995

[151] R.D. Leapman & S. Sun, Ultramicroscopy **59**, (1-4):71-9, 1995

[152] T. Steckenreiter, E. Balanzat, H. Fuess, C. Trautmann, J. Polym. Sci. A: Polym. Chem. **37**, 4318 - 4329, 1999

[153] L. Montanari, M. Costantini, E.C. Signoretti, L. Valvo, M. Santucci, M. Bartolomei, P. Fattibene, S. Onori, A. Faucitano, B. Conti, I. Genta, J. Contr. Rel. **56**, 219 229, 1998

[154] K.T. Nguyen & J.L. West, Biomaterials **23**, 4307 - 4314, 2002

[155] J.Y. Lee & H.C. Box, J. Chem. Phys. **55**, 2598 - 2600, 1971

[156] J. Hüttermann, W.A. Bernhard, E. Haindi, G. Schmidt, J. Phys. Chem. **81**, 228 - 232, 1976

[157] C. Bressler, M. Chergui, P. Pattison, M. Wulff, A. Filipponi, R. Abela, Proc. SPIE **3451**, 108 - 116, 1998

[158] C. Bressler, C. Milne, V.-T. Pham, A. El Nahhas, R. M. van der Veen, W. Gawelda, S. Johnson, P. Beaud, D. Grolimund, M. Kaiser, C. N. Borca, G. Ingold, R. Abela and M. Chergui, Science **323**, 489 - 492, 2009

[159] R.W. Schoenlein, W.P. Leemans, A.H. Chin, P. Volfbeyn, T.E. Glover, P. Balling, M. Zolotorev, K.-J. Kim, S. Chattopadhyay, S.V. Shank, Science **274**, 236 - 238, 1996

[160] C. Rischel, A. Rousse, I. Uschmann, P.-A. Albouy, J.-P. Geindre, P. Audebert, J.-C. Gauthier, E. Förster, J.-L. Martin, A. Antonetti, Nature **390**, 490 - 492, 1997

[161] A.H. Chin, R.W. Schoenlein, T.E. Glover, P. Balling, W.P. Leemans, C.V. Shank, Phys. Rev. Lett. **83**, 336 - 339, 1999

[162] J. Larsson, Meas. Sci. Technol. **12**, 1835 - 1840, 2001

[163] J.R. Ferraro, K. Nakamoto, C.W. Brown, *Introductory Raman Spectroscopy*, Academic Press, 2003

[164] N.E. Jacobsen. *NMR Spectroscopy Explained: Simplified Theory, Applications and Examples for Organic Chemistry and Structural Biology*, John Wiley & Sons, 2007

[165] M. Balci, *Basic 1H- and 13C-NMR Spectroscopy*, Elsevier, 2005

[166] M. Che & E. Giamello, Stud. Surf. Sci. Catal. **57**, B265 - B332, 1990

[167] J.A. Weil, J.R. Bolton, *Electron paramagnetic resonance: elementary theory and practical applications*, John Wiley & Sons, 2007

[168] D. Becker, *Electron Paramagnetic Resonance Volume 20*, edited by B.C. Gilbert, M.J. Davies, D.M. Murphy. RSC Publishing, 2007

[169] W. Demtröder, *Laser Spectroscopy, Volume 2, Experimental Techniques*, Springer, 2008

[170] E. de Hoffmann, V. Stroobant, *Mass spectrometry: principles and applications*, John Wiley & Sons, 2007

[171] S. Lindsay, *Einführung in die HPLC: Analytische Chemie*, John Wiley & Sons, 1996

[172] M.C. McMaster, *HPLC, a practical user's guide*, 2nd ed., John Wiley & Sons, 2007

Selbstständigkeitserklärung

Ich erkläre, dass ich die vorliegende Arbeit selbstständig und unter Verwendung der angegebenen Hilfsmittel, persönlichen Mitteilungen und Quellen angefertigt habe.

Ort, Datum

Unterschrift

Danksagung

Zunächst möchte ich mich bei Herrn Prof. Dr. Edgar Weckert für die Chance, diese Dissertation in seiner Arbeitsgruppe anzufertigen, für die Übernahme des Gutachtens bei der Dissertation und der Disputation und für die vielen Diskussionen und Ratschläge bedanken. Ein ebenso großes Dankeschön geht an Herrn Dr. Alke Meents für die vielen anregenden Diskussionen, die Übernahme des Gutachtens bei der Disputation und natürlich die vielen guten Tipps und die Hilfestellung bei den Experimenten.

Herrn Prof. Dr. Dr. Christian Betzel danke ich für die Erstellung des Zweitgutachtens.

Ein großer Dank auch an die aktuellen und ehemaligen Mitglieder der Arbeitsgruppe Weckert für die vielen interessanten Diskussionen in unseren Gruppentreffen, sowie an das gesamte Team der Beamline P11 für die tolle Arbeitsatmosphäre und stete Hilfe, wo immer sie nötig war. Ein ganz besonderer Dank gilt hier Anja Burkhardt für die große Hilfe bei allen Experimenten, viele hilfreiche Tipps und anregende Diskussionen und das Korrekturlesen meiner Arbeit.

Ein herzliches Dankeschön geht an das Team der HASYLAB-Werkstatt von Jens Brehling, ohne deren Hilfe, oft auch in letzer Minute, viele Experimente nicht möglich gewesen wären.

Ebenfalls herzlich bedanken möchte ich mich bei bei David Barnes und allen weiteren "Korrekturlesern", die mit ihren zahllosen Hinweisen und Fragen, welcher Natur auch immer sie waren, dazu beigetragen haben, diese Arbeit fertigzustellen.

Natürlich danke ich auch allen weiteren Leuten, die zum Gelingen dieser Arbeit beigetragen haben, und hier nicht namentlich erwähnt werden.

Mein größter Dank gilt meiner Familie und meinen Freunden, auf deren gutes Zureden und Verständnis ich mich während der gesamten Zeit verlassen konnte. Ganz besonders erwähnen möchte ich hier meine Eltern, die mich in jeder Situation zum Durchhalten ermutigt und die gesamte Zeit auf jede nur erdenkliche Weise unterstützt haben. Ein großer Dank geht zudem an meine Schwester Vanessa, sowie an Carlo, Matthias, Sebastian F., Sebastian R., Anna und Guido, die nicht nur fachlich, sondern vor allem durch ihre moralische Untertützung zum Gelingen dieser Arbeit beigetragen haben.

Appendix

A.4 X-ray diffraction of B12 cofactors

A.4.1 Cyanocobalamin

Crystal growth: 12 mg of cyanocobalamin ($CoC_{63}H_{88}N_{14}O_{14}P$) were solved in 1 ml water. The deep-red solution was then mixed with 1.5 ml isopropyl alcohol in a petri dish. The dish was then stored in an isopropyl alcohol atmosphere. The system was closed, in order to prevent the evaporation of isopropyl alcohol. No cryoprotectant was used. Small rectangular crystals between $400 \times 250 \times 200$ μm^3 and $100 \times 80 \times 20$ μm^3 grew within three days by vapor diffusion.

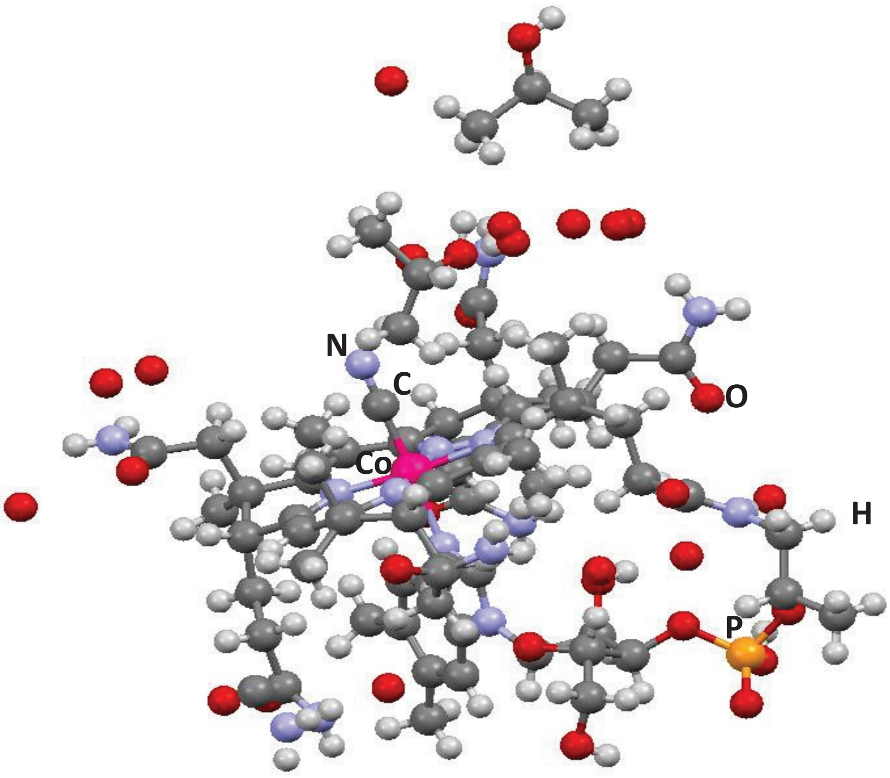

Figure A.11: Molecular structure of cyanocobalamin solved from X-ray data.

Table A.1: Data collection parameters for measurements of the 1st cyanocobalamin crystal.

Crystal size	$400 \times 200 \times 200\ \mu m^3$
Detector distance	70 mm
Starting angle	0°
Oscillation range	2°
Exposure time	1 s
No. of images	4860
Filter transmission	0.156
Photon flux	$15.36 \cdot 10^9$ ph/s
Temperature	100 K
Energy	16.45 keV
Wavelength	0.7537 Å

Table A.2: Data collection parameters for measurements of the 2nd cyanocobalamin crystal.

Crystal size	400 × 400 × 300 μm^3
Detector distance	70 mm
Starting angle	0°
Oscillation range	2°
Exposure time	1 s
No. of images	4860
Filter transmission	1.0
Photon flux	$98.43 \cdot 10^9$ ph/s
Temperature	100 K
Energy	16.45 keV
Wavelength	0.7537 Å

Table A.3: Data collection parameters for measurements of the 3rd cyanocobalamin crystal.

Crystal size	380 × 150 × 150 μm^3
Detector distance	65 mm
Starting angle	0°
Oscillation range	2°
Exposure time	1 s
Number of images	3600
Filter transmission	1.0
Photon flux	$108 \cdot 10^9$ ph/s
Temperature	200 K
Energy	16.45 keV
Wavelength	0.7537 Å

Table A.4: Data evaluation and structure refinement parameters of the 1st cyanocobalamin crystal.

Rmrgd-F	1.7%
Resolution	0.7 Å
Data completeness	73.8%
Number of reflections (total)	12922
Number of reflections (gt)	12417
Cell constants	a = 15.77 Å b = 22.29 Å c = 25.41 Å $\alpha = 90.00°$ $\beta = 90.00°$ $\gamma = 90.00°$
Space group	$P2_12_12_1$
R1 value from structure refinement	0.0613
Solvent molecules	$9{\cdot}H_2O + 1.33{\cdot}C_3H_8O$

Table A.5: Data evaluation and structure refinement parameters of the 2nd cyanocobalamin crystal.

Rmrgd-F	1.7%
Resolution	0.7 Å
Data completeness	83.8%
Number of reflections (total)	13272
Number of reflections (gt)	13092
Cell constants	a = 15.75 Å b = 22.33 Å c = 25.33 Å $\alpha = 90.00°$ $\beta = 90.00°$ $\gamma = 90.00°$
Space group	$P2_12_12_1$
R1 value from structure refinement	0.0595
Solvent	$9.25{\cdot}H_2O + 0.75{\cdot}C_3H_8O$

Table A.6: Data evaluation and structure refinement parameters the 3rd cyanocobalamin crystal.

Rmrgd-F	3.4%
Resolution	0.8 Å
Data completeness	86.8%
Number of reflections (total)	13861
Number of reflections (gt)	13052
Cell constants	a = 15.80 Å b = 22.32 Å c = 25.54 Å $\alpha = 90.00°$ $\beta = 90.00°$ $\gamma = 90.00°$
Space group	$P2_12_12_1$
R1 value from structure refinement	0.0640
Solvent	$7.25 \cdot H_2O + 1.25 \cdot C_3H_8O$

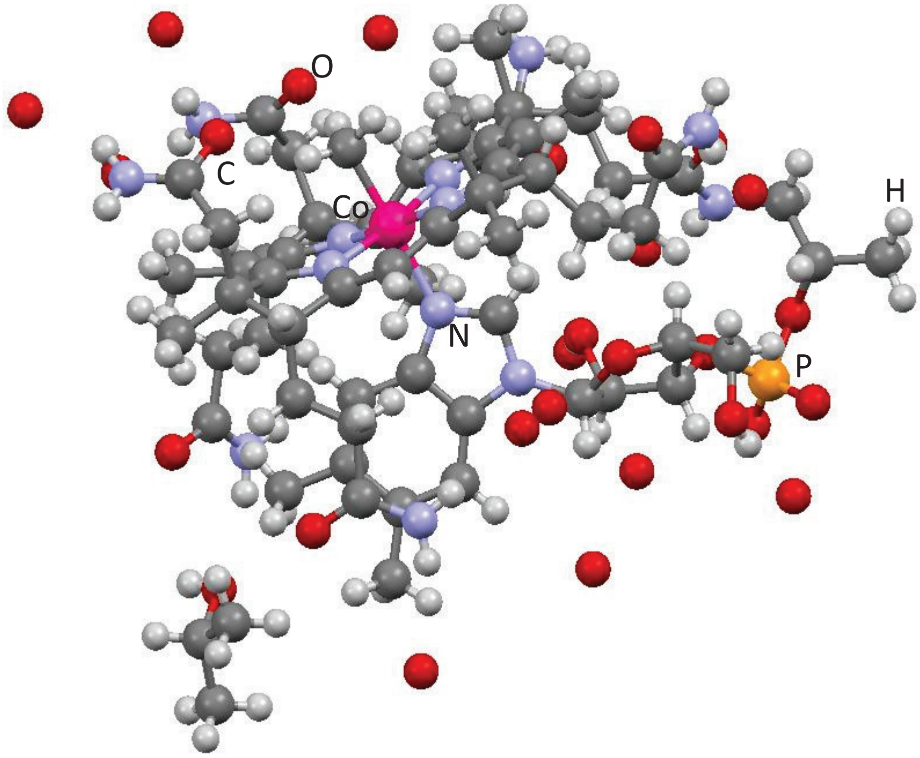

Figure A.12: Molecular structure of methylcobalamin solved from X-ray data.

A.4.2 Methylcobalamin

Crystal growth: Crystal growth of methylcobalamin ($CoC_{63}H_{91}N_{13}O_{14}P$) was conducted similarly to cyanocobalamin. 12 mg of methylcobalamin were solved in 1 ml water and mixed with 1.5 ml isopropyl alcohol. The mixture was then stored in an isopropyl atmosphere. Small, rectangular crystals of a size of between 200 × 100 × 100 μ m^3 and 80 × 50 × 10 μ m^3 grew within one week.

Table A.7: Data collection parameters for measurements of the 1st methylcobalamin crystal.

Crystal size	$150 \times 60 \times 80$ μ m^3
Detector distance	65 mm
Starting angle	0°
Oscillation range	2°
Exposure time	1 s
No. of images	4500
Filter transmission	1.0 (0.2)
Photon flux	$193.49 \cdot 10^9$ ph/s without filter ($34.38 \cdot 10^9$ ph/s (1st round), $36.6 \cdot 10^9$ ph/s (2nd round))
Temperature	100 K
Energy	16.45 keV
Wavelength	0.7537 Å

Table A.8: Data collection parameters for measurements of the 2nd methylcobalamin crystal.

Crystal size	$250 \times 50 \times 40$ μm^3
Detector distance	65 mm
Starting angle	0°
Oscillation range	2°
Exposure time	1 s
No. of images	4500
Filter transmission	1.0
Photon flux	$193.49 \cdot 10^9$ ph/s
Temperature	100 K
Energy	16.45 keV
Wavelength	0.7537 Å

Table A.9: Data evaluation and structure refinement parameters for the 1st methylcobalamin crystal, measured without filters.

Rmrgd-F	2.1%
Resolution	0.7 Å
Data completeness	70.9%
Number of reflections (total)	12099
Number of reflections (gt)	11647
Cell constants	a = 16.36 Å b = 20.60 Å c = 24.22 Å $\alpha = 90.00°$ $\beta = 90.00°$ $\gamma = 90.00°$
Space group	$P2_12_12_1$
R1 value from structure refinement	0.0602
Solvent molecules	$9.5 \cdot H_2O + 0.75 \cdot C_3H_8O$

Table A.10: Data evaluation and structure refinement parameters of the 1st methylcobalamin crystal, measured with 20% filter transmission.

Rmrgd-F	2.3%
Resolution	0.7 Å
Data completeness	64.4%
Number of reflections (total)	12240
Number of reflections (gt)	11421
Cell constants	a = 16.36 Å b = 20.60 Å c = 24.20 Å $\alpha = 90.00°$ $\beta = 90.00°$ $\gamma = 90.00°$
Space group	$P2_12_12_1$
R1 value from structure refinement	0.0643
Solvent molecules	$9.5 \cdot H_2O + 0.75 \cdot C_3H_8O$

Table A.11: Data evaluation and structure refinement parameters of the 2nd methylcobalamin crystal.

Rmrgd-F	2.1%
Resolution	0.7 Å
Data completeness	78.5%
Number of reflections (total)	13238
Number of reflections (gt)	12755
Cell constants	a = 16.36 Å b = 20.58 Å c = 24.18 Å $\alpha = 90.00°$ $\beta = 90.°$ $\gamma = 90.00°$
Space group	$P2_12_12_1$
R1 value from structure refinement	0.0546
Solvent molecules	$9{\cdot}H_2O + 0.75{\cdot}C_3H_8O$

A.5 X-ray diffraction measurements on amino acids and thymidine

A.5.1 L-serine

Crystal growth: Single crystals were grown by controlled cooling of an aqueous solution of L-serine saturated at 90°C. After equilibration at 60°C the solution was cooled down to 45°C using a cooling rate of 1°C/min. The obtained crystals were up to 5 cm in the longest dimension. They could then be cut using a Well 6234 wire saw equipped with a 0.5 mm thin diamond wire, which was immersed in a water bath prior to cutting.

Table A.12: Data collection parameters for L-serine.

Crystal size	$80 \times 50 \times 20\ \mu\ m^3$
Detector distance	185 mm
Starting angle	0°
Oscillation range	1°
Exposure time	1 s
No. of images	22680
Photon flux	$4.2 \cdot 10^{10}$ ph/s
Temperature	100 K
Energy	17.5 keV
Wavelength	0.7085 Å

Table A.13: Data evaluation and structure refinement parameters of L-serine.

Rmrgd-F	1.2%
Resolution	0.7 Å
Data completeness	87.4%
Number of reflections (total)	1037
Number of reflections (gt)	1028
Cell constants	a = 5.62 Å b = 8.51 Å c = 9.25 Å $\alpha = 90.00°$ $\beta = 90.00°$ $\gamma = 90.00°$
Space group	$P2_12_12_1$
R1 value from structure refinement	0.0322
Solvent molecules	none

Electron paramagnetic resonance spectroscopy: It is well-known that L-serine is EPR-silent in its native state. EPR experiments on an X-ray irradiated L-serine crystal, which was transported and transferred under liquid nitrogen showed, an EPR-signal. This shows that a reaction takes place upon X-ray irradiation.

Further investigations have to be performed to find the origin of this signal. Since the EPR-signal of crystals depends heavily on the alignment of the sample, it would be more helpful to first investigate an X-ray irradiated sample consisting of L-serine powder.

Thawing of the L-serine crystals: A single crystal of L-serine X-ray irradiated for 14400 seconds was removed from liquid nitrogen and thawed to room temperature. Upon thawing the crystal broke into two pieces (fig. A.14) after approximately 30 seconds and started to deteriorate to a foam-like structure (60 s to 300 s). After approximately 1200 seconds an oil-like film was left (fig. A.15).

First Raman investigations of L-serine: It was the goal of in-situ Raman measurements at 100 K to obtain information about the decay of theCH_2-group which is clearly visible in the spectra. The experiments were conducted with a 532 nm laser, which led to a high background originating from fluorescence of the L-serine crystal (fig. A.17). The

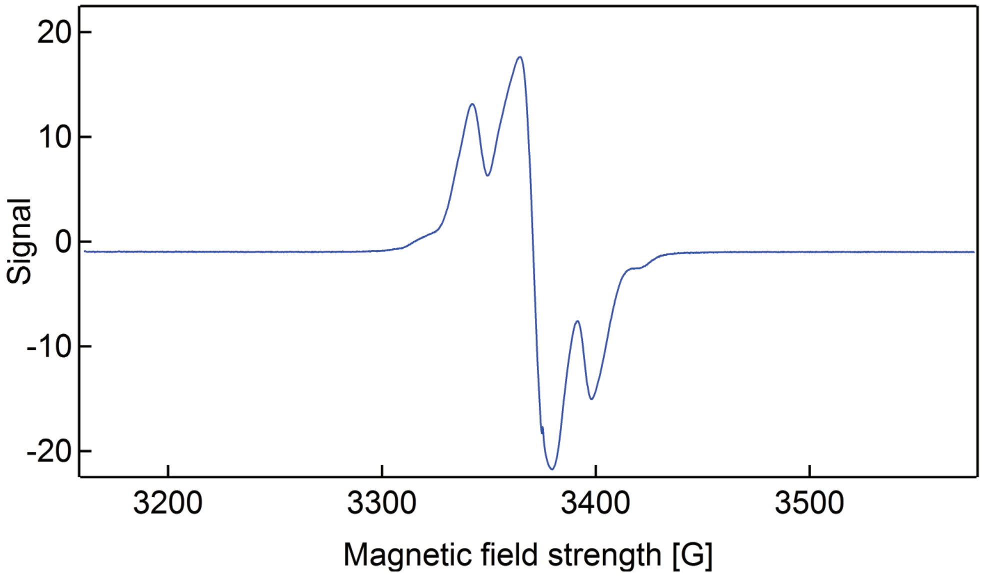

Figure A.13: EPR-spectrum of a single crystal of L-serine after 30 minutes of irradiation with a white X-ray beam.

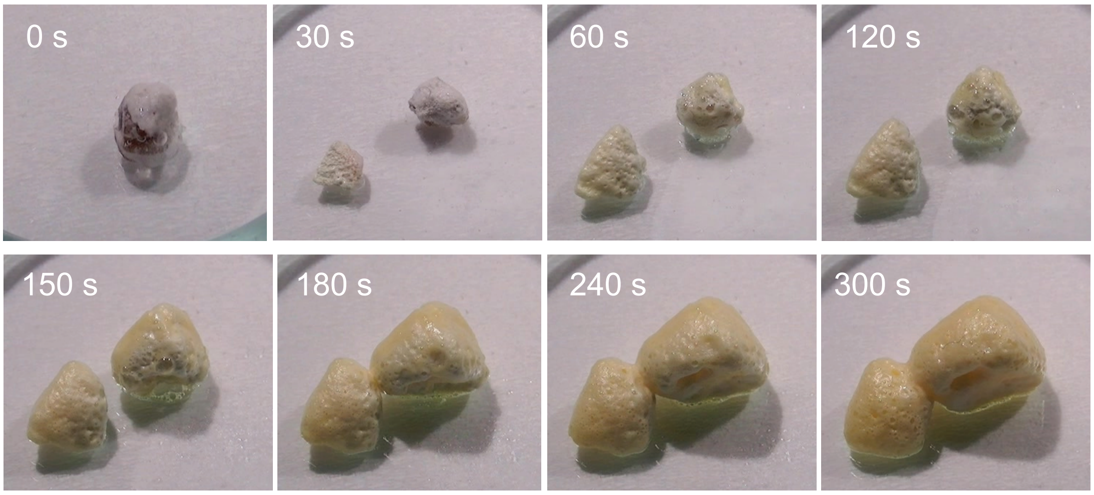

Figure A.14: Thawing of a single crystal of L-serine, irradiated for 14400 seconds.

Figure A.15: Oil-like film left upon thawing of a single crystal of L-serine, irradiated for 14400 seconds.

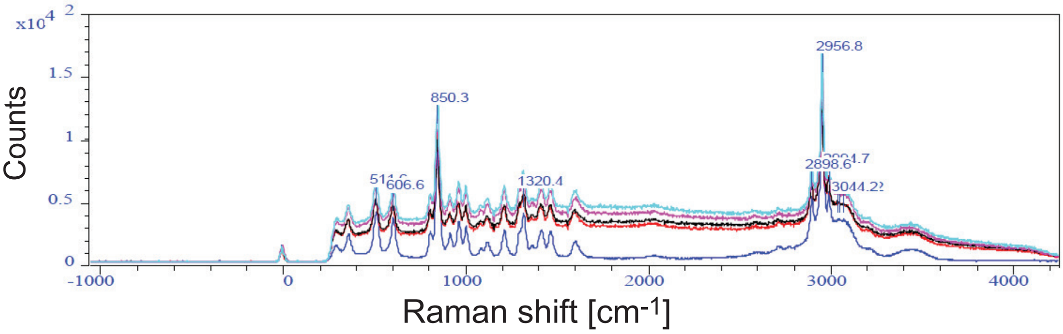

Figure A.16: Raman spectra of unirradiated (dark blue) and irradiated (red, black, violet and bright blue, subsequently) L-serine. Irradiation was performed with a white X-ray beam. The growing background is clearly visible.

crystal changes colour upon irradiation, turning from transparent to red. Possible changes (which would be as small as 20%) could not be detected with such a high background. Further in-situ Raman investigations with another wavelength are planned.

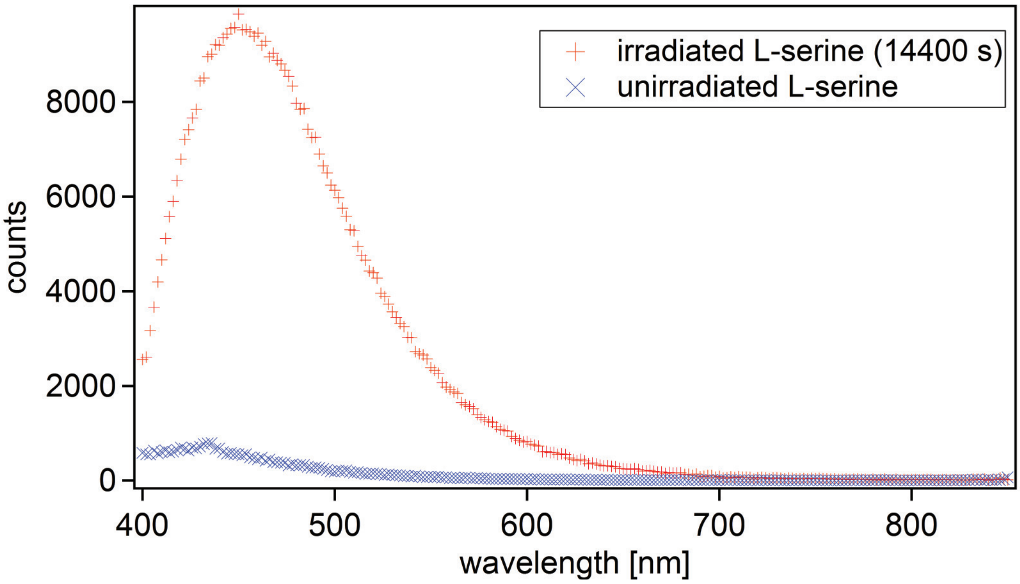

Figure A.17: Fluorescence spectra of irradiated (red) and unirradiated (blue) L-serine. The irradiated compound shows a fluorescence signal at 532 nm.

A.5.2 L-alanine

Crystal growth: A saturated solution of L-alanine was prepared by solving 2.0 g of L-alanine powder in 10 ml H_2O at 70°C. The solution was then stirred for 1 h. The clear solution was then covered and stored at room temperature. Small, transparent crystals grew within three days by slow evaporation.

Table A.14: Data collection parameters for L-alanine.

Crystal size	60 × 20 × 10 μ m^3
Detector distance	185 mm
Starting angle	0°
Oscillation range	2°
Exposure time	1 s
No. of images	4320
Photon flux	$13.0 \cdot 10^{10}$ ph/s
Temperature	100 K
Energy	16.4 keV
Wavelength	0.7560 Å

Table A.15: Data evaluation and structure refinement parameters of L-alanine.

Rmrgd-F	1.9%
Resolution	0.7 Å
Data completeness	84.1%
Number of reflections (total)	959
Number of reflections (gt)	940
Cell constants	a = 5.79 Å b = 5.94 Å c = 12.26 Å α = 90.00° β = 90.00° γ = 90.00°
Space group	$P2_12_12_1$
R1 value from structure refinement	0.0302
Solvent molecules	none

A.5.3 Thymidine

Crystal growth: 10 ml of a saturated aqueous solution of deoxythymidine were prepared at 70°C. The solution was filtered, covered and stored in a temperature-controlled environment. The temperature was decreased by 3°C/day. Crystals started to grow after one week of evaporation at higher temperatures.

Table A.16: Data collection parameters for thymidine.

Crystal size	$70 \times 30 \times 20\ \mu$ m^3
Detector distance	165 mm
Starting angle	0°
Oscillation range	1°
Exposure time	0.5 s
No. of images	19080
Photon flux	$9.0 \cdot 10^{10}$ ph/s
Temperature	100 K
Energy	17.5 keV
Wavelength	0.7085 Å

Table A.17: Data evaluation and structure refinement parameters of thymidine.

Rmrgd-F	1.2%
Resolution	0.8 Å
Data completeness	95.6%
Number of reflections (total)	1240
Number of reflections (gt)	1223
Cell constants	a = 4.81 Å b = 13.74 Å c = 16.22 Å $\alpha = 90.00°$ $\beta = 90.00°$ $\gamma = 90.00°$
Space group	$P2_12_12_1$
R1 value from structure refinement	0.0263
Solvent molecules	none

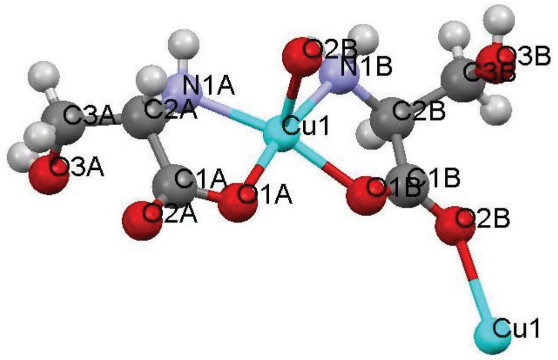

Figure A.18: Labeling scheme of CuSer.

A.6 Metal amino acid complexes

A.6.1 Bis(L-serinato)copper(II) (CuSer)

Crystal growth: 157,7 mg (0.5 mmol) $Ba(OH)_2{\cdot}8H_2O$ (s), 105 mg (1 mmol) L-serine and 124.8 mg (0.5 mmol) $CuSO_4{\cdot}5H_2O$ were solved in 10 ml H_2O at room temperature and stirred for 1 h, giving an intensely blue solution. The light blue sediment was separated from the solution by centrifugation. The clear blue solution was mixed with ethanol in a 1:2 ratio, covered and stored at room temperature. Small, blue crystals grew within a day.

Table A.18: Data collection parameters for CuSer1.

Crystal size	250 × 100 × 20 μm^3
Detector distance	40 mm
Starting angle	0°
Oscillation range	2°
Dose mode setting	200 kHz
No. of images	4860
Photon flux	$5{\cdot}10^{10}$ ph/s
Temperature	100 K
Energy	15.31 keV
Wavelength	0.81 Å

Table A.19: Data collection parameters for CuSer2.

Crystal size	250 × 100 × 20 μm^3
Detector distance	40 mm
Starting angle	0°
Oscillation range	2°
Dose mode setting	400 kHz
No. of images	1440
Photon flux	$5{\cdot}10^{10}$ ph/s
Temperature	100 K
Energy	15.31 keV
Wavelength	0.81 Å

Table A.20: Data collection parameters for CuSer3.

Crystal size	250 × 150 × 30 μm^3
Detector distance	40 mm
Starting angle	0°
Oscillation range	2°
Dose mode setting	400 kHz
No. of images	4140
Photon flux	$5{\cdot}10^{10}$ ph/s
Temperature	100 K
Energy	15.31 keV
Wavelength	0.81 Å

Table A.21: Data evaluation and structure refinement parameters for CuSer1.

Rmrgd-F	4.4%
Resolution	0.9 Å
Data completeness	88.2%
Number of reflections (total)	640
Number of reflections (gt)	638
Cell constants	a=5.65 Å b=8.40 Å c=9.95 Å α=90.00° β=90.56° γ=90.00°
Space group	$P2_1$
R1 value from structure refinement	0.0388
Solvent molecules	none

Table A.22: Data evaluation and structure refinement parameters for CuSer2.

Rmrgd-F	5.4%
Resolution	0.9 Å
Data completeness	92.4%
Number of reflections (total)	1226
Number of reflections (gt)	1219
Cell constants	a=5.64 Å b=8.40 Å c=9.94 Å α=90.00° β=90.58° γ=90.00°
Space group	$P2_1$
R1 value from structure refinement	0.0327
Solvent molecules	none

Table A.23: Data evaluation and structure refinement parameters for CuSer3.

Rmrgd-F	4.4%
Resolution	1.0 Å
Data completeness	97.4%
Number of reflections (total)	1283
Number of reflections (gt)	1245
Cell constants	a=5.61 Å b=8.36 Å c=9.90 Å α=90.00° β=90.58° γ=90.00°
Space group	$P2_1$
R1 value from structure refinement	0.0492
Solvent molecules	none

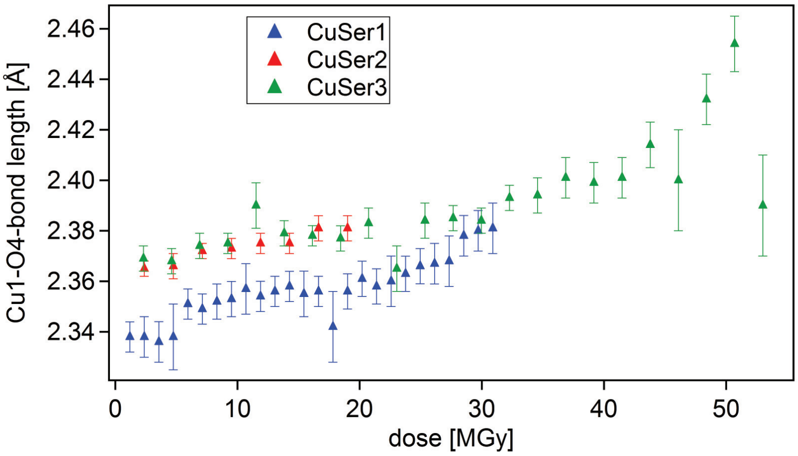

Figure A.19: Change of the Cu1-O2B-bond length in CuSer with increasing X-ray dose.

Bond length change of the Cu1-O2B-bond: In case of CuSer an increase of the Cu1-O2B-bond length with increasing X-ray dose could be be observed (see fig. A.19). This bond length change upon X-ray irradiation could indicate a cleavage of the Cu1-O2B-bond.

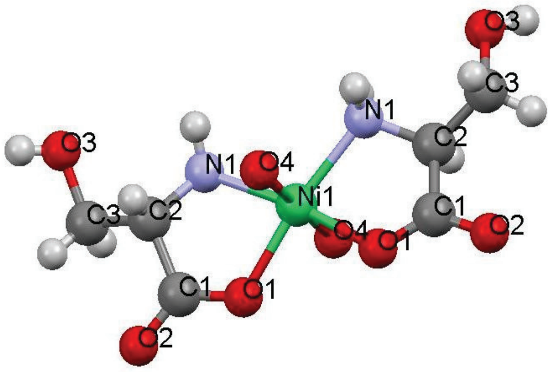

Figure A.20: Labeling scheme of NiSer.

A.6.2 Diaquobis(L-serinato)nickel(II) (NiSer)

Crystal growth: 1.5 g (4.8 mmol) $Ba(OH)_2 \cdot 8H_2O$ (s) were added to an aqueous solution of 1.00 g (9.5 mmol) L-serine at room temperature. The mixture was subsequently stirred for 5 minutes. After addition of 6 ml of an aqueous solution of 1.34 g (4.8 mmol) $NiSO_4 \cdot 7H_2O$ the mixture was stirred for another 45 minutes. The pale precipitate was separated from the intensely blue solution by centrifugation. The solvent was completely removed under reduced pressure yielding a deep blue solid.
Single crystals suitable for X-ray diffraction were grown by recrystallization of 50 mg of the raw product from a mixture of water/isopropyl alcohol (2:1). After 2 h pale blue crystals were obtained by slow evaporation.

Bond length change of the Ni1-O4-bond: In case of the single refined NiSer, no bond length changes could be observed for both oxygen atoms connected to the nickel center (see fig. A.21).

Table A.24: Data collection parameters for NiSer1.

Crystal size	100 × 60 × 20 μm^3
Detector distance	40 mm
Starting angle	0°
Oscillation range	2°
Dose mode setting	200 kHz
No. of images	4680
Photon flux	$5\cdot10^{10}$ ph/s
Temperature	100 K
Energy	15.31 keV
Wavelength	0.81 Å

Table A.25: Data collection parameters for NiSer2.

Crystal size	100 × 60 × 20 μm^3
Detector distance	40 mm
Starting angle	0°
Oscillation range	2°
Dose mode setting	400 kHz
No. of images	4860
Photon flux	$5\cdot10^{10}$ ph/s
Temperature	100 K
Energy	15.31 keV
Wavelength	0.81 Å

Table A.26: Data evaluation and structure refinement parameters of NiSer1.

Rmrgd-F	4.4%
Resolution	0.9 Å
Data completeness	88.2%
Number of reflections (total)	794
Number of reflections (gt)	777
Cell constants	a=7.70 Å b=8.59 Å c=8.87 Å α=90.00° β=102.50° γ=90.00°
Space group	C2
R1 value from structure refinement	0.0539
Solvent molecules	none

Table A.27: Data evaluation and structure refinement parameters of NiSer2.

Rmrgd-F	9.1%
Resolution	0.9 Å
Data completeness	84.0%
Number of reflections (total)	n/a
Number of reflections (gt)	n/a
Cell constants	a=7.73 Å b=8.58 Å c=8.87 Å α=90.00° β=102.29° γ=90.00°
Space group	C2
R1 value from structure refinement	n/a
Solvent molecules	n/a

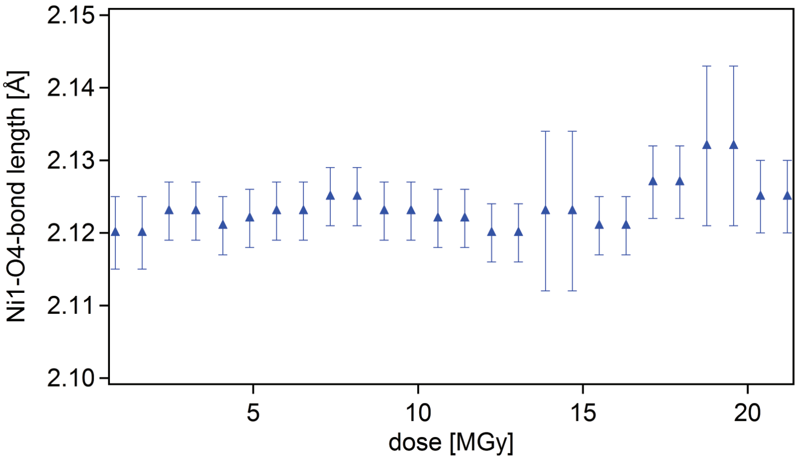

Figure A.21: Change of the Ni1-O4-bond length in NiSer1 with increasing X-ray dose.

A.6.3 Bis-(L-isoleucinato)copper(II) (CuIso)

Crystal growth: 262 mg (2 mmol) L-isoleucine were solved in 30 ml H_2O and stirred at 70°C. After 5 minutes 221,1 mg (1 mmol) $CuCO_3{\cdot}Cu(OH)_2$, were added. The solution was filtered, covered and stored at room temperature. Small, rectangular, blue crystals grew within two days by evaporation.

Table A.28: Data collection parameters of CuIso1.

Crystal size	$120 \times 150 \times 10\ \mu m^3$
Detector distance	40 mm
Starting angle	0°
Oscillation range	2°
Dose mode setting	100 kHz
No. of images	4860
Photon flux	$5{\cdot}10^{10}$ ph/s
Temperature	100 K
Energy	15.31 keV
Wavelength	0.81 Å

Bond length change of the Cu1-O3-bond: A possible mechanism for the reduction of copper-isoleucine could be a cleavage of the bond between the copper centre and the

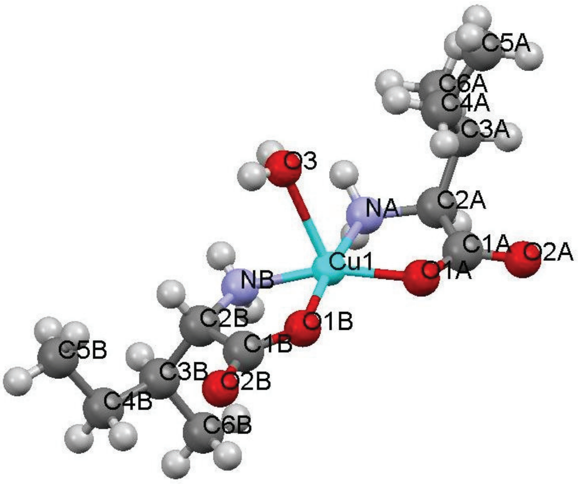

Figure A.22: Labeling scheme of CuIso.

Table A.29: Data collection parameters for CuIso2.

Crystal size	150 × 150 × 10 μm^3
Detector distance	40 mm
Starting angle	0°
Oscillation range	2°
Dose mode setting	400 kHz
No. of images	1800
Photon flux	$5 \cdot 10^{10}$ ph/s
Temperature	100 K
Energy	15.31 keV
Wavelength	0.81 Å

Table A.30: Data evaluation and structure refinement parameters of CuIso1.

Rmrgd-F	3.7%
Resolution	0.9 Å
Data completeness	99.2%
Number of reflections (total)	2189
Number of reflections (gt)	2067
Cell constants	a=7.55 Å b=9.40 Å c=21.45 Å α=90.00° β=90.00° γ=90.00°
Space group	$P2_12_12_1$
R1 value from structure refinement	0.0467
Solvent molecules	none

Table A.31: Information on data evaluation and structure refinement of the 2nd copper-isoleucine crystal.

Rmrgd-F	2.3%
Resolution	0.9 Å
Data completeness	97.8%
Number of reflections (total)	2170
Number of reflections (gt)	2126
Cell constants	a=7.59 Å b=9.45 Å c=21.59 Å α=90.00° β=90.00° γ=90.00°
Space group	$P2_12_12_1$
R1 value from structure refinement	0.0407
Solvent molecules	none

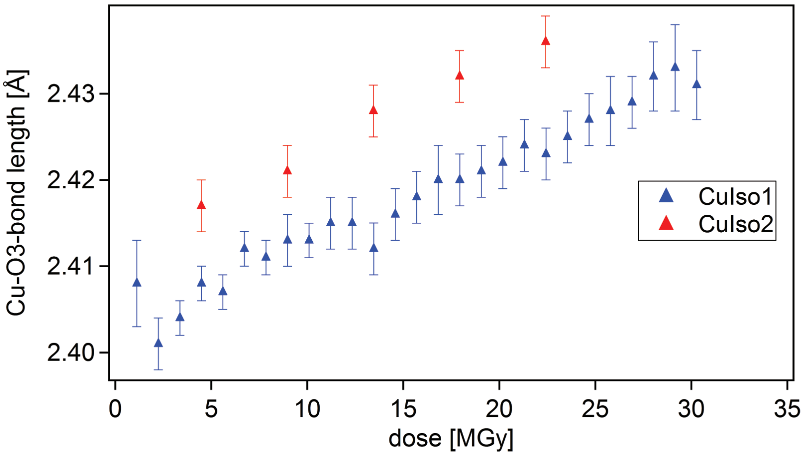

Figure A.23: Change of the Cu1-O3 bond length for CuIso with increasing X-ray dose

water ligand (Cu1-O3). A bond elongation between these two atoms could be observed in the X-ray data for both crystals (see fig. A.23).

A.7 X-ray absorption measurements on B12 cofactors

For dose calculation of the XANES measurements at the SuperXAS beamline overall molecular formulas were determined. In the case of the ammonium ferric citrate which is a combination of different amounts of Fe^{3+} and $[NH_4]^+$ ions ($Fe_xC_6H_{5+4y}N_yO_7$) the molecular formula was assumed to be $FeC_6H_5NO_7$, thus including a small error in the absorption coefficient.

Table A.32 shows a summary of all temperatures measured for the different compounds during K-edge XANES measurements at the SuperXAS beamline at the Swiss Light Source.

Table A.32: Summary of the different compounds measured at different temperatures in K-edge XANES.

Compound	**5**	**25**	**50**	**100**	**150**	**200**	**250**	**300**
Solid cobalamin	x	x	x	x	x	x	x	x
Aqueous cobalamin	-	-	-	x	x	x	x	-
Solid ammonium ferric citrate	-	-	-	x	-	-	-	x
Aqueous ammonium ferric citrate	-	-	-	x	-	x	-	-
Potassium hexacyano ferrate	-	-	-	x	-	-	-	x
Diiron-dithiolate	-	-	-	x	-	-	-	x
Pyrite	-	-	-	x	-	-	-	x

L-edge XANES measurements on the L2 and L3 edge of Co(III) were conducted on thin methyl- as well as cyanocobalamin films to countercheck the results from Champloy *et al.*[23] at the PolLux beamline (X07DA) at the Swiss Light source[‡]. For this, low concentrations of cyanocobalamin and methylcobalamin were solved in ethanol. The solution was then distributed on a silicon nitride window with a membrane of 100 nm thickness and a surface of $0.25 \times 0.25\ \mu m^2$.

The ethanol evaporated, yielding a film of roughly 1.5 μm in thickness, which corresponds to a transmission of around 50%. The samples were cooled to 100 K during measurements. No dose evaluation was obtained, since both datasets were investigated subsequently

---

[‡] http://www.psi.ch/sls/pollux/pollux

and had a comparable absorption coefficient. So it was assumed that each dataset for methylcobalamin had absorbed roughly the same dose as each dataset of cyanocobalamin. The cyanocobalamin dataset was analysed directly at the beamline, so only one image of the series is shown here. The plot of methylcobalamin was performed from already normalised data. While cyanocobalamin showed strong changes upon irradiation, such as the disappearance of the pre-edge peak of the first absorption edge as well as a strong shift to lower energies, no such changes were observed for methylcobalamin. Only a slight change in the intensity of both absorption edges as well as a widening of the peaks could be found, which cannot be directly connected to photoreduction.

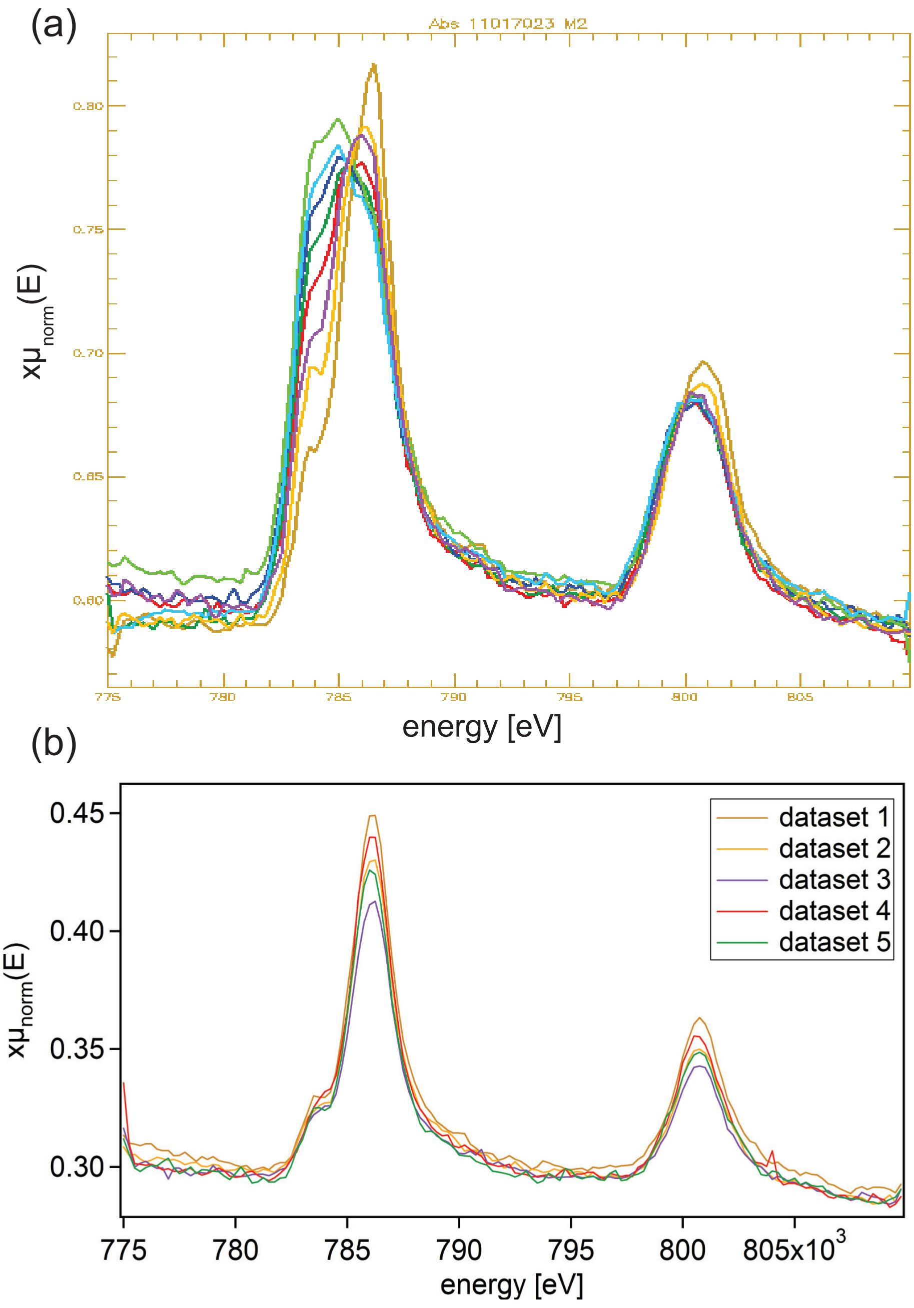

Figure A.24: Dose series of L-edge XANES spectra of cyano- (a) and methyl- (b) cobalamin with similar colour scheme.

A.8 Neutron diffraction measurements on amino acids and thymidine

A.8.1 L-serine

Table A.33: Occupancy and ITDP of the positions of all 7 hydrogen atoms in the L-serine molecule after 0 seconds of irradiation.

name	**occupancy**	**occupancy standard deviation**	**ITDP** [Å^2]
H1	1.00000	0.00012	0.01799
H2	1.00000	0.00012	0.01799
H3	0.97220	0.00012	0.01799
H4	1.00000	0.00010	0.01459
H5	1.00000	0.00014	0.02638
H6	1.00000	0.00012	0.01826
H7	1.00000	0.00012	0.01826

Table A.34: Occupancies and ITDPs of the positions of all 7 hydrogen atoms in the L-serine molecule after 375 seconds of irradiation.

name	**occupancy**	**occupancy standard deviation**	**ITDP** [Å^2]
H1	1.00000	0.00017	0.02052
H2	1.00000	0.00017	0.02052
H3	0.89412	0.00018	0.02052
H4	1.00000	0.00018	0.02066
H5	0.94895	0.00200	0.03568
H6	0.92073	0.00019	0.02482
H7	1.00000	0.00200	0.02482

Table A.35: Occupancies and ITDPs of the positions of all 7 hydrogen atoms in the L-serine molecule after 600 seconds of irradiation.

name	**occupancy**	**occupancy standard deviation**	**ITDP** [Å^2]
H1	1.00000	0.00200	0.02483
H2	1.00000	0.00200	0.02483
H3	1.00000	0.00200	0.02483
H4	1.00000	0.00200	0.02313
H5	0.86452	0.00300	0.04304
H6	0.92390	0.00200	0.02994
H7	0.98531	0.00200	0.02994

Table A.36: Occupancy and ITDP of the positions of all 7 hydrogen atoms in the L-serine molecule after 1680 seconds of irradiation.

name	**occupancy**	**occupancy standard deviation**	**ITDP** [Å^2]
H1	0.92129	0.00600	0.03148
H2	1.00000	0.00700	0.03148
H3	1.00000	0.00600	0.03148
H4	1.00000	0.00800	0.03960
H5	0.79800	0.00700	0.05580
H6	0.80742	0.00700	0.03882
H7	1.00000	0.00700	0.03882

Table A.37: R1 value from structure refinement and unit cell volume of L-serine determined from neutron diffraction data.

time [s]	**0**	**375**	**600**	**1680**
R1 value	0.0907	0.0990	0.1060	0.1719
unit cell volume [Å^3]	439.92	445.12	445.83	447.76

A.8.2 L-alanine

Table A.38: R1 value from structure refinement and unit cell volume of L-alanine determined from neutron diffraction data.

time [s]	**600**	**3600**
R1 value	0.1001	0.1679
unit cell volume [Å^3]	421.93	419.83

A.8.3 Thymidine

Table A.39: Occupancies and ITDPs of the positions of all 14 hydrogen atoms in the thymidine molecule after 0 seconds of irradiation.

name	**occupancy**	**occupancy standard deviation**	**ITDP [Å^2]**
H1	1.00000	0.00200	0.01606
H2	1.00000	0.00200	0.01643
H3	1.00000	0.00200	0.02757
H4	1.00000	0.00200	0.02757
H5	1.00000	0.00200	0.02757
H6	1.00000	0.00200	0.01821
H7	1.00000	0.00200	0.02058
H8	1.00000	0.00200	0.01424
H9	1.00000	0.00200	0.01803
H10	1.00000	0.00200	0.01803
H11	1.00000	0.00019	0.01504
H12	1.00000	0.00200	0.01455
H13	1.00000	0.00200	0.01900
H14	1.00000	0.00200	0.01900

Table A.40: Occupancies and ITDPs of the positions of all 14 hydrogen atoms in the thymidine molecule after 600 seconds of irradiation.

name	**occupancy**	**occupancy standard deviation**	**ITDP [Å^2]**
H1	1.00000	0.00018	0.01211
H2	1.00000	0.00019	0.01670
H3	1.00000	0.00200	0.02742
H4	1.00000	0.00200	0.02742
H5	1.00000	0.00200	0.02742
H6	1.00000	0.00200	0.01940
H7	0.97615	0.00200	0.02110
H8	1.00000	0.00018	0.01200
H9	1.00000	0.00200	0.01844
H10	1.00000	0.00200	0.01844
H11	1.00000	0.00018	0.01354
H12	1.00000	0.00018	0.01498
H13	1.00000	0.00200	0.01880
H14	1.00000	0.00200	0.01880

Table A.41: Occupancies and ITDPs of the positions of all 14 hydrogen atoms in the thymidine molecule after 1200 seconds of irradiation.

name	**occupancy**	**occupancy standard deviation**	**ITDP [Å^2]**
H1	1.00000	0.00019	0.01294
H2	1.00000	0.00200	0.01833
H3	1.00000	0.00200	0.03187
H4	1.00000	0.00300	0.03187
H5	0.96830	0.00200	0.03187
H6	1.00000	0.00200	0.01891
H7	0.92894	0.00200	0.02136
H8	1.00000	0.00200	0.01328
H9	1.00000	0.00200	0.02138
H10	1.00000	0.00200	0.02138
H11	1.00000	0.00019	0.01536
H12	1.00000	0.00018	0.01354
H13	1.00000	0.00200	0.02050
H14	1.00000	0.00200	0.02050

Table A.42: R1 value from structure refinement and unit cell volume of thymidine determined from neutron diffraction data.

time [s]	**0**	**600**	**1200**
R1 value	0.0805	0.0881	0.0902
unit cell volume [Å^3]	1067.56	1066.95	1069.34